SURFACE PLASMON RANDOM SCATTERING

AND RELATED PHENOMENA

by

ROBERT PAUL SCHUMANN

A DISSERTATION

Presented to the Department of Physics
and the Graduate School of the University of Oregon
in partial fulfillment of the requirements
for the degree of
Doctor of Philosophy

June 2009

University of Oregon Graduate School

Confirmation of Approval and Acceptance of Dissertation prepared by:

Robert Schumann

Title:

"Surface Plasmon Random Scattering And Related Phenomena"

This dissertation has been accepted and approved in partial fulfillment of the requirements for the Doctor of Philosophy degree in the Department of Physics by:

Stephen Kevan, Chairperson, Physics
Stephen Gregory, Advisor, Physics
Michael Raymer, Member, Physics
David Strom, Member, Physics
Mark Lonergan, Outside Member, Chemistry

and Richard Linton, Vice President for Research and Graduate Studies/Dean of the Graduate School for the University of Oregon.

June 13, 2009

Original approval signatures are on file with the Graduate School and the University of Oregon Libraries.

An Abstract of the Dissertation of

Robert Paul Schumann for the degree of Doctor of Philosophy

in the Department of Physics to be taken June 2009

Title: SURFACE PLASMON RANDOM SCATTERING AND RELATED PHENOMENA

Approved: _____
Dr. Stephen Gregory

Surface plasmon polaritons (SPPs) are collective electron excitations with attendant electromagnetic fields which propagate on a metal-dielectric interface. They behave, in many ways, as model two-dimensional electromagnetic waves. However, because the evanescent field of the SPPs extends a short distance outside the interface, a near-field probe can modify the wave propagation. We use this behavior to study both SPP scattering within the plane of the interface and also the transition to free-space propagation out of the plane.

We have, in particular, studied the multiple scattering of SPPs excited on rough silver films. Our laboratory possesses apertureless near-field scanning optical microscopes (A-NSOMs), the probes of which can act as an in-plane scatterer of SPPs. Subsequent momentum-conserving decays of the SPPs generate an expanding hollow

cone of light to which information about the direction and phase of the SPPs on the surface is transferred.

A focus of our studies has been SPP multiple scattering when one of the scatterers (the tip) can move. This problem is very closely related to a similar problem in mesoscopic electronic transport, involving "universal conductance fluctuations". It is also related to various radar-detection, microwave communications and medical imaging problems. In parallel with actual experimental measurements, we have also conducted extensive Monte Carlo simulations of the scattering.

Multiple scattering leads to the appearance and detection of "speckle" in the far field. A speckle field, however, is more properly considered in terms of its embedded optical vortices and so we have used holographic techniques to study these. We have demonstrated that vortices can be manipulated, created and destroyed by movement of the STM probe tip.

Optical vortices are an example of the effect of "geometric" or "topological" phase in physics and as such link the trajectory of a parameter in one space to the phase observed in another. In our case, the trajectory of the A-NSOM tip parallel to the sample surface plane generates topological phase in the far field, manifestations of which are vortices.

CURRICULUM VITAE

NAME OF AUTHOR: Robert Paul Schumann

GRADUATE AND UNDERGRADUATE SCHOOLS ATTENDED:

University of Oregon
University of Missouri

DEGREES AWARDED:

Doctor of Philosophy in Physics, 2009, University of Oregon
Bachelor of Science in Physics, 1999, University of Missouri

AREAS OF SPECIAL INTEREST:

Surface Plasmon Polariton Physics, Near-Field and Far-Field Optics

PROFESSIONAL EXPERIENCE:

Graduate Research Assistant, Department of Physics,
University of Oregon, Eugene, 2004-2009.

Graduate Teaching Assistant, Department of Physics,
University of Oregon, Eugene, 2000-2004, 2009.

GRANTS, AWARDS AND HONORS:

GANN Grant, 2004.

ACKNOWLEDGMENTS

There is no way I could have made it through graduate school if it wasn't for my advisor Stephen Gregory. Not only did he support me financially and mentally, but he made my experience here at the University of Oregon tolerable if not enjoyable. I found our conversations (and arguments) regarding mathematics, physics and science to be engaging, stimulating and incredibly instructive. His knowledge, expertise and insights provided much fuel for our research and helped me to mature as a physicist. Equally enthralling were our many discussions on politics, religion, philosophy, and the state of the world. His interests in computers and technology resonated well with my own as did our common fondness for plants, animals and the natural world. It has been over these past years working in his lab, that I have come to see Steve not only as my advisor and mentor, but also as my friend.

I would also like to thank my committee members Steve Kevan for chairing my committee and for teaching me solid state physics, David Strom, for being one of the best professors a TA could have, Michael Raymer for knocking some sense into my head, and Mark Lonergan for advice on dealing with the graduate school. While I was no doubt a source of frustration for my committee members, their patients and level headedness helped see me through this process and for this, I thank them.

I would like to thank the physics office staff, especially Bonnie Grimm, for all of her assistance and thanks to Chris and all of the guys in the machine shop.

I would also like to thank my fellow classmates and especially Peter Hugger, Tim Sweeney, and Jeremy Thorn for their brief stint with me down in the lab.

Last, but certainly not least, I want to thank my best friend, companion, and better half, Amy and our beloved little ones, Alex, Ariel, Egan and Griffin. Thanks for all of your support through my many years of schooling and for enriching my life beyond words. I am truly grateful for all of the happiness and love you have brought to my life.

DEDICATION

To my Mom, Dad, Fred and Christa.

TABLE OF CONTENTS

Chapter Page

I. INTRODUCTION 1

I.1 Historical Overview of Surface Plasmon Physics 1
I.2 Our Study of Surface Plasmon Polaritons 6
I.3 Outline for the Dissertation 7

II. SURFACE PLASMON POLARITONS 9

II.1 Introduction to Surface Plasmon Polariton Derivation 9
II.2 Maxwell's Equations 10
II.3 Simplified Maxwell's Equations in Matter 13
II.4 Finding Solutions For a Metal–Dielectric Interface 14
II.5 Drude-Sommerfeld Model for a Metallic Dielectric Function 17
II.6 Comments on The SPP Field 19
II.7 Dispersion Relation for SPP 22
II.8 Prism Coupled SPP 22
II.9 Fresnel Equations 25

III. EXPERIMENTAL APPARATUS 31

III.1 Introduction 31
III.2 The Scanning Tunneling Microscope 31
III.3 The Scanning Tunneling Microscope Used in Our Lab 33
III.4 STM Calibration 39
III.5 Thin Film Vacuum Deposition 40
III.6 Full Experimental Apparatus 43

Chapter Page

IV. GENERATING IMAGES IN PHOTOMETRY SPACE 45

IV.1. Introduction 45
IV.2. Focused Incident Gaussian Beam 46
IV.3. Description of Terms 53
IV.4. Scanning Plasmon Optical Microscopy 53
IV.5. Single Scattering and Primary Stripes 55
IV.6. Coherent Back Scattering and Secondary Waves 61

V. CONE SPECKLE, RANDOM SCATTERING, AND OPTICAL VORTICES 69

V.1. Introduction 69
V.2. Cone Speckle and SPP Scattering 69
V.3. Scattering Regimes 72
V.4. Angular Momentum in Electromagnetic Fields and Optical Vortices 75
V.5. Phase Singularities in Random Wave Fields 77
V.6. Cone Speckle 82
V.7. Photometry Maps in the Absence of Background Fields 84
V.8. Monte Carlo SPP Scattering Simulation 89
V.9. Future Projects 97

VI. CONCLUSION 102

VI.1. Conclusion and Future Work 102

APPENDIX: MONTE CARLO SPP SCATTERING SIMULATION PROGRAM 107

BIBLIOGRAPHY 124

LIST OF FIGURES

Figure Page

1. Metal – dielectric plane interface geometry 14
2. Real and imaginary parts of metal dielectric functions 20
3. SPP amplitude and vector field at a silver/vacuum interface 21
4. Dispersion curves for light and surface plasmons 23
5. Otto and Kretschmann configurations for prism coupling 24
6. Reflection from two and three layer interface 25
7. Reflection amplitude from a glass/air and a glass/silver interface 26
8. Amplitude reflection for varying silver film thickness 28
9. Amplitude reflection for varying dielectric constants 29
10. Schematic of the STM housing 36
11. Actuating the probe tip 37
12. Electrochemical etching of the tungsten STM probe tip 39
13. STM scan of diffraction grating 41
14. Diagram of our experimental apparatus 44
15. Amplitude and phase of illuminated region 50
16. Amplitude and intensity of propagating reflection profile 52
17. Depiction of common terms used in this thesis 53
18. Average cone ring intensity vs. probe tip distance from the surface 56
19. STM and SPOM/NSOM images of a vacuum deposited silver film 56
20. Isolation of large topography feature 57
21. SPOM/NSOM images recorded at two different locations around cone 58
22. Surface phase and the origin of the primary stripes 61
23. Analyzing the primary stripes using the Fourier transform 62
24. Primary stripe profile for various locations around the ring 63
25. Comparison of primary stripes, experiment and theory 64
26. Time reversed scattering paths resulting in CBS 66
27. Analyzed direction of SPP back-scattered field 68
28. Hypothetical SPP scattering paths and phasor sum 71
29. Examples of cone ring speckle 73
30. STM topography image of a 40nm silver film 74

Figure Page

31. Hermite-Gaussian and Laguerre-Gaussian laser modes 76
32. Common representations of optical phase singularities 78
33. Phase singularities with skew and topological charge +2 79
34. Network of vortices interacting with a coherent background field 83
35. Locations of optical vortices in the cone speckle 85
36. Annihilation of oppositely charged optical vortices vs. tip movement 86
37. Examples of photometry maps recorded in dark regions of the cone 88
38. Random array of point scatterers used in computer simulation 90
39. Photometry intensity and phase maps from Monte Carlo simulation 91
40. Eliminating the primary stripes from computer generated photometry 93
41. Distribution of intensity and phase of background field 94
42. Emerging vortices due to the reduction of single scattering from tip 95
43. Tip trajectory revealing 2π accumulation of phase 96
44. Computer simulation with four scattering centers plus tip 98
45. Two and three SPP field interference 100
46. Two orthogonal SPP fields with radially scattering probe tip 101

LIST OF TABLES

Table Page

1. Physical properties of a SPP for various metal-vacuum plane interfaces 19

CHAPTER I

INTRODUCTION

I.1. Historical Overview of Surface Plasmon Physics

Understanding of surface plasmon (SP) physics is largely recognized to have begun with the theoretical framework published by Ritchie in his 1957 paper *Plasma Losses by Fast Electrons in Thin Films*[1]. In this paper, Ritchie provided the first theoretical treatment of SP's and showed how fast electrons traveling through thin metal films can lose energy to plasma modes that are confined to the surface of metallic films. Ritchie proposed that in addition to the familiar energy loss of $\hbar\omega_p$ due to the excitation of volume plasmons, energy can also be lost to the excitation of surface plasmons by a reduced amount of $\frac{\hbar\omega_p}{\sqrt{2}}$ where ω_p is the bulk plasma frequency. In 1970 Powell and Swan observed the two energy loss mechanisms for both aluminum and magnesium samples. Powell and Swan also observed a shift in the surface plasmon energy loss due to oxidization of the metal surface [17].

Prior to Ritchie's theoretical treatment, phenomena associated with SP's were well known, but not very well understood. An example of one such phenomenon was the 1902 observation made by Wood [2] regarding the intensity distribution in the reflection spectrum from a metal backed diffraction grating illuminated with white light. Wood noticed that some parts of the spectrum were highly attenuated when illuminated with white light and that this effect was particularly strong when the incident light was polarized perpendicularly with respect to the grating rulings (P polarized).

This anomalous diffraction spectrum is said to display a "Wood's Anomaly". Conventional diffraction theory was insufficient to explain this anomalous diffraction. In 1941 Fano Suggested that Wood's Anomalies were the result of the incident light coupling to Zenneck-Sommerfeld surface waves [3]. However, it wasn't until 1968 that this anomalous diffraction was fully understood as the result of the excitation of grating coupled SPs [4].

Perhaps the oldest and most widely known phenomena involving SP's concern the striking color of certain stained glasses when illuminated with light. As far back as the 4th century, it was common practice to color stained glass by introducing metallic substances during the fabrication process. Even to this day, some stained glass obtains its color by the infusion of metallic salts. It has been found that the presence of gold nanoparticles embedded in the glass produces deep red colors whereas the presence of silver nanoparticles produces yellowish colors - colors that differ from that of the bulk metals themselves. In 1908 Mie recognized that this effect was in part due to the electromagnetic interaction of the field with the metallic nanoparticles, their diameters of which are less than a wavelength of light [5]. However, it wasn't until 1970 that Kreibig and Zacharias related this phenomena to the excitation of highly localized SP oscillations on the metallic nanoparticles [6]. Today, the interaction of light with metallic nano particles remains a hot topic of research.

While the theoretical understanding of surface plasmons has successfully provided explanations for previously unexplained phenomena, its true success lies in the diverse fields which it has subsequently motivated. What follows is a small sample of some of the important discoveries and applications regarding the field of SP physics.

In 1968, Otto devised a method for optically exciting SPs at a smooth metal-vacuum interface [7]. He proposed bringing a glass prism within close proximity of a metal surface to couple the optical field to SP modes. He reasoned that light

undergoing total internal reflection inside the prism could evanescently excite SP waves on the metal surface when the in-plane momentum is matched. Later that year, Kretschmann and Raether modified Otto's geometry, depositing a thin metal film directly on the coupling prism [8]. In Kretschmann and Raether's new configuration, SPs are evanescently excited on the exposed surface of the metal film. As it turns out, the Kretschmann-Raether geometry has proved to be the more useful of the two prism coupled configurations, due to its easy of implementation and to the fact that the SP field is exposed on the side of the metal film opposite the prism and is therefore available for further interaction. There are, however, cases for which the Otto configuration is preferred, for instance, in the generation of coupled long range SPs in multilayer configurations.

Another important discovery involving SPs is the large enhancement of the Raman scattered signal from molecules on a surface. Raman scattering typically is a weak process where a molecule emits radiation of a slightly different frequency from that of the excitation due to a shift caused by the molecule's vibrational modes. In 1974, Fleischman et al. discovered a large enhancement to the Raman scattering from pyridine molecules adsorbed on a roughened silver surface [9]. Jeanmaire and Van Duyne subsequently proposed that the enhancement was caused in part by the large electric field associated with localized SPs. The effect has come to be known as Surface Enhanced Raman Scattering, or SERS for short [10]. It is common for SERS to give enhancement factors of 10^6 to 10^7, with factors as high as 10^{14} for single molecule Raman scattering [16]. However, a full and comprehensive understanding of the role that localized SPs plays in the large enhancement factors of Raman scattering is still lacking.

Surface plasmons have also played an important role in Near Field Scanning Microscopy (NFSM) for certain types of surfaces. The beginning of NFSM can be traced

back to 1984 with the development of the Near Field Scanning Optical Microscope (NSOM/SNOM) by Pohl [11] and simultaneously by Lewis [12]. The capabilities of an NSOM verified the 1928 proposition made by E. H. Synge [13] regarding a method for beating the Abbé diffraction limit that restricts one's ability to resolve objects much smaller than a wavelength of light using conventional optics. In 1991 Specht, et al. demonstrated that similar near field microscopy can be accomplished based on the detection of scattered SPs on a thin silver surface by a raster scanned probe tip [14]. This new method of near field microscopy, known as Scanning Plasmon Near Field Microscopy (SPNM), or equivalently, Scanning Plasmon Optical Microscopy (SPOM), compliments previous near field microscopes and can accomplish lateral resolutions as small as 3nm, or roughly $\frac{\lambda_{sp}}{200}$ where λ_{sp} is the SP wavelength.

In 1990 SPs emerged from a purely research based discipline and into an area with commercial value. That year, the Swedish life science company Pharmacia Biosensor, later reforming as Biacore and ultimately acquired by GE Healthcare in 2006 for 390 million dollars, released an analyte detection instrument based on Surface Plasmon Resonance (SPR). This instrument, and many similar ones which have followed, utilized the extraordinary sensitive response of SPR to the dielectric properties of the medium in contact with the surface supporting SPs. Originally aimed at biochemical applications, SPR based detectors now have many applications ranging from contamination detection to the detection of chemical processes and reactions.

As with many discoveries in physics, some discoveries involving SPs come about largely by surprise. An example of this was the 1998 discovery by Ebbesen, et al. [15] on the unusually high optical transmission through a two dimensional array of sub wavelength holes in a silver film. They found that the intensity of the transmitted light, which was collinear with the incident beam, exceeded the value predicted by standard aperture theory. In fact, the intensity was more than twice that of the

incident light impinging on the apertures. They were able to relate this enhanced transmission to the presence of SPs facilitating the transfer of the optical field through the apertures. It should be noted that other studies have suggested that while SPs may assist in this enhanced transmission for some materials, it has been found that it is possible to achieve enhancements in transmission at optical frequencies for materials that do not support SPs [18].

The preceding brief review of some of the developments in the field of SP physics is intended to illustrate the dynamism and variety the field has to offer. It is also intended to show the promise SP physics have in the realm of technology, particularly for nanoscale applications. For example, there is an ever increasing demand for faster computers and faster and better communications and this demand has spurred many to rethink electronic design. Traditionally, the way to increase speed depended on shrinking semiconductor devices and shortening traces. Other purely electrical techniques include, increasing the number of cores on a single die, integrating more components directly on a chip (the so called system-on-a-chip similar to, but not to be confused with microcontrollers which are also called systems-on-a-chip), capacitively coupling components together thereby reducing the size of their interconnects, and fabricating integrated circuits in all three dimensions (as opposed to quasi two dimensional integration). All these techniques are essentially tricks to shorten the distance within and between components to increase speed. However, there are many problems associated with further miniaturization, such as, increased leakage currents, problems with adequate thermal dissipation, and the technical difficulty of improving lithographic techniques necessary for further miniaturization.

It is thought that the integration of photonic components within electronics may address many of the above issues. Photonic alternatives to electronic circuits could greatly increase the speed of computation and communication and possibly be a foun-

dation for quantum computing. The move to photonics would initially require an integration of photonic components with electronic components. Unfortunately, this is complicated by diffraction effects resulting from the mismatch in size between dielectric based photonic devices and nanoscale electronics. SPs, which are not subject to these same diffraction constraints, may facilitate this integration creating "plasmonic" based systems.

I.2. Our Study of Surface Plasmon Polaritons

Despite all that has been accomplished in the field of SP physics, there are still many questions worth pursuing particularly in the realm of scattering. For instance, very little research has been conducted on the hollow cone of radiation that is emitted from scattered SPs in prism-coupled configurations. This hollow cone of light results from the in-plane scattering and subsequent (radiative) decay of the SPs. The scattering of SPs is caused by the grain boundaries, impurities, defects and topographical structures that characterize the metal film surface. The scattering of SPs can also be caused by the introduction of an object such as the tip of a Scanning Tunneling Microscope (STM). The hollow conical shape of the emitted radiation is a result of the fact that not only must the energy be conserved during the conversion of a SP to a free space optical field, but also the in-plane momentum which is matched when the appropriate angle with respect to the normal to the surface is achieved. Much of the past work regarding this radiation entailed the full collection of the conical light in SPOM type measurements. Little concern has been given to the characteristics of the radiation itself and the underlying relation to the behavior of the SPs on the surface that generated it. It is our contention that if this light is properly understood, it would provide us with a means of obtaining information about the propagation, interaction, and scattering processes undergone by the SPs on the metal film.

Our initial goal in the lab was to find out how the interference within the cone of radiation changed when a probe tip scatterer is placed and moved amongst the SPs. We also wanted to discover what this told us about the scattering and transport properties of the SPs on the metal surface. Initially, we supposed that there would be some kind of measurable transconduction-like signal for the SPs as we moved our scatterer within the path of the SPs. We imagined an effect similar to the transconduction fluctuations that ballistic electrons undergo when their paths through an electronic billiard device are perturbed by an applied magnetic field. Our apparatus proved quite useful for studying many aspects of SP propagation, scattering and radiative decay.

The basic design of our experimental apparatus consists of a thin silver film deposited on a fused silica hemisphere upon which SPs are optically excited (Kretschmann style configuration). The hemisphere is mounted onto a vacuum canister which houses a Scanning Tunneling Microscope (STM). The tip of the STM is mounted so that it can be brought within tunneling distance of the metal film and directly interact with the evanescent field of the SPs. The surface plasmons are excited with a tightly focused beam from a HeNe laser and the resultant radiative field is collected by a CCD camera or/and an optical fiber leading to a photo multiplying tube. Modifications to this basic design were made depending on the line of investigation we were studying at the time. A complete description of our device will be covered in more detail in chapter III.

I.3. Outline for the Dissertation

Chapter I (current chapter) provides a brief historical overview on many of the important discoveries regarding surface plasmon physics. I also provide motivation for our own experimental endeavors and outline the contents of this dissertation.

Chapter II provides a brief introduction to the theoretical derivation of surface plasmons and many of their important physical properties. The Drude model for deriving the dielectric function of metals is included as well as a discussion of some of the methods for exciting surface plasmons on a metal-dielectric interface. The physical properties of SPs will include a look at the SP dispersion relation, and the propagation and decay lengths of a SP field.

Chapter III describes our experimental apparatus including our Scanning Tunneling Microscope (STM), the vacuum deposition of metal films, and the etching of probe tips.

Chapter IV will cover the topic of Scanning Plasmon Optical Microscopy (SPOM) including our experimental investigations into the interaction of the STM tip with the SP field and our attempt to measure Coherent Back Scattering (CBS) signals. We also discuss the role of single scattering from the probe tip and the appearance of periodic intensity fluctuations (primary stripes) in our optical data.

Chapter V covers our investigation on optical vortices and the related field of optical speckle. Special attention will be given to the change in intensity of the optical signal near vortices in the radiated cone as the STM tip interacts with the SP field. We also discuss our results obtained from Monte Carlo computer simulation used to model SP multiple scattering.

Chapter VI is where we present a summery of our work and final conclusions.

Appendix A contains the c programing language code for our Monte Carlo simulations used to model SPP scattering scenarios.

CHAPTER II

SURFACE PLASMON POLARITONS

II.1. Introduction to Surface Plasmon Polaritons Derivation

A plasmon is a quantum of charge density oscillation and can, for instance, propagate through the conduction electrons in a metal. A surface plasmon (SP) is a plasmon that is confined to the surface of (typically) a metal in contact with an insulating dielectric. The term surface plasmon polariton (SPP) is often used to refer to a surface plasmon excitation coupled to an electromagnetic wave that accompanies the charge oscillations. In general, the scientific literature often refers to SP and SPP interchangeably where SPP is considered to be the more descriptive of the two terms. In this chapter, I will present a classical derivation of the appearance of a SPP at a plane interface between a metal and a dielectric and discuss many of it's properties. Listed in these references are a number of sources consulted that proved invaluable for understanding the electromagnetic theory of SPPs [19, 20, 21, 22, 23, 36, 74]. Maxwell's equations in matter provide an obvious starting point for the derivation of a SPP formation at a metal - dielectric boundary, but first we must recast these equations in a form that lends itself to a tractable solution.

II.2. Maxwell's Equations

Maxwell's equations describes the macroscopic electrodynamics for any classical system. The differential form of Maxwell's equations in matter are:

$$\nabla \cdot \mathbf{D} = \rho \tag{1}$$

$$\nabla \times \mathbf{E} = -\frac{\partial \mathbf{B}}{\partial t} \tag{2}$$

$$\nabla \cdot \mathbf{B} = 0 \tag{3}$$

$$\nabla \times \mathbf{H} = \mathbf{J} + \frac{\partial \mathbf{D}}{\partial t} \tag{4}$$

Where the electric displacement, $\mathbf{D}$, is constitutive of the electric field and the polarization $\mathbf{D} = \epsilon_0 \mathbf{E} + \mathbf{P}$, the magnetic field, $\mathbf{H}$, is constitutive of the magnetic induction and the magnetization $\mathbf{H} = \frac{1}{\mu_0}\mathbf{B} - \mathbf{M}$, ρ is the free charge density, and $\mathbf{J}$ denotes the free current density.

In general, the polarization, $\mathbf{P}$, and the magnetization, $\mathbf{M}$, have a fairly complicated dependence upon the applied electric and magnetic fields, making analytical solutions to Maxwell's equations difficult to find. For our purposes, it is desirable to consider materials that are approximately linear, homogeneous, and isotropic. When these conditions are met, the polarization becomes a linear function of the electric field, written as, $\mathbf{P} = \epsilon_0 \chi_e \mathbf{E}$ where χ_e is a scalar quantity known as the electric susceptibility. With the introduction of the permittivity $\epsilon = \epsilon_0(1 + \chi_e)$, the electric displacement within the material can be written entirely in terms of the applied electric field as $\mathbf{D} = \epsilon \mathbf{E}$. Similarly, the magnetization can be approximated as being linearly dependent on $\mathbf{B}$ by the magnetic susceptibility. The magnetic susceptibility for most non-ferrous materials, however, have values on the order of 10^{-5} and can safely be ignored, that is, $\mathbf{H} = \frac{1}{\mu}\mathbf{B}$ where $\mu \simeq \mu_0$.

In addition, we consider materials in which free charge is absent. For conductors, any accumulated charge can be removed by grounding and for dielectrics, internal charge neutrality is required ensuring $\rho = 0$.

While it is not necessary for the media forming the interface to adhere strictly to all of the preceding conditions in order for SPPs to exist, this does result in easier methods for obtaining solutions to Maxwell's equations.

Before proceeding any further, we mention that the solving of Maxwell's Equations can be greatly simplified if we can set $\mathbf{J} = 0$. Thus, a discussion regarding free currents in metals is in order. Surface plasmons are supported in part by a conducting medium, and as we know, electromagnetic fields will drive currents in conductors. This implies that free currents will flow in the conductor and would seem to suggest that $\mathbf{J}$ cannot be zero. Yet, it isjustifiable to set $\mathbf{J}$ to zero so long as the free current is accounted for elsewhere in the formulation, as we shall do here by adopting a complex-valued dielectric function. This assertion is justified as follows:

Consider the current in a metal as proportional to an applied electric field. We can express this as $\mathbf{J} = \sigma_c \mathbf{E}$ where σ_c is the electrical conductivity of the metal and $\mathbf{E}$ is the applied electric field. This is simply a statement of Ohm's law. Applying the above substitutions ($\mathbf{D} = \epsilon \mathbf{E}$, $\mathbf{H} = \frac{1}{\mu}\mathbf{B}$, and $\mathbf{J} = \sigma_c \mathbf{E}$) into Maxwell's equations we arrive at the following expression for equation 4.

$$\nabla \times \mathbf{B} = \mu \sigma_c \mathbf{E} + \mu \epsilon \frac{\partial \mathbf{E}}{\partial t} \tag{5}$$

Taking the curl of equation 2 and substituting this into equation 5 leads to the damped wave equation

$$\nabla \times \nabla \times \mathbf{E} = -\mu \sigma_c \frac{\partial \mathbf{E}}{\partial t} - \mu \epsilon \frac{\partial^2 \mathbf{E}}{\partial t^2}. \tag{6}$$

The electric field can be written in the form of a Fourier integral with respect to its frequency components $\mathbf{E}(\mathbf{r},\omega)$, namely

$$\mathbf{E}(\mathbf{r},t) = \int_{-\infty}^{\infty} \mathbf{E}(\mathbf{r},\omega) e^{i\omega t} d\omega. \tag{7}$$

This allows the time derivatives of equation 6 to be evaluated, giving

$$\boldsymbol{\nabla} \times \boldsymbol{\nabla} \times \mathbf{E} = \omega^2 \mu \epsilon \mathbf{E} - i\omega\mu\sigma_c \mathbf{E}. \tag{8}$$

Finally, we notice that equation 8 can be written in the form of equation 6, but without the term containing the free current density provided that the dielectric function takes on complex values of the form given in equation 10, that is

$$\boldsymbol{\nabla} \times \boldsymbol{\nabla} \times \mathbf{E} = -\mu\epsilon' \frac{\partial^2 \mathbf{E}}{\partial t^2} \tag{9}$$

provided that

$$(\epsilon - i\frac{\sigma_c}{\omega}) \rightarrow \epsilon'. \tag{10}$$

The use of complex valued dielectric functions to account for any induced currents in conductors is common practice and is found to come about quite naturally from the Drude - Sommerfeld model for metals. We will use this convention for describing the dielectric function of metals throughout the remainder of this dissertation.

II.3. Simplified Maxwell's Equations in Matter

Once our conditions for a linear, homogeneous, isotropic medium without free charge and current densities are used, Maxwell's equations reduce to the following simpler form.

$$\boldsymbol{\nabla} \cdot \mathbf{E} = 0 \tag{11}$$

$$\boldsymbol{\nabla} \times \mathbf{E} = -\frac{\partial \mathbf{B}}{\partial t} \tag{12}$$

$$\boldsymbol{\nabla} \cdot \mathbf{B} = 0 \tag{13}$$

$$\boldsymbol{\nabla} \times \mathbf{B} = \mu\epsilon \frac{\partial \mathbf{E}}{\partial t} \tag{14}$$

Uncoupling these equations for the electric field, $\mathbf{E}$, and the magnetic induction, $\mathbf{B}$, gives the familiar second order homogeneous wave equations:

$$\nabla^2 \mathbf{E} - \mu\epsilon \frac{\partial^2 \mathbf{E}}{\partial t^2} = 0 \tag{15}$$

$$\nabla^2 \mathbf{B} - \mu\epsilon \frac{\partial^2 \mathbf{B}}{\partial t^2} = 0 \tag{16}$$

From here, it is sufficient to solve either one of the wave equations for either $\mathbf{E}$ or $\mathbf{B}$, as it is a simple matter to derive one solution from the other. We will solve equation 15 for the electric field $\mathbf{E}$ with the following general solution

$$\mathbf{E} = \begin{pmatrix} E_x \\ E_y \\ E_z \end{pmatrix} \exp i(\mathbf{k} \cdot \mathbf{r} - \omega t). \tag{17}$$

As mentioned above, the magnetic field can be determined at any time by using the relation $\mathbf{B} = \frac{1}{\sqrt{\epsilon\mu}} \hat{\mathbf{k}} \times \mathbf{E}$ where $\hat{\mathbf{k}}$ is the unit vector pointing in the $\mathbf{k}$ (propagating) direction.

Metal-Dielectric Plane Interface Geometry

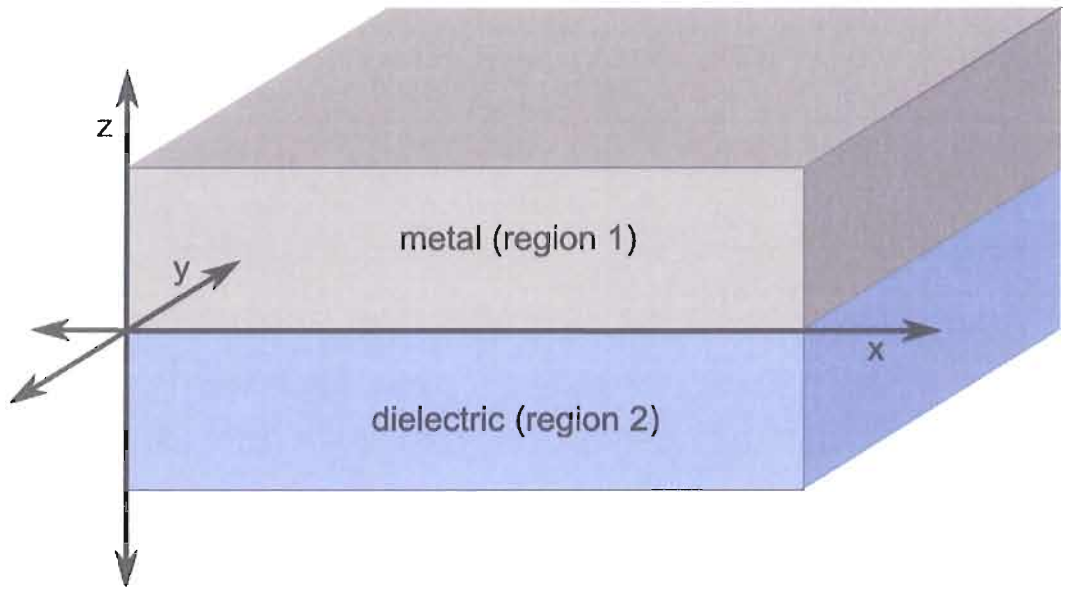

Figure 1: Metal - dielectric plane interface geometry. The plane interface geometry for the metal - dielectric half-space regions meeting at $z = 0$ on the x, y plane.

II.4. Finding Solutions For a Metal - Dielectric Interface

To progress any further, the general solution must be subjected to the boundary conditions as defined by the geometry of the system. We consider a plane interface between a metal and a dielectric where the plane interface extends in the x, y plane located at $z = 0$ (see figure 1). The upper half-space region ($z > 0$) is occupied by the metal with parameters ϵ_1 and μ_1 and the lower half-space region ($z < 0$) is occupied by the dielectric with parameters ϵ_2 and μ_2.

We can take advantage of the symmetry of the interface and orient the wave vector so that it lies within the (x, z) plane, i.e. $\mathbf{k} = \mathbf{k_x} + \mathbf{k_z}$. The S and P-polarized states are subjected to different boundary conditions. It can be shown that the condition for the S-polarized state leads to $E_y = 0$ in equation 17, that is, to no finite solution. This can be understood physically by realizing that S-polarized fields cannot contribute to an accumulation of charge at the interface. We conclude that for a solution to exists,

it must be P-polarized and we can further reduce equation 17 to

$$\mathbf{E}_j = \begin{pmatrix} E_{j,x} \\ 0 \\ E_{j,z} \end{pmatrix} \exp i(k_x x + k_{j,z} z - \omega t), \qquad j = 1, 2. \tag{18}$$

Where the index j denotes the region as defined in the geometry of figure 1.

We have also exploited the facts that the wave vector parallel to the interface, k_x, and the angular frequency, ω, are the same for each half-space region. These are a consequence of the requirement that the argument within the exponential factor of equation 18 on each side of the interface must be equal for all points on the interface and for all times [23].

The conditions $\hat{\mathbf{n}} \times (\mathbf{E}_2 - \mathbf{E}_1) = 0$ and $\hat{\mathbf{n}} \cdot (\mathbf{D}_2 - \mathbf{D}_1) = 0$ where $\hat{\mathbf{n}}$ is defined as the unit vector normal to the interface pointing from region 1 to region 2 must be met for the fields described in equation 18. This leads to the condition for the field components parallel and perpendicular to the interface, namely

$$E_{1,x} - E_{2,x} = 0, \tag{19}$$

and

$$\epsilon_2 E_{2,z} - \epsilon_1 E_{1,z} = 0. \tag{20}$$

The requirement from Maxwell's equation (equation 11) that the divergence of the electric field must vanish gives the following relationship between E_x and E_z for each half-space

$$k_x E_{j,x} + k_{j,z} E_{j,z} = 0, \qquad j = 1, 2. \tag{21}$$

For equations 19, 20, and 21 to simultaneously hold true for non zero electric fields, we require

$$\epsilon_2 k_{1,z} - \epsilon_1 k_{2,z} = 0. \tag{22}$$

Furthermore, we note that the components of the field in each half space are related by

$$k_x^2 + k_{j,z}^2 = \epsilon_j \left(\frac{\omega}{c}\right)^2, \qquad j = 1, 2. \tag{23}$$

Employing equations 19 and 21 we can solve for the respective electric field amplitudes and scale them according to an over all factor E_0. Equations 22 and 23 allows us to determine the wave numbers k_x, $k_{1,z}$, and $k_{2,z}$ in terms of the permittivities ϵ_1, ϵ_2, and angular frequency ω. Thus, when we put this all together, we can cast equation 18 in it's final form as

$$\mathbf{E}(x, z, t) = E_0 \begin{pmatrix} 1 \\ 0 \\ \frac{-k_x}{k_{j,z}} \end{pmatrix} \exp i\left(k_x x + k_{j,z} z - \omega t\right), \qquad j = 1, 2 \tag{24}$$

where $k_x = \frac{\omega}{c}\sqrt{\frac{\epsilon_1 \epsilon_2}{\epsilon_1 + \epsilon_2}}$, and $k_{j,z} = \frac{\omega}{c}\frac{\epsilon_j}{\sqrt{\epsilon_j + \epsilon_2}}$, for $j = 1, 2$.

The values of ϵ_1 and ϵ_2 can drastically effect the behavior of equation 24. For metals, the Drude - Sommerfeld model predicts a complex valued dielectric function. As for the dielectric material, we will assume a lossless real valued dielectric function. With these considerations in mind, we observe that k_x, $k_{1,z}$, and $k_{2,z}$ are all complex valued (therefore, they all have propagating parts and decaying parts.) In order for equation 24 to sustain propagating bound modes, we require a combination of ϵ_1 and ϵ_2 such that the magnitude of the real part of k_x is large compared to the magnitude of its imaginary part, and for the magnitudes of the imaginary parts of $k_{1,z}$, and $k_{2,z}$ to be large compared to the magnitudes of their real parts. As we will see, these conditions are met for silver-vacuum interfaces and can therefore, support SPP propagation.

II.5. Drude - Sommerfeld Model for a Metallic Dielectric Function

We now shift our attention to the dielectric function of metals. The electrical response of metals to an electromagnetic field can be largely understood by the Drude - Sommerfeld model. Using this model, we can predict the value of the complex dielectric function from basic principles. We will consider this model as composed of two parts. First, the simple Drude model which accounts for the contributions to the dielectric function by the free conduction electrons, and second, the contribution from electrons that undergo interband transitions.

We begin by considering the simple Drude model. The equation for driven, dampened motion of a single condition electron subject to an oscillating electric field is

$$m_e \frac{\partial^2 \mathbf{r}}{\partial t^2} + m_e \Gamma \frac{\partial \mathbf{r}}{\partial t} = e\mathbf{E}_0 e^{-i\omega t}. \tag{25}$$

Where m_e is the effective mass of the conduction electron, e is the electron charge and Γ is the collision frequency defined as the Fermi velocity divided by the electron mean free path. For simplicity, the effect of the magnetic field on the driven conduction electron is considered small and will therefore be ignored. Solving this equation for the electron displacement $\mathbf{r}$ as a function of time gives

$$\mathbf{r}(t) = \frac{-e\mathbf{E}_0(\omega - i\Gamma)}{m_e\omega(\omega^2 + \Gamma^2)} e^{-i\omega t}. \tag{26}$$

We can determine the polarization of the metal due to the conduction electrons by $\mathbf{P}(t) = ne\mathbf{r}(t)$. Where n denotes the free electron number density. Assuming a linear polarization, $\mathbf{P}(t) = \epsilon_0 \chi_e \mathbf{E}(t)$, the permittivity defined by $\epsilon = \epsilon_0(1 + \chi_e)$ along with the displacement given by equation 26 produces

$$\epsilon = \epsilon_0 \left(1 - \frac{\omega_p^2}{\omega^2 + \Gamma^2} + i\frac{\Gamma\omega_p^2}{\omega(\omega^2 + \Gamma^2)}\right). \tag{27}$$

Where, $\omega_p = \sqrt{\frac{ne^2}{m_e \epsilon_0}}$ is the bulk plasma frequency of the metal.

While the response of a metal to an electromagnetic field is largely determined by its conduction electrons, the simple Drude model fails to accurately predict features of the dielectric function for noble metals at frequencies near those of the visible region. In this frequency range there will be a contribution due to interband transitions. e.g. $3d \rightarrow 4sp$ for copper in the visible, $5d \rightarrow 6sp$ for gold, also in the visible, and $4d \rightarrow 5sp$ for silver, in the ultraviolet. It is a simple matter to include the response of "interband" electrons (i.e those undergoing interband transitions) to the electromagnetic field by introducing a "spring constant" term to the equation of motion found previously in equation 25. Specifically,

$$m_e^{'} \frac{\partial^2 \mathbf{r}}{\partial t^2} + m_e^{'} \Gamma^{'} \frac{\partial \mathbf{r}}{\partial t} + \alpha \mathbf{r} = e \mathbf{E}_0 e^{-i\omega t}. \tag{28}$$

For this new equation, the effective mass $m_e^{'}$ and the damping coefficient $\Gamma^{'}$ for the interband electrons are recognized to be different from those of the free conduction electrons found in equation 25. Here, the "spring constant", α, is determined by the natural resonant frequency $\omega_0 = \sqrt{\frac{\alpha}{m_e^{'}}}$ of the interband electrons.Using a similar solution to that for the free electron contribution, the contribution to the permittivity for interband electrons is given by

$$\epsilon^{'} = \epsilon_0 \left(1 + \frac{\omega^{'2}(\omega_0^2 - \omega^2)}{(\omega_0^2 - \omega^2)^2 + (\omega \Gamma^{'})^2} + i \frac{\omega^{'2} \omega \Gamma^{'}}{(\omega_0^2 - \omega^2)^2 + (\omega \Gamma^{'})^2} \right). \tag{29}$$

Where, $\omega^{'} = \sqrt{\frac{n^{'} e^2}{m_e^{'} \epsilon_0}}$ is written to mimic the form of the bulk plasma frequency, and $n^{'}$ denotes the number density of the bound electrons.

A quick note regarding notation, strictly speaking, the dielectric constant is defined as the permittivity, ϵ, divided by ϵ_0, however, it is customary to refer to the dielectric constant simply as ϵ. Where there is no confusion, we too will refer to the

Interface mediums.	SPP wavelength.	SPP propagation length.	Decay length in metal.	Decay length in vacuum.
Silver/Vacuum	615.3 nm	125.5 μm	22.9 nm	419 nm
Gold/Vacuum	605.7 nm	20.2 μm	28 nm	332.4 nm
Copper/Vacuum	605.6 nm	14.8 μm	28.2 nm	331.6 nm
Aluminum/Vacuum	558.9 nm	1.7 μm	43.9 nm	185.8 nm

Table 1: Physical properties of a SPP for various metal - vacuum plane interfaces. All decay lengths are determined for when the amplitude of the field decays to within $\frac{1}{e}$ of its original value. The value of the metal's dielectric function is picked based on a prism coupled excitation by a 632.8 nm HeNe laser beam and will be different for different optical frequencies. The dielectric functions for silver, gold and copper come from reference [67] and the dielectric functions for aluminum comes from reference[68].

dielectric constant by the unitless symbol ϵ.

Figure 2 shows a plot of the measured complex dielectric functions for silver, gold, and copper along with calculated values for gold based on the dielectric function due to conduction electrons (equation 27) and the more complete formulation given by adding on the contribution due to interband electrons (equation 27 plus equation 29.)

II.6. Comments on The SPP Field

As stated before, the conditions for a propagating bound mode at a metal - dielectric interface depends on the values of the dielectric functions for each medium. A plot of equation 24 for SPPs on a silver - vacuum interface with $\epsilon_1 = -18.3 + i0.494$ and $\epsilon_2 = 1$ is shown in figure 3. Table 1 indicates several physical properties of SPPs for various plane interface mediums. These properties are based on the wave numbers as follows: The wavelength of the SPP mode is determined by the real part of k_x with the decay length along the direction of propagation being determined by its imaginary part. The evanescent decay length into each medium is determined by the imaginary parts of $k_{1,z}$, and $k_{2,z}$respectively.

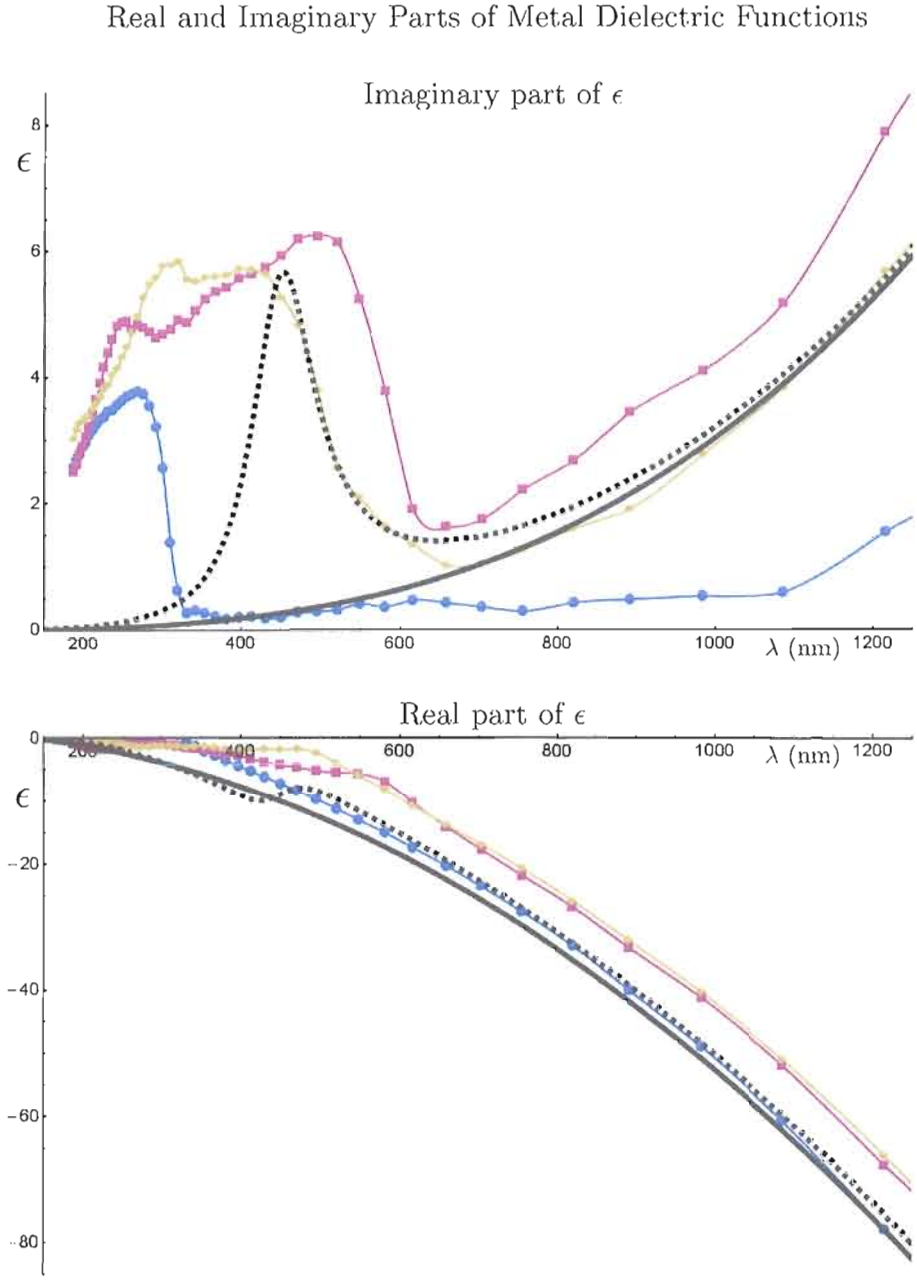

Figure 2: Real and imaginary parts of metal dielectric functions. This Plot shows the complex dielectric function for gold (yellow diamonds), copper (red squares), and silver (blue disks) based on measurements by Johnson et. al. [67]. Accompanying the measurements are plots of the dielectric function for gold based on the Drude - Sommerfeld model for the free electron contribution, equation 27 (solid black line), and the free electron plus interband transition contribution, equation 27 plus equation 29 (dashed black line). The following values are used in the calculations: $\omega_p = 13.8 \times 10^{15} s^{-1}$, $\Gamma = 1.075 \times 10^{14} s^{-1}$, $\omega' = 45 \times 10^{14} s^{-1}$, $\omega_0 = 4.186 \times 10^{15} s^{-1}$ and $\Gamma' = 9 \times 10^{14} s^{-1}$and can be found in reference [20].

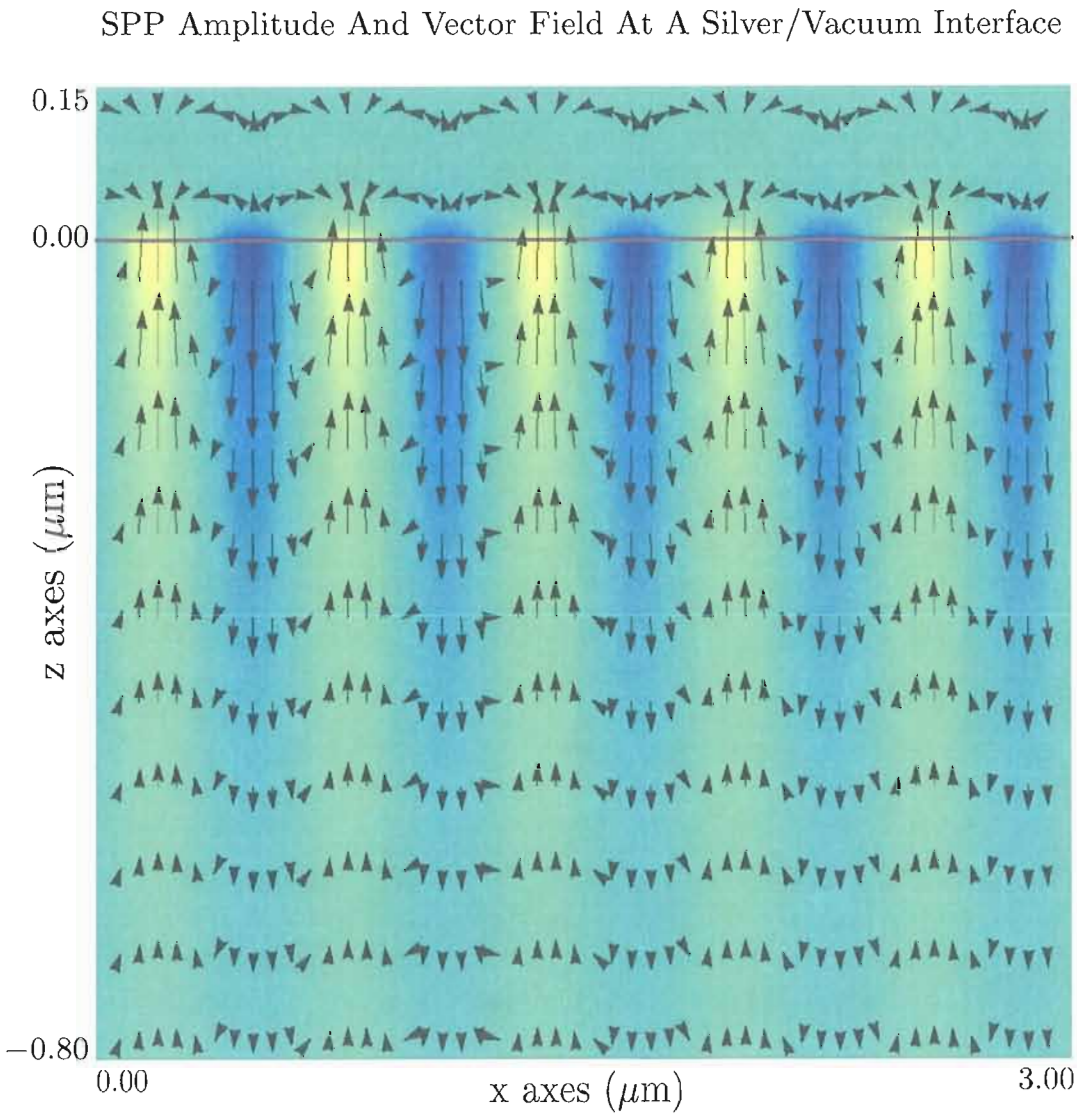

Figure 3: SPP amplitude and vector field at a silver/vacuum interface. This plot shows the field amplitude of SPP (equation 24) on a silver - vacuum interface. The direction and magnitude of the field is indicated by the vector plot and color scale. The magnetic field (not shown) is oriented in and out of the page. The values of the permittivities used in generating this plot are, $\epsilon_1 = -18.3 + i0.494$ and $\epsilon_2 = 1$ corresponding to an optical field with wavelength $\lambda = 632.8$nm.

II.7. Dispersion Relation for SPP

The dispersion relation for a SPP relates its angular frequency, ω, to the propagating part of its wave number along the interface, real part of k_{sp}. The dispersion relation is determined by combining equation22 with 23 and using the fact that $k = \frac{\omega}{c}$. This produces

$$k_{sp} = \sqrt{\frac{\epsilon_1 \epsilon_2}{\epsilon_1 + \epsilon_2}} \frac{\omega}{c}. \tag{30}$$

Figure 4 shows the dispersion curves for SPP modes based on equation30 for two different interfaces, a metal - vacuum and a metal - glass as well as the dispersion curves for light in vacuum and glass.

II.8. Prism Coupled SPP

In order for a free space optical field to excite a SPP mode, both the energy and in-plane momentum must be matched. As shown in figure 4, the dispersion curve for a SPP on the metal - vacuum interface lies entirely to the right of the curve of the free space optical field in vacuum, therefore, direct coupling is not possible. Similarly, the dispersion curve for a SPP residing on a metal - glass interface lies entirely to the right of the dispersion curves for light for both glass and vacuum, and again, direct coupling is not possible. It is, however, possible to excite a SPP mode on the metal - vacuum interface provided that the momentum of the optical field is first increased by passing it through a glass prism. Matching the in-plane momentum of the optical field with the momentum of the SPPs is just a matter of adjusting the incidence angle of the incoming field i.e. $k_{sp} = k_x = k\sqrt{\epsilon_p}\sin(\theta)$ where ϵ_p is the dielectric constant of the prism and θ is the angle of incidence. The idea of using a prism to increase the

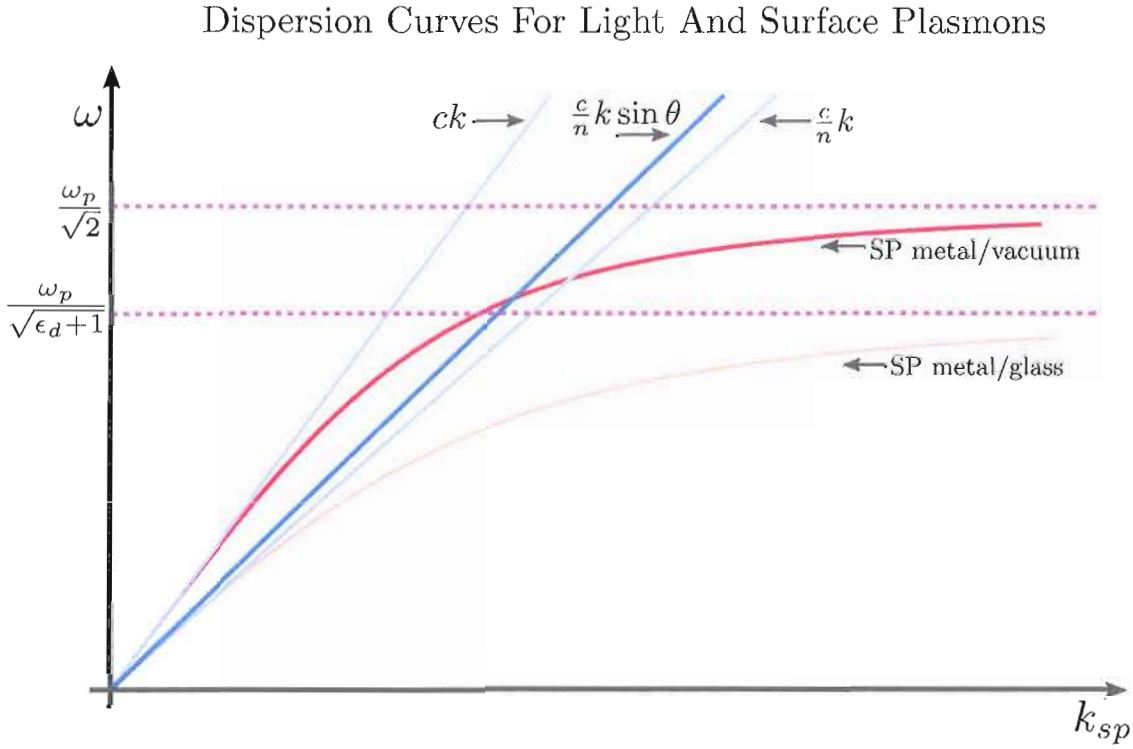

Figure 4: Dispersion curves for light and surface plasmons. The dispersion curve for a light field in vacuum given by $\omega = ck$, and glass given by $\omega = \frac{c}{n}k$. The line depicted by $\omega = \frac{c}{n}ksin(\theta)$ is the projection of the wave vector for light in glass along the k_x direction (k_{sp} direction). The dispersion curves for a SPP at a metal - glass and metal - vacuum interface are also depicted. The dispersion curves for the SPPs were calculated from the simple Drude model given by equation 27 for silver. For low values of k_{sp}, the SPP dispersion approaches the dispersion curve of the optical field in its respective medium and is said to be photon like. For large values of k_{sp}, the SPP approaches the reduced bulk plasma frequency given by $\frac{\omega_p}{\sqrt{1+\epsilon_d}}$ and is refered to as being plasmon like.

Otto And Kretschmann Configurations For Prism Coupling

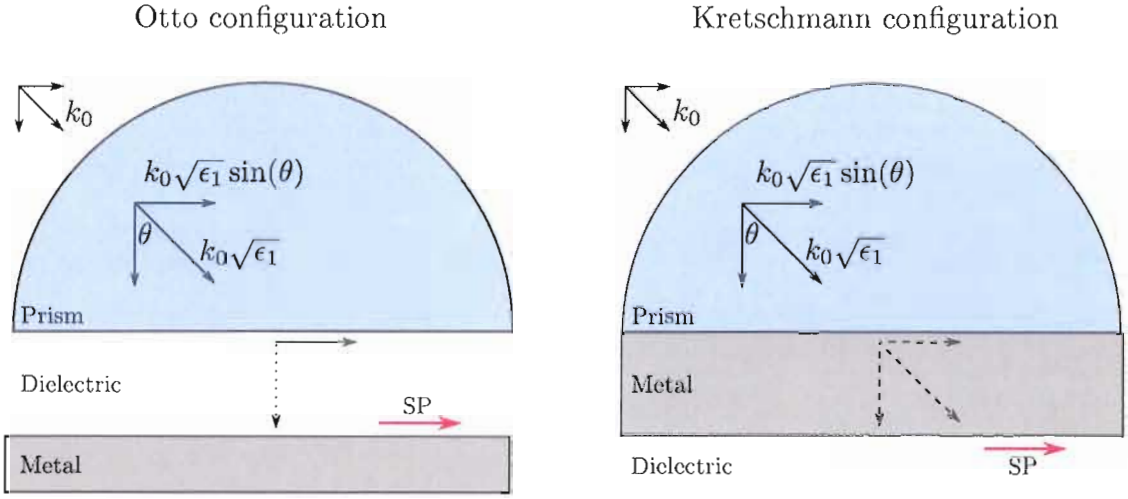

Figure 5: Otto and Kretschmann configurations for prism coupling. These are two common geometries for prism coupling free space optical fields to SPP modes. The red arrow, labeled by "SP", indicates the propagation wave vector of the SPP and the surface on which SPP oscillations reside.

momentum of an optical field in order to excite SPP was put forward by Otto [7] and Kretschmann [8] for two different coupling geometries.

In the Otto configuration (see figure 5), the momentum of the incident beam is increased by the prism. Under total internal reflection, an evanescent field is generated beyond the surface of the prism exciting SPP modes on the near side surface of a semi-infinate metal. For the Kretschmann configuration, the use of the prism is similar to that of the Otto configuration for increasing momentum, however, in this case a thin metal film is deposited directly onto the prism's surface. Since conductors are highly absorptive, the film must be thin enough for the evanescent field to penetrate (typically the film thickness is between 40 and 70nm). In this configuration, the SPPs are excited on the far side of the metal provided that the same momentum resonance condition is met (figure 5).

Reflection From Two And Three Layer Interface

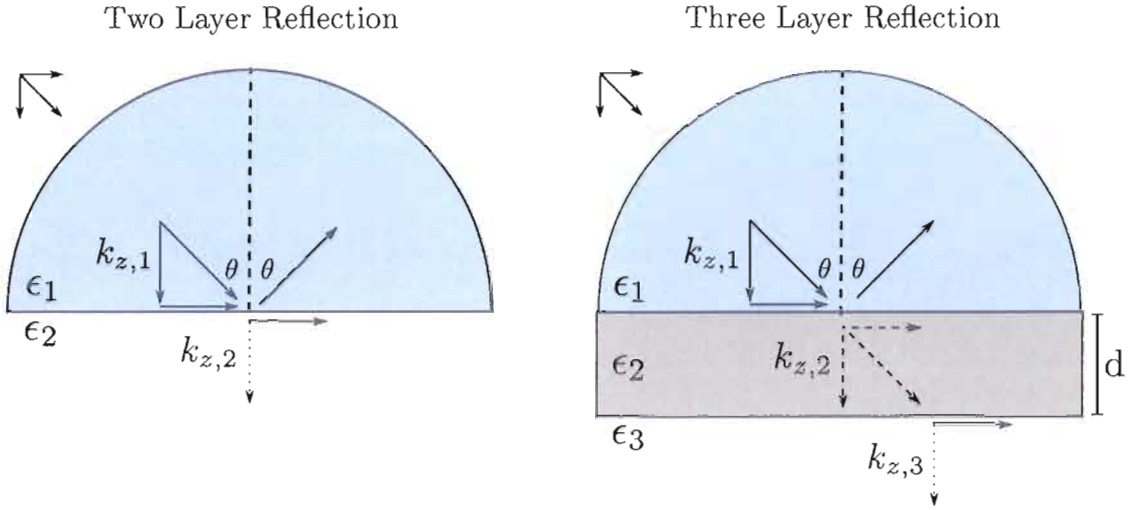

Figure 6: Reflection from two and three layer interface. Here, θ is the angle of incidence (and reflection), $k_{z,i}$ is the z component of the wave vector for the ith medium, ϵ_i is the dielectric constant for the ith medium, and d is the thickness of the second layer.

II.9. Fresnel Equations

The prism coupled geometry lends itself well to the reflection (and transmission) analysis provided by the Fresnel equations. Excitation of SPPs is characterized by the occurrence of attenuated total reflection (ATR). That is, a dip in the reflection for P-polarized light at incident angles greater than the critical angle for total internal reflection. The complex amplitude reflection is defined as $r \equiv \frac{E_r}{E_i}$ where E_r is the reflected electric field amplitude and E_i is the incident electric field amplitude. Figure 6 shows a two and three layer configuration with corresponding (arbitrary) dielectric constants.

The two layer Fresnel amplitude reflection coefficient for a P-polarized planewave reflecting from the $1, 2$ interface in terms of the dielectric constants and the z com-

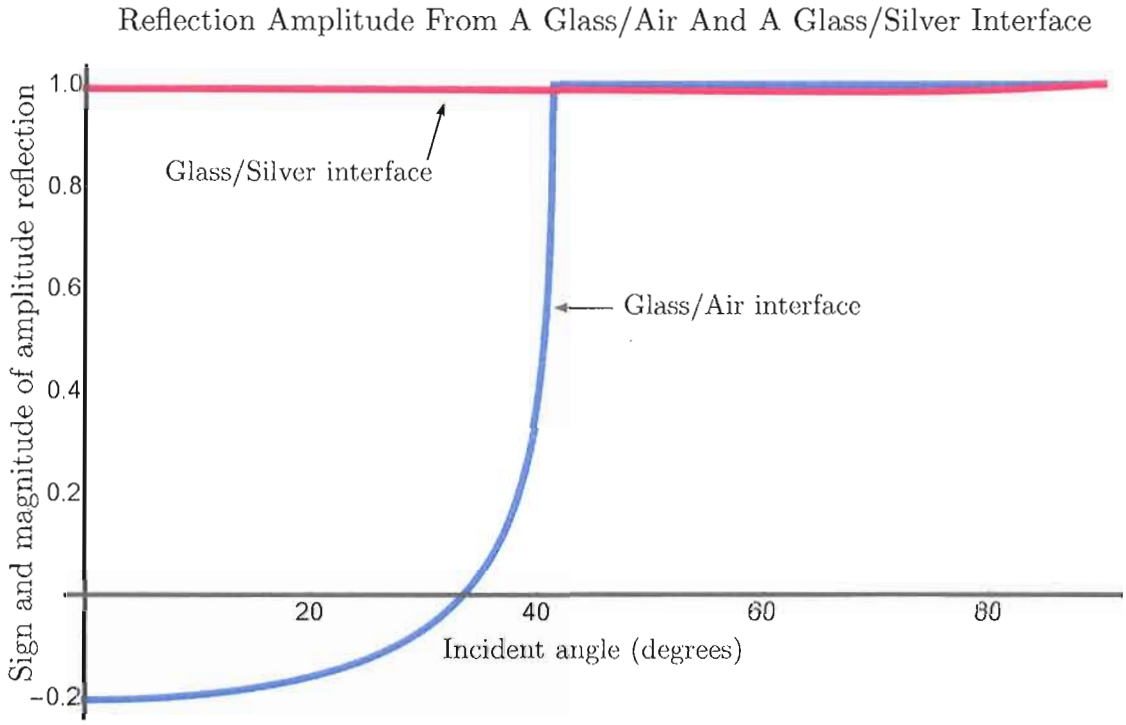

Figure 7: Reflection amplitude from a glass/air and a glass/silver interface. Magnitude of the amplitude reflection for P-polarized planewaves from a single interface. The plot of equation 31 with $\epsilon_1 = 2.30$ (glass), $\epsilon_2 = 1.00$ (air), and $\epsilon_2 = -18.29 + i0.494$ (silver). The z component of the wave vector is given by $k_{z,i} = k_0\sqrt{\epsilon_i - \epsilon_1 \sin\theta}$ for $i = 1, 2$ and $k_0 = \frac{2\pi}{\lambda}$ where λ is the free space wavelength (632.8nm in this case). The negative value in the glass-air reflection indicates a 180 degree phase shift, all other phase information is suppressed.

ponent of the wave vector is given by

$$r_{1,2} = \frac{\epsilon_2 k_{z,1} - \epsilon_1 k_{z,2}}{\epsilon_2 k_{z,1} + \epsilon_1 k_{z,2}} \tag{31}$$

where $k_{z,i} = k_0\sqrt{\epsilon_i - \epsilon_1 \sin\theta}$ for $i = 1, 2$ and $k_0 = \frac{2\pi}{\lambda}$ where λ is the free space wavelength and θ is the incident angle. The plot of equation 31 for a glass-air and glass-silver interface is shown in figure 7.

For a three layer systems, such as the Otto and Kretschmann configurations, the

Fresnel amplitude reflection for a P-polarized plane wave is given by

$$r_{1,2,3} = \frac{r_{1,2} + r_{2,3} \exp(2ik_{z,2}d)}{1 + r_{1,2}r_{2,3} \exp(2ik_{z,2}d)} \tag{32}$$

with $r_{i,j} = \frac{\epsilon_j k_{z,i} - \epsilon_i k_{z,j}}{\epsilon_j k_{z,i} + \epsilon_i k_{z,j}}$, $k_{z,i} = k_0\sqrt{\epsilon_i - \epsilon_1 \sin\theta}$ for $i = 1, 2, 3$ and $k_0 = \frac{2\pi}{\lambda}$ where λ is the free space wavelength. In figure 8 we find the plot of $|r_{1,2,3}|$ vs. incident angle for various silver film thicknesses, d, revealing ATR due to SPP excitation with material layers arranged according to the Kretschmann configuration.

The dip in the reflection is due to the destructive interference between the reflected field from the glass-silver interface (first surface) and the re-radiated leaky field from the excited SPP on the silver-vacuum interface (second surface). There is a critical thickness ($d_{min} = 53.7$nm in this case) for which the reflection vanishes all together. For film thicknesses greater than d_{min}, the reflection increases. This is due to the fact that the evanescent field which excites the SPPs decays exponentially in the metal film resulting in a weaker excitation. Similarly, the re-radiated SPP field is attenuated once more as it evanescently leaks through the metal film to destructively interfere with the first surface reflected field. The double decay through the silver film is expressed by the factor of 2 in the argument of the exponential in equation 32. As the film thickness continues to increase, the glass-silver interface begins to behave more and more like aback surface silvered mirror. The reflectivity increases until the entire reflection is due to the first surface interface (with a small portion of the field being absorbed by the silver film and an absence of SPP excitation).

For film thicknesses less than d_{min}, the increase in reflection is due to the field emitted by the SPP overtaking and dominating the constant reflection from the first surface interface. The reflection off the second surface is in antiphase with the reflection off the first surface, therefore, there is a discontinuous π phase shift in the

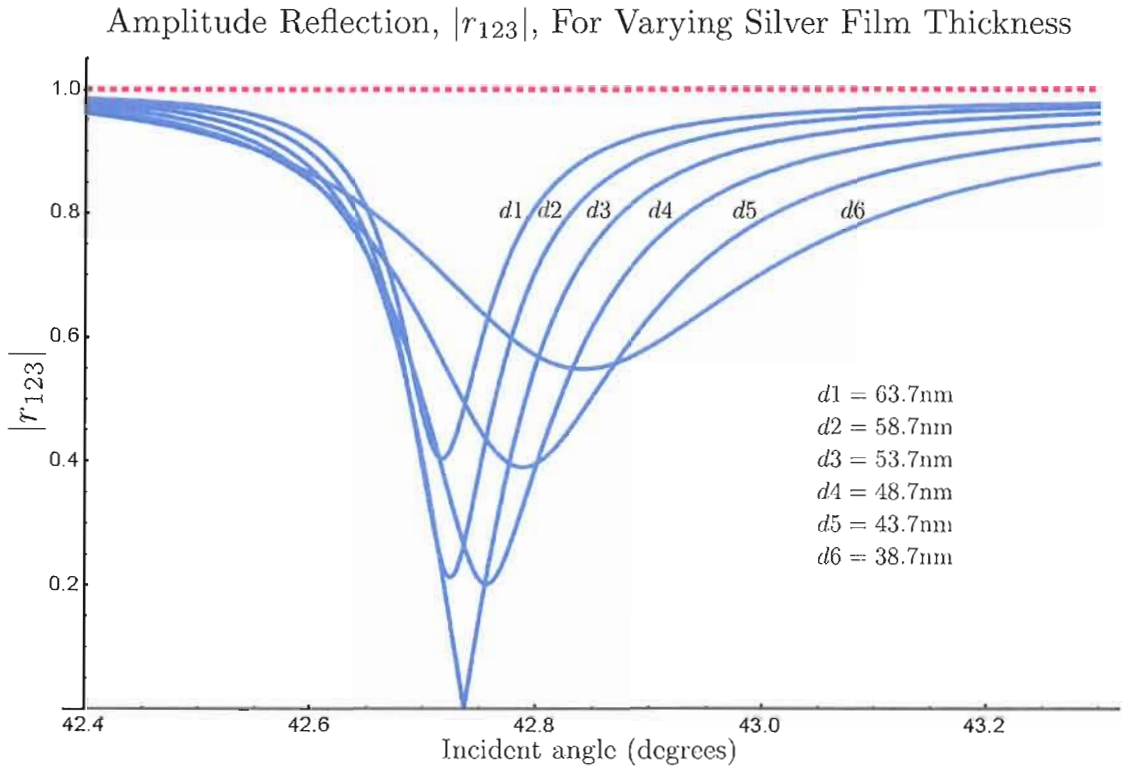

Figure 8: Amplitude reflection, r_{123}, for varying silver film thickness. The three layers are arranged accordingly from glass ($\epsilon_1 = 2.30$), to silver ($\epsilon_2 = -18.29 + i0.494$), to vacuum ($\epsilon_3 = 1$) with the silver thickness varying from d_1 to d_6.

reflected beam minimum as the film thickness increases from below d_{min} to above d_{min}. There are some remarkable consequences that arise from this reflected interference that is pursued further in reference [75].

The Fresnel reflection coefficient is useful for demonstrating the high sensitivity of ATR to the dielectric medium on the interface supporting SPPs and is employed in the analysis of SPP based sensors. Several methods used in analyte/ATR detection include measuring changes in the reflected intensity near the resonant SPP angle [69, 70] and measuring changes in the SPP resonance angle [71, 72] vs. changes in the dielectric (transducing) medium. A good general overview of SPP sensor technology based on ATR on other methods can be found in reference [73]. Figure 9 shows the expected shift in resonance angle for six different dielectric constants.

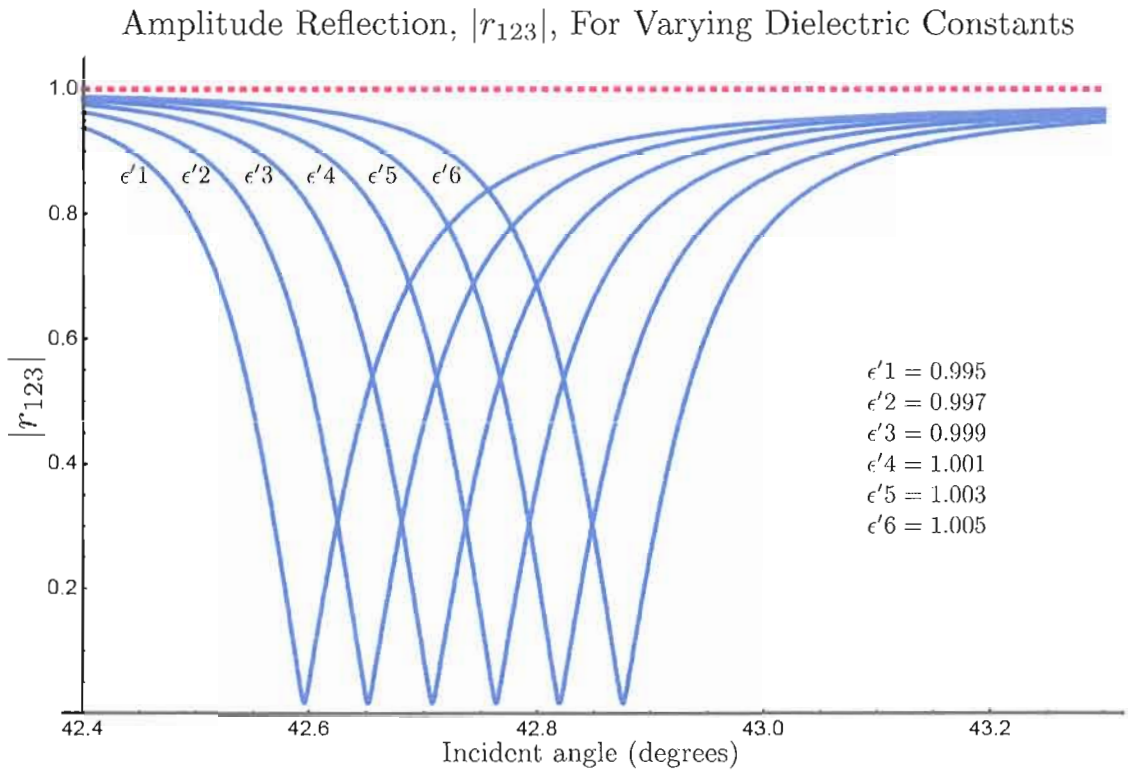

Figure 9: Amplitude reflection, r_{123}, for varying dielectric constants. This shows the shift in SPP resonance angle with respect to changes in the dielectric constant of the metal interfacing region. The three layers are arranged accordingly from glass ($\epsilon_1 = 2.30$), to silver ($\epsilon_2 = -18.29 + i0.494$), to the third dielectric layer labeled by $\epsilon' i$ for $i = 1 - 6$. The silver thickness used in this calculation is $d = 53.7$nm.

For completeness, the Fresnel amplitude reflection for a P-polarized plane wave for an arbitrary number of layers can be iterated as follows

$$r_{j,l,m,\ldots,n} = \frac{r_{j,l} + r_{l,m,\ldots,n} \exp\left(2ik_{z,l}d_l\right)}{1 + r_{j,l}r_{l,m,\ldots,n} \exp\left(2ik_{z,l}d_l\right)} \tag{33}$$

where d_l is the thickness of the lth layer, $r_{i,j} = \frac{\epsilon_j k_{z,i} - \epsilon_i k_{z,j}}{\epsilon_j k_{z,i} + \epsilon_i k_{z,j}}$, $k_{z,i} = k_0\sqrt{\epsilon_i - \epsilon_1 \sin\theta}$, and $k_0 = \frac{2\pi}{\lambda}$ where λ is the free space wavelength as given before. This formula is useful for modeling the ATR for coupled SPP in four layer systems and can even be used for modeling multiple anti-reflective coatings.

CHAPTER III

EXPERIMENTAL APPARATUS

III.1. Introduction

In this chapter, I discuss aspects of the apparatus used in ourexperiments. When necessary, modifications to this basic setup will be dealt with in the relevant chapters that follow. I'll begin with a discussion on STMs, and in particular, the STM used in our SPP experiments. I will present our preferred method for fabricating tungsten probe tips and the steps taken to calibrate the STM. The fabrication of samples is also discussed, and finally, I will describe the working experimental setup as a whole.

III.2. The Scanning Tunneling Microscope

Scanning tunneling microscopy is based on the quantum phenomenon of tunneling, in which a particle, in this case an electron, tunnels through an energy barrier that would classically prohibit its passage. When a forward-biased, sharp, conducting tip is brought within close proximity of a conducting (or semiconducting) surface the electrons in the occupied states of the tip will tunnel to the empty states of the surface resulting in a detectable tunnel current. For a metal tip and a metal surface held at a low bias voltage and small separation distances, the dependence of the tunnel current can be expressed as

$$I \propto \frac{V}{z} \exp(-1.025\sqrt{\bar{\Phi}}z). \tag{34}$$

Where I is the tunnel current (the units of which will depend on the proportionality constant), V is the bias voltage, Φ is the average energy barrier height between the two conductors in units of eV, and z is the gap separation measured in angstroms. The value of Φ in equation 34 is typically a few eV for a wide range of tip and sample materials [27]. It is worth pointing out that Φ is fairly constant over a moderate range of gap distances, but decreases rapidly when the gap distance decreases to within a fraction of a nm [24].

The strong dependence of the tunnel current on the change of the gap separation is due to the exponential factor in equation 34. As an example, a change in the gap distance, z, from 1nm to 0.4nm for an average energy barrier height of, 5eV, will bring about an order of magnitude change in the current I. Because of this strong gap separation dependence, STMs operating under ideal conditions are capable of achieving vertical resolutions on the order of 0.1nm.

There is a fairly wide range of operation parameters over which STMs can function. For example, the operating bias voltage will typically range anywhere from 1mV to 1V, with tunnel currents ranging between 0.1nA and 1nA, and tip to surface separation is commonly between 0.1 to 1nm for most applications.

In the present experiments, we typically set the bias voltage to 300mVand measure tunnel currents on the order of a few hundred pico-amps. Under these conditions, our tip to surface separation, while not known exactly, issuspected to be within 1nm.

STMs can function in different operational modes, among these are: the constant current mode, the constant height mode [25], the differential mode [26], and the work function mode. Weexclusively used the constant current mode in our experiments. In the constant current mode, a negative feedback loop is used to continually adjust the height of the tip above the surface so that a constant tunnel current is maintained. By recording the feedback signal for each x-ytip position within the scan, a topography

of the surface is constructed. This mode of operation also allowed us to track the surface over large regions of the sample while preventing the probe tip from crashing into the sample.

Ultimately, the STM tunnel current depends on the electronic state characteristics of both the tip and the sample. This can often times complicate the interpretation of sample topographies. Particularly in the case of atomic scale scans where prior knowledge of the electronic structure of the tip and surface is required for correctly interpreting the characteristics of the surface scan (and in some cases, the subsurface structure). However, for scans performed on silver surfaces with supra-atomicresolution, knowledge of the details of the electronic states become less important and the resulting tunneling map can usually be interpreted as directly relating to the topography of the surface. This is not to say that there are no distortion effects for large range scans. Distortions due to the convolution of the tip geometry with the geometry of the features on the surface are common, as well as distortions that arise from multiple "micro tips" protruding from the surface of the probe tip. It is important to take into account these and other effects in order to create an accurate depiction of the surface topography. This, however, may not always be possible especially when the tip geometry is ambiguous. There are, however, a number of software tools specifically written for post scan image processing that are able to minimize and remove many kinds of distortions (for instance, the program SPIP from Image Metrology).

III.3. The Scanning Tunneling Microscope Used in Our Lab

Our lab's STM is a home made unit designed and built by Stephen Gregory and his graduate students [76, 77, 78, 79]. After much use, occasional modifications to the electronics, and frequent modifications to the control software, an updated description of our lab's STM is necessary. In this section, I will discuss severalaspects

of our STMincluding the control system and the STM housing chamber. We begin with a discussion of the control system.

The control systeminvolves a combination of software and electronic hardware. The software is written in LabView^{TM}and runs on arelatively slow, archaic computer equipped with A-to-D and D-to-A I/O boards which provides an interface with the hardware component of the control system. The controlsoftware takes care of the many tasks related to the functioning of the STM.Everything from facilitating a safe and controlled tip approach, to executing a metrology scan of the surface. The software is also responsible for coordinating actions of the STM to peripheral tasks such as triggering a CCD camera at periodic intervals. Many of the parameters needed to initialize the STM are also handled by the control software such as setting the bias voltage, the scan range, and the scan resolution. Once these parameters are set, the software is responsible foron-screen depiction and execution of the scan motion and for recording the feedback signal provided by the hardware whichis used in the construction of topographies.

The second part of the control system consists of hardware. One responsibility of the hardware is to take the desiredx-y-ztip position as stipulated by the software and convert it into the required form for driving the piezoelectric tubes that actuate the probe tip. The desired tip position is read from the software in the form of five separate voltage levels from the I/O boards in the PC, two for the x position, two for the y position and one for the z position of the tip. The hardware is also responsible for monitoring the voltage level from the tunnel current amplifier and generating the appropriate feedback signal for controlling the tip to sample separation. The hardware circuitry determines the feedback signal by performing a logarithmic operation on the signal from the tunnel current amplifier. This is to linearize the exponential dependence of the tunnel current on the tip to surface distance (equation 34). From

here, summing amplifiers are used to combine the various signals into four separate channels, one channel for each of the four piezoelectric actuators that controls the tip. Finally, the voltage level of each channel is amplified to drive the actuators.

As mentioned above, the control unit hardware must monitor the (small)tunnel current. Our setup uses an Ithaco current amplifier that takes as an input the tunnel current and outputs a corresponding voltage level. Setting the sensitivity of our current amplifier to 10^{-10} amps per volt is found to produce good topographical scan results for scan ranges between 50nm and 2μm. It should be mentioned that this setting for the sensitivity is a "ball park" figure as optimal scanning entails striking a balance between all of the various setting of all of the components.

The current amplifier has an internal rise time filter for removing noise and current spikes. Through trial and error, we have found that a rise time setting of 0.3 ms provided a good compromise between amplifier responsiveness and amplifier lag. Again, this is a "ball park" figure dependent on other operating factors.

The final part of our STM consists of the vacuum chamber containing the scan head as pictured in figure 10. The unit holds the sample, the probe tip, and the piezoelectric actuators. The probe tip fits into a holder that affixes to the central post of a four quadrant rocker. One end of a cylindrical piezoelectric tube is bonded to each arm of the rocker and the other end is bonded to a spring loaded platform equipped with a micrometer that allows for coarse adjustment in the z direction. The piezoelectric tubes attached to opposite ends of the rocker contract and expand accordingly to cause the tip to sweep in the x and y directions (see figure). Additionally, the unit is designed so that the atmosphere within the STM chamber can be controlled. Once the sample is clamped into place, a seal is formed and the chamber can be pumped down tocreate a vacuum or back-filled to provide a gaseous environment. This is important for reducing contaminant buildup on our samples and for controlling the

Schematic Of The STM Housing

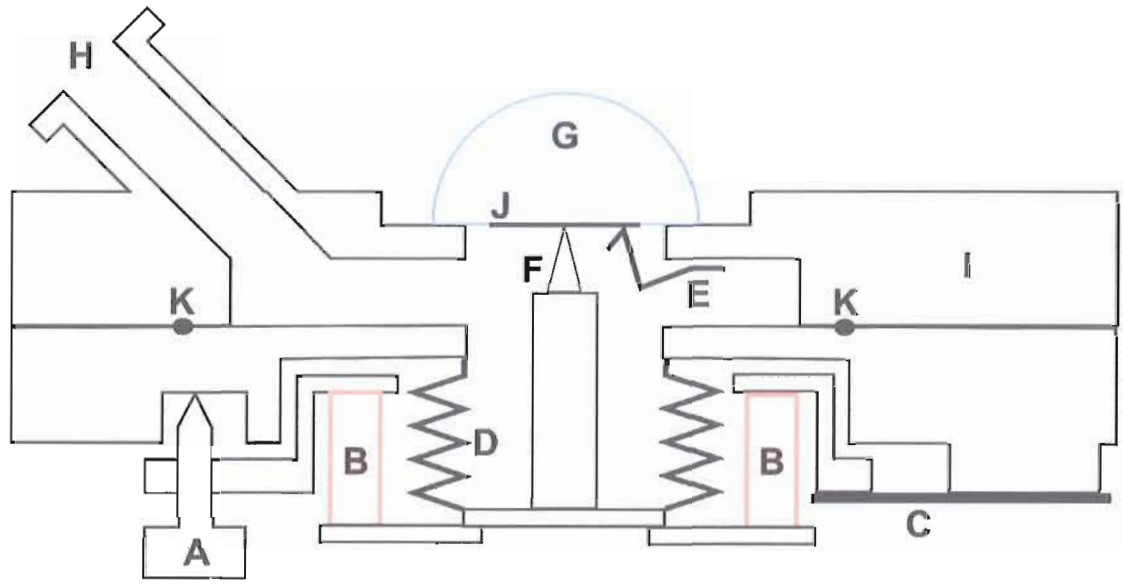

Figure 10: Schematic of the STM housing (not to scale). **A** is the micrometer for coarse z positioning of the probe tip. **B** indicates the hollow cylindrical piezoelectric tubes (only two of the four piezoelectric tubes are shown in this cross sectional diagram). **C** is a flat spring hinge for tensioning the micrometer. **D** is a flexible airtight bellows. **E** is the grounding contact for the sample (this contact is insulated from all other components). **F** is the probe tip. **G** is the fused silica hemispherical prism forming the substrate of our sample. **H** is a high-vacuum flange. **I** is the STM housing. **J** is the thin silver film deposited directly on the hemispherical prism, and **K** is a viton 0-ring for sealing the chamber. For simplicity, all electrical connections have been omitted.

dielectric medium for our SPP experiments.

One last component of our STM that deserves some attention is the STM probe tip. A large amount of literature has been published on the fabrication of probe tips. Reference [28] lists of over 80 papers detailing the art of probe tip fabrication by various means. In our lab, we have the capability of producing probe tips made from tungsten, platinum,silverand gold. We have experimented with each of these tips and found that tungsten proved to be the easiest to use and produced the best STM scan results. Tungsten tips also make good SPP scatterers, thus, we ended up relying on tungsten tips exclusively for use in our experiments.

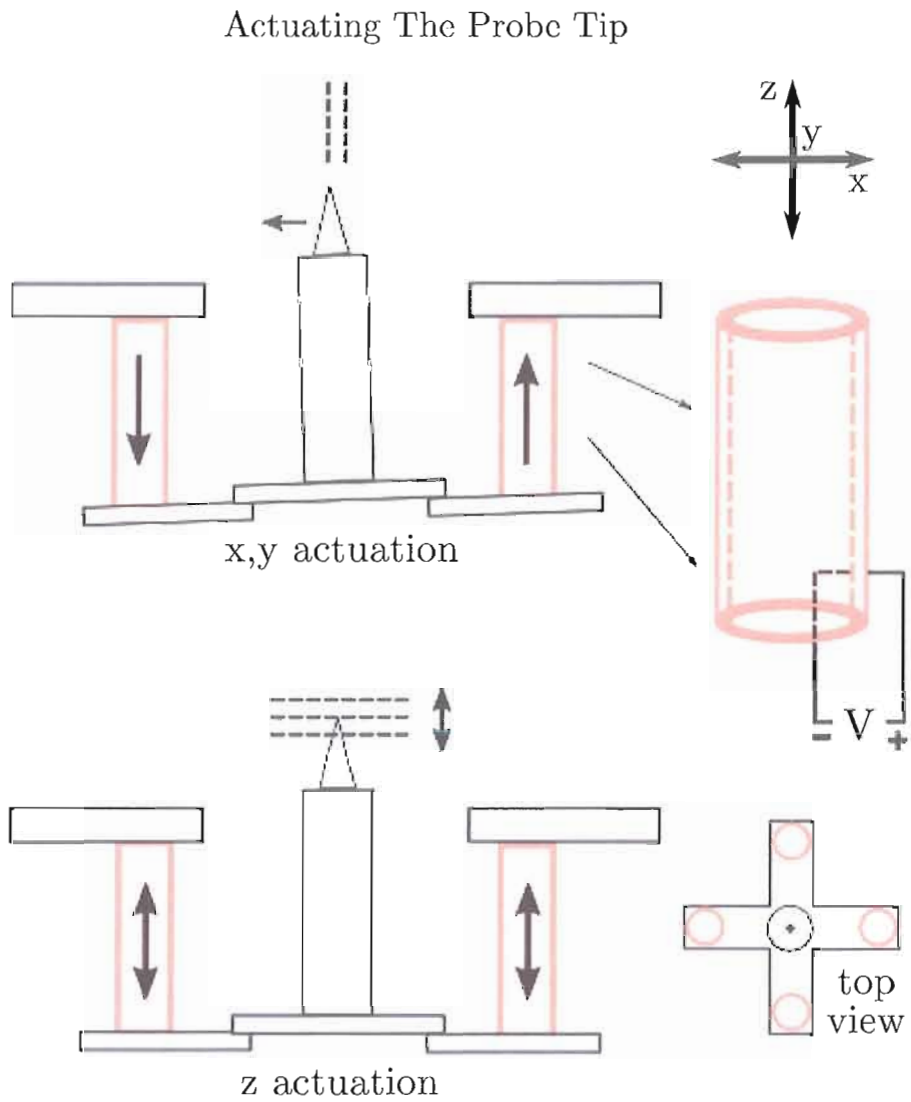

Figure 11: Actuating the probe tip. The tubes opposite one another work together to move the tip. As one tube expands, it's counterpart contracts, causing the central post to rock in a plane. For small displacements this translates into lateral movement of the tip. Moving the tip towards (or away) from the surface requires an identical contraction (or extension) from all four of the piezoelectric tubes. The top view shows the four quadrant geometry of the rocker with the probe tip in the center and the piezoelectric tubes at the four quadrants. Also shown on the right is a schematic for applying the voltage. Electrodes are soldered to nickel plating on the inside and the outside of the piezoelectric tube walls. A tube contracts when a voltage is applied across the walls of the tube with the polarity shown above. In operation, the quiescent voltage across the tube walls is set to about 80 volts. Contraction and expansion of the tubes is obtained by increasing or lowering the voltage respectively.

The best tungsten tips possessed good geometric characteristics and are sharp having tip radii of a few tens of nm. By far the most reliable way to meet these requirements is to fabricate the tips using an electrochemical etching process. Figure 12 illustrates our method for electrochemically etching tungsten rods.

In the etching process a 20 mil diameter tungsten rod is partially submerged in a 1.4 N solution of sodium hydroxide (NaOH). The rod acts as the cathode for the electrochemical process. It is this rod that is etched down to form the probe tip. The anode electrode consists of a submerged tungsten wire loop encircling the cathode. The designation of anode and cathode is entirely determined by the direction of current flow, and hence, the polarity of the applied voltage. This is important because, only the cathode electrode is etched in the process. A constant current of 124 ma is passed through the solution toenact the etching process. The etching of the tungsten occurs in the region of the meniscus formed where the tungsten rod enters the NaOH solution. After a time period of around seven minutes, the reduction of the tungsten rod becomes so great, that the lower section will pull free from the remaining upper section under the force of its own weight. Having broken free from the electrode, etching of the lower section ceases and it remains extremely sharp. To prevent damage to the tip, a holder is placed on the bottom of the container to safely catch the falling tip. The sharp end of the upper section will continue toetch away until it looses contact with the solution or until the current is stopped. This results in a tip that is far less sharp yet still retains a nice geometry. We retain the lower section for use in the STM. The upper section isusually discarded, but may be retained when a blunt, well formed tip is needed.

Electrochemical Etching of The Tungsten STM Probe Tip

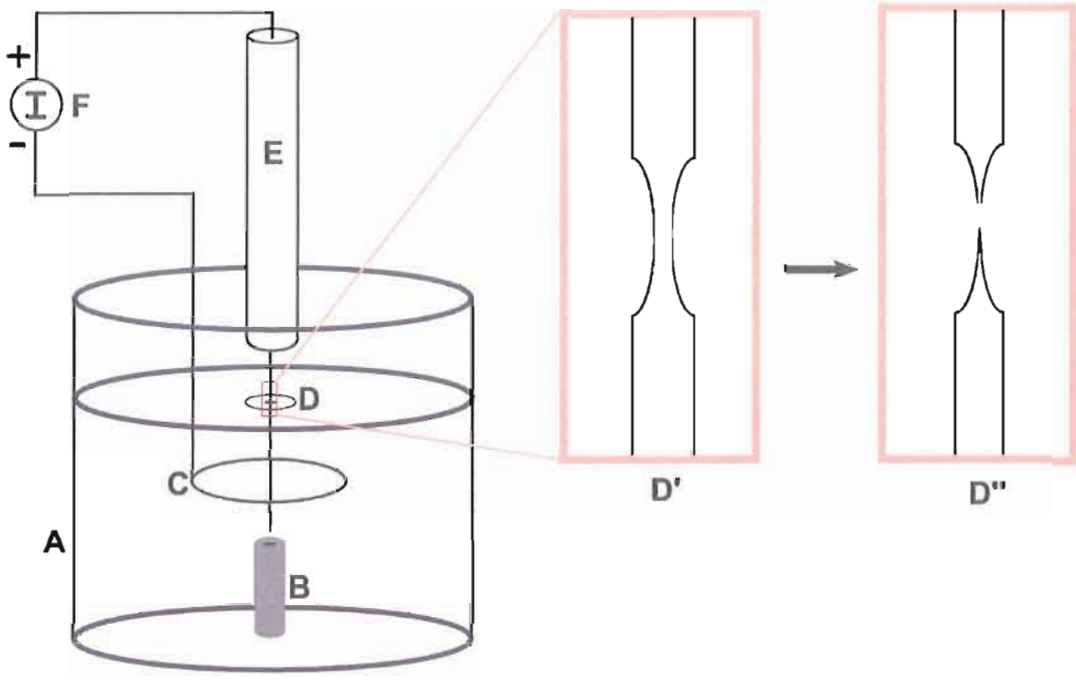

Figure 12: Electrochemical etching of the tungsten STM probe tip. **A** is a beaker containing a 1.4N NaOH solution, **B** is a holder for catching the finished etched tip when it breaks free from the tungsten rod electrode, **C** is the loop electrode (anode) that encircles the tungsten rod, **D** shows the tungsten rod (cathode) and depicts the location where the etching process occurs, **D'** is a close-up representation of **D** showing the etching of the tungsten rod at the meniscus layer, **D"** shows a finished etched tip breaking free of the remaining tungsten rod, **E** is a holder for the tungsten rod, and **F** shows the current source and the correct polarity for etching the tungsten rod.

III.4. STM Calibration

Based on preliminary STM scans, it became apparent that increasing the overall scan range capabilities of the STM was necessary for better matching the range over which SPPs are generated on the silver surface. Increasing the maximum scan range was accomplished by replacing the set of resistors at the summing junction of the op-amps used to control the maximum scan range of the probe tip. After the modification was complete, the new scan range was calibrated by scanning a gold plated

diffraction grating consisting of 3600 rules per mm and using the resulting topography to determine the range of the scan. Figure 13 shows the topography image from which we deduced the new scan range of $2.21 \pm .06\ \mu m$ for the x and y axes.

While a direct measurement of the x and y scan range was made, knowledge of the tip position in the z direction was based on information supplied by the manufacturer of the piezoelectric tubes, the displacement, $\triangle L$ in the z direction is determined by $\triangle L = -6.055 \triangle V$ where the prefactor is in units of nm per volt at 293K, where $\triangle V$ is the corresponding change in the applied voltage across the walls of the tube.

III.5. Thin Film Vacuum Deposition

Our samples consist of a thin silver film deposited directly onto the flat surface of a one inch diameter fused silica hemisphere by the process of vacuum deposition. We experimented with evaporating the metal film onto disposable cover slips and bonding the slips to the bottom of the hemisphere with index matching fluid, but this produced sub-par results.

We begin preparing the samples by first thoroughly cleaning the hemispheres. The cleaning process may include the removal of old silver films. This is accomplished by dissolving the film in a solution of nitric acid followed by a light polishing of the surface with a soft polishing pad and a suspension of 0.05μm alumina cubic crystal. All hemispheres are rinsed with acetone followed by isopropyl alcohol and deionized water. A final cleaning of the flat surface is performed with methanol and lens paper using the drop and drag method.

Once cleaned, the hemispheres are loaded into the evaporation chamber, and the chamber is pumped down using a combination of a turbo pump and a mechanical backing pump until a pressure of about 1×10^{-6} Torr is reached. At this stage in the process, an electrical current is passed through a tungsten boat containing high

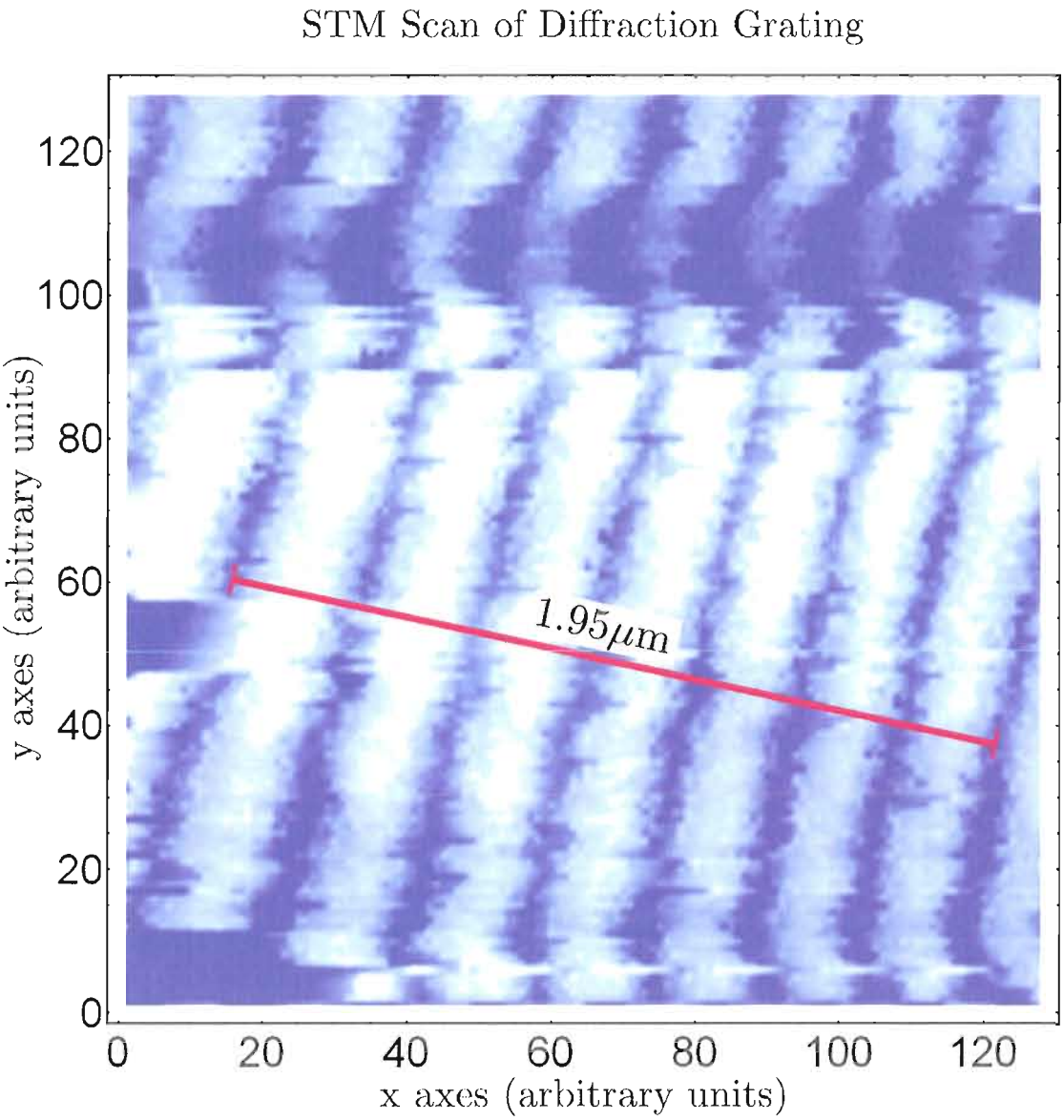

Figure 13: STM scan of diffraction grating. This topography scan of a gold plated diffraction grating (3600 rules per mm) was used for calibrating the scan range of the STM. Shown here is one representative measurement for the spacing of the rules. The breaks in the scan along the y coordinate are due to drifting of the sample in the z direction. The break indicates the location in the scan where a manual correction to the height of the tip was implemented to prevent a tip crash. From this data, our scan range was determined to be $2.21 \pm .06\ \mu m$. The numbers (tip steps) along each axis are the pixel numbers corresponding to a 128×128 resolution scan.

purity 69 grade silver shot located below a shutter. Above the shutter is a mask and above that, the flat side of the hemisphere. As the silver shot heats, it evaporates. The shutter is opened and the silver vapor travels unimpeded through the vacuum and condenses on the hemisphere surface exposed by the mask. The deposition rate and total thickness of the film is monitored by an Inficon XTM/2 Deposition Monitor with a crystal sensor positioned near the hemispherical substrate. Once the desired film thickness is achieved, the shutter is closed, halting the deposition process. The power down procedure is carried out, venting the chamber with dry nitrogen, and the sample is removed. The sample is maintained under vacuum or in an atmosphere of dry nitrogen to slow the process of contamination and corrosion. A useful sample lifetime of several weeks can be expected when these precautions are observed.

III.6. Full Experimental Apparatus

Figure 14 shows our experimental apparatus consisting of our hemispherical sample mounted upon our STM. The probe tip of the STM is positioned in such a way that it can interact with the evanescent field of the SPPs. Topographical surface scans of the silver surface can similarly be performed for characterization purposes.

Our primary optical source for exciting SPPs consists of a 5mw (max), 632.8 nm wavelength HeNe laser. We have also used argon-ion and ti-Sapphire lasers, but have found that much of the physics with which we are concerned can be conducted with the much friendlier HeNe laser.

There are two main sources of emitted light that are of interest to us. The first is the conical radiation emitted by the radiative decay from elastically scattered SPPs. The second, is the specularly reflected beam off the sample. We recorded the optical fields with a Sony XCD-X700 CCD camera having a 6.35mm (horizontal) $\times$ 4.7mm (vertical) CCD array with 1024 $\times$ 768 resolution and 8-bit monochrome depth. We recorded the optical fields in one of two ways. First, by allowing the light to fall directly onto the CCD array producing close-up and detailed images of the optical field. Alternatively, by projecting the light onto a diffuse screen and imaging the illuminated screen with a macro lens attached to the CCD camera. This method was good for enlarging the field of view for observing the entire cone of light at once.

Diagram of Our Experimental Apparatus

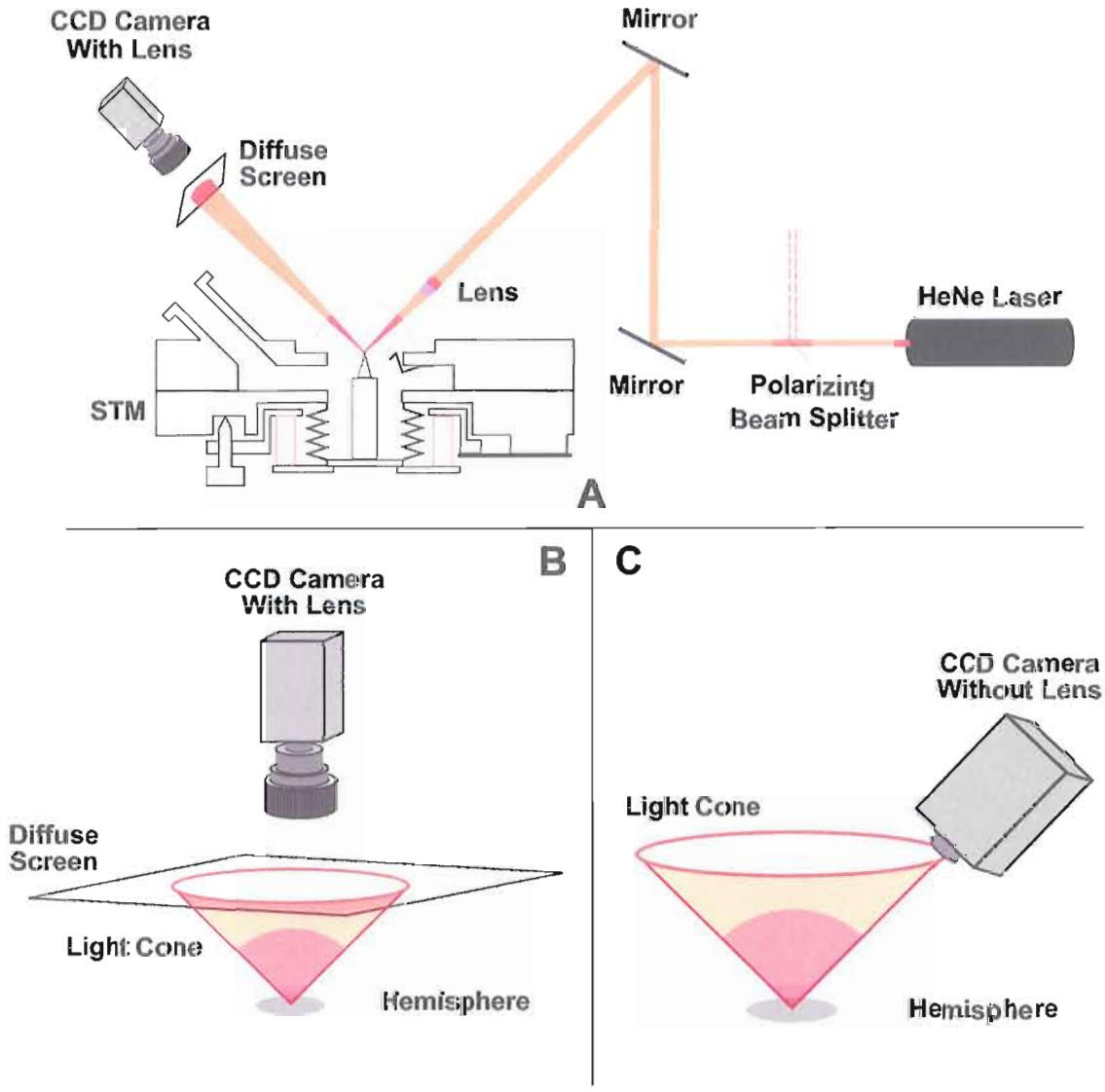

Figure 14: Diagram of our experimental apparatus. Diagram **A** shows the basic configuration of our experiment. The polarizing beam splitter ensures only P-polarized light reaches the sample for the excitation of SPPs. It also picks off a portion of the beam which can later be used as a reference field. The hollow cone of light emanating from the decay of elastically scattered SPPs is shown in diagrams **B** and **C** where the two different methods for detecting the light are illustrated. Diagram **B** shows the projection of the light onto a diffuse screen which is then imaged with a macro lens attached to the CCD camera. Diagram **C** shows the direct interception of the light onto the CCD array without the use of a lens.

CHAPTER IV

GENERATING IMAGES IN PHOTOMETRY SPACE

IV.1. Introduction

In our initial experiments we measured the optical radiation from the decay of SPPs as the STM tip is scanned within tunneling distance over the silver surface. The SPPs are generated by a strongly focused laser beam, thereby confining the excitation of SPPs to a small region on the surface which includes the scan region. This ensures a strong interaction between the STM tip and the generated SPPs. The emitted conical optical field (see figure 17) contains speckle resulting from random phase accumulation due to the multiple scattering of SPPs on the silver surface. The individual scattering centers are known to act as independent conical radiators [36] the positions of which add a random phase contribution to the speckle sum. Since the STM tip itself acts as an in-plane elastic scatterer (as well as a conical emitter) for the SPPs, moving the tip across the surface will alter the scattering scenario and modify the speckle in the conical field. Also apparent is the dependence of the overall intensity of the speckle on the distance of the tip from the surface.

In this chapter, we discuss several findings related to the changes in the speckle pattern under the influence of the moving tip. We will begin this chapter with a discussion of the characterization of the illuminated region on the silver surface. We will then discuss our results regarding apertureless Scanning Plasmon Optical Microscopy (SPOM) and conclude with a discussion of the stripe features that appear in our SPOM and photometry map images.

IV.2. Focused Incident Gaussian Beam

Throughout our experiments, we were particularly interested in the effects of the probe tip on the behavior of the SPPs. To maximize the effect of the tip, it was necessary to have the tip interact with as many of the available SPPs as possible. This was accomplished by restricting the excitation of the SPPs to within a small area on the silver surface centered about the tip by using a tightly focused incident beam. Once SPPs are excited, they will propagate forward, possibly out of the illuminated area. Since no physical surface is perfectly smooth, SPP scattering from adsorbed impurities, surface irregularities and other defects will cause SPPs to diffusely migrate away. Measuring SPP diffusion is one viable way of studying metallic film roughness [52, 53].

Knowing the characteristics of the incident Gaussian beam at the silver surface allows us to determine the excitation region of the SPP for calculation and simulation purposes. This was best accomplished by using ABCD transmission matrix formalism [37] for treating the Gaussian beam from our HeNe laser traversing through our optical system.

To begin, we state the complex amplitude for a general Gaussian beam traveling in the z direction with lateral profile in the x, y plane as given by

$$E(r,z,t) = E_0 \frac{w_0}{W(z)} \exp\left[-\frac{r^2}{W^2(z)}\right] \exp\left[ikz + ik\frac{r^2}{2R(z)} - i\xi(z) - i\omega t\right] \tag{35}$$

with

$$\begin{aligned} W(z) &= w_0\sqrt{1+\left(\tfrac{z}{z_0}\right)^2}, & \xi(z) &= \arctan\left(\tfrac{z}{z_0}\right) \\ R(z) &= z\left[1+\left(\tfrac{z_0}{z}\right)^2\right], & z_0 &= \tfrac{\pi w_0^2}{\lambda} \end{aligned} \tag{36}$$

Where w_0 is the beamwaist, i.e. the beam radius at its narrowest part. The size and location of the beamwaist is determined by the resonator of the laser and its location is defined to be $z = 0$. The Rayleigh distance is given by z_0 and provides, among other things, a measure of the depth of focus. $W(z)$ is the beamwidth radius, $R(z)$ is the radius of curvature of the wavefront, and $\xi(z)$ is the Gouy phase. The values of w_0 and $W(z)$ are determined when the beam's transverse intensity falls to $\frac{1}{e^2}$ of its on axis value.

Gaussian beams have the special property of retaining their Gaussian nature as they propagate through an optical system consisting of lenses and mirrors. Only their wavefronts and beam widths are modified. For example, a Gaussian beam transmitted through a positive focusing lens will remain Gaussian, but its wavefront will obtain a negative radius of curvature resulting in the beam converging to a focus. The ability to use ABCD transfer matrix formalism for determining the values of $W(z)$ and $R(z)$ though an optical system is one of the many beneficial properties of Gaussian beams. The construction of the transfer matrix for a specific optical system is exactly the same as that for ray tracing, only its implementation for Gaussian beams is different. The transfer matrix given by

$$M_T = \begin{bmatrix} A & B \\ C & D \end{bmatrix} \tag{37}$$

allows us to calculate the final values of R and W from their initial values using

$$q_f = \frac{Aq_i + B}{Cq_i + D} \tag{38}$$

$$q = \frac{\pi^2 R W^4}{\pi^2 W^4 + R^2\lambda^2} + i\frac{\pi R^2 W^2 \lambda}{\pi^2 W^4 + R^2\lambda^2} \tag{39}$$

The quantities q_f and q_i of equation 38 are respectively the final and initial value of q, where q provides the expression for the beam width radius, W, and the radius of curvature, R as given in equation 39.

Our optical system consists of a lens with a focal length of 20mm followed by a translation through air to the curved surface of the hemisphere and a final translation through the glass of the hemisphere to the silver film. The initial values for the beam width and the radius of curvature of the incident Gaussian beam have the approximate values of $W_i \approx 1.6$ mm (measured), and $R_i \approx 1.5$ m (calculated). With these initial values, the spot size diameter at the metal surface is calculated to be 4.2 μm with a wavefront radius just inside of the focus of -2.9 mm which indicates a nearly flat yet slightly converging beam. Since the wavefronts remain nearly flat over the range in which the beam illuminates the surface, we can safely approximate the electric field at the silver film with

$$E(x,y) = E_0 \exp\left[\frac{x^2}{W_x^2} + \frac{y^2}{W^2}\right] \exp\left[ik_{xi}x\right]. \tag{40}$$

Where $W_x = \frac{W}{\cos\theta_i}$ is the major diameter of the elliptical spot on the surface for incident angle, θ_i, and $k_{xi} = k_0\sqrt{\epsilon_1}\sin\theta_i$ which describes the progression of the phase across the surface due to the tilt of the beam. W is the beamwidth at the focus, k_0 is the wave vector in air/vacuum and ϵ_1 is the dielectric constant of the fused silica

hemisphere.

Figure 15 shows the plot of equation 40 for the beam on the silver surface. The modulation was added to reveal the advancement of the phase across the surface, each peak in the modulation corresponds to a 2π phase advance in the $+x$ direction. Since SPP resonance occurs when the in-plane momentum of the optical field coincides with the momentum of the SPP ($k_{xi} = k_{sp}$), the SPP field stays in phase with the launching field all along the length of the illuminated region.

An interesting result that occurs in the reflection profile of a tightly focused beam that does not occur for broadly focused beams incident at the SPP resonance angle is the appearance of interference fringes in the specular reflection. Ignoring for the moment the y axis profile of equation 40 we can decompose the incident beam profile into its Fourier planewave components given by

$$G(k_x) = \frac{w_o}{\sqrt{2}} e^{-\frac{w_0}{4}(k_x - k_{sp})^2} \tag{41}$$

where

$$G(k_x) = \frac{1}{\sqrt{2\pi}} \int_{-\infty}^{\infty} g(x) e^{-ik_x x} dx \tag{42}$$

Here, $g(x) = e^{-(\frac{x}{w_0})^2 + ik_{sp}x}$ is the Gaussian beam profile on the glass-silver surface at the SPP resonant angle i.e. $k_{sp} = k_0\sqrt{\epsilon_1}\sin\theta_{sp}$, and $w_0 = \frac{W}{\cos\theta_{sp}}$. The amplitude reflection profile at any distance z from the glass prism-silver (first surface) interface is given by the inverse Fourier transform

$$ref_{123}(x,z) = \frac{1}{\sqrt{2\pi}} \int_{-\infty}^{\infty} G(k_x) r_{123} \exp(i\sqrt{\epsilon_1 k_0^2 - k_x^2}\, z) e^{ik_x x} dk_x. \tag{43}$$

Where r_{123} is the plane wave Fresnel equation 32 for a three layer system. Alternatively, we can calculate the contribution to the total reflection from each interface separately by replacing r_{123} in equation 43 with r_{12} for reflection from the glass prism-silver (first surface) and $(r_{123} - r_{12})$ for the silver-vacuum (second surface) interface.

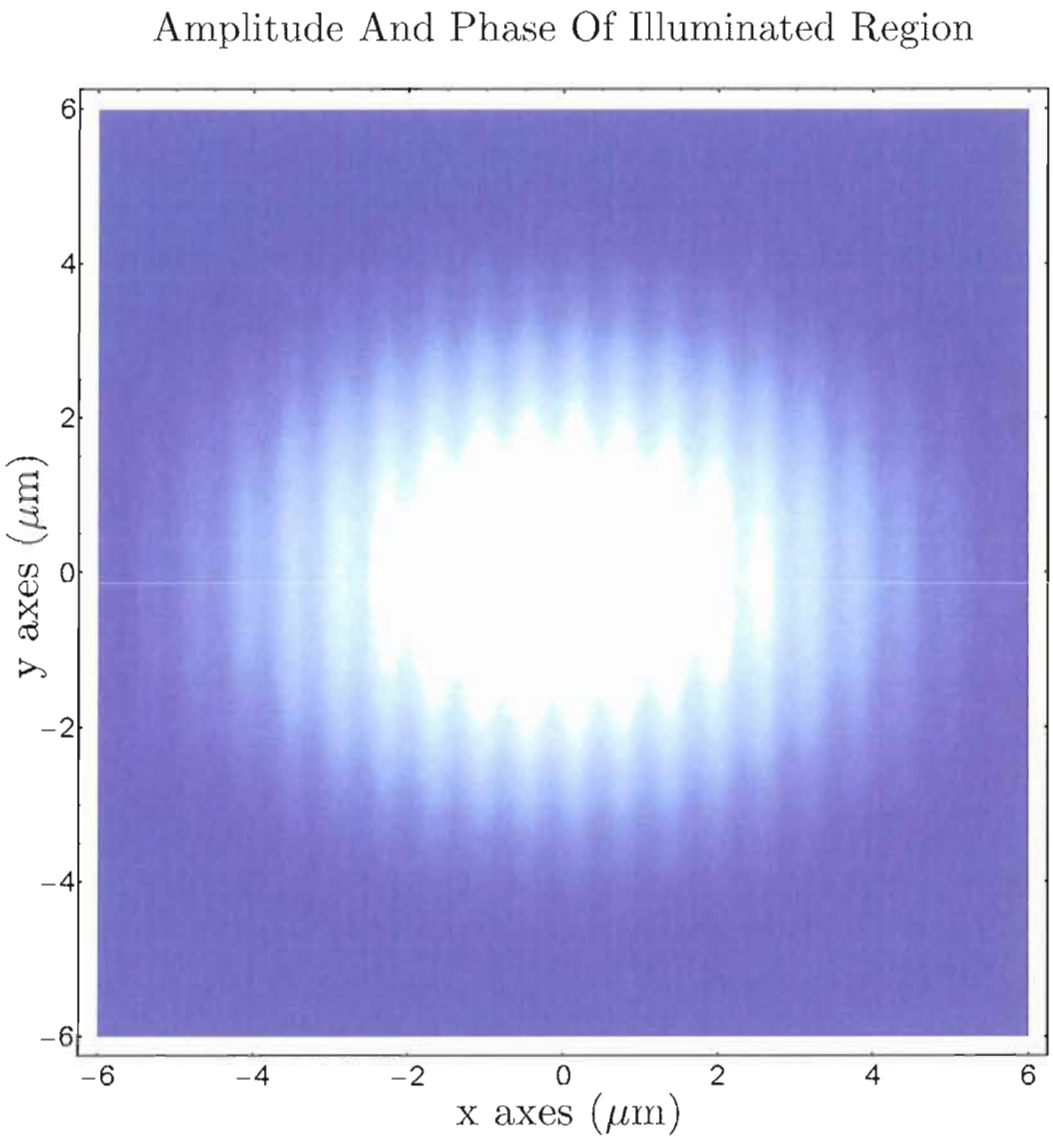

Figure 15: Amplitude and phase of illuminated region. The amplitude of the illuminated spot as described by equation 40 incident from the -x direction. The modulation was added to illustrate the phase advance across the surface. Each peak in the modulation corresponds to a 2π advance in phase.

Here, r_{12} is given by equation 7. Figure 16 shows the amplitude reflection for each layer separately along with the total reflection intensity.

The reflection of the incident Gaussian beam is found to retain its Gaussian profile upon reflection from the first surface as it propagates and diffracts away from the interface. The reflection from the second interface shows evidence of the SPP propagation along the silver-vacuum interface. As this field propagates and diffracts, wiggles in its profile appear, these same wiggles interfere with the Gaussian profile from the first surface creating a total reflected intensity with an interference maxima that may exceed unity. Upon reaching the far-field, the second surface reflection approximates a Lorentzian which interferes destructively with the Gaussian creating a Gaussian with a central notch in its reflected intensity.

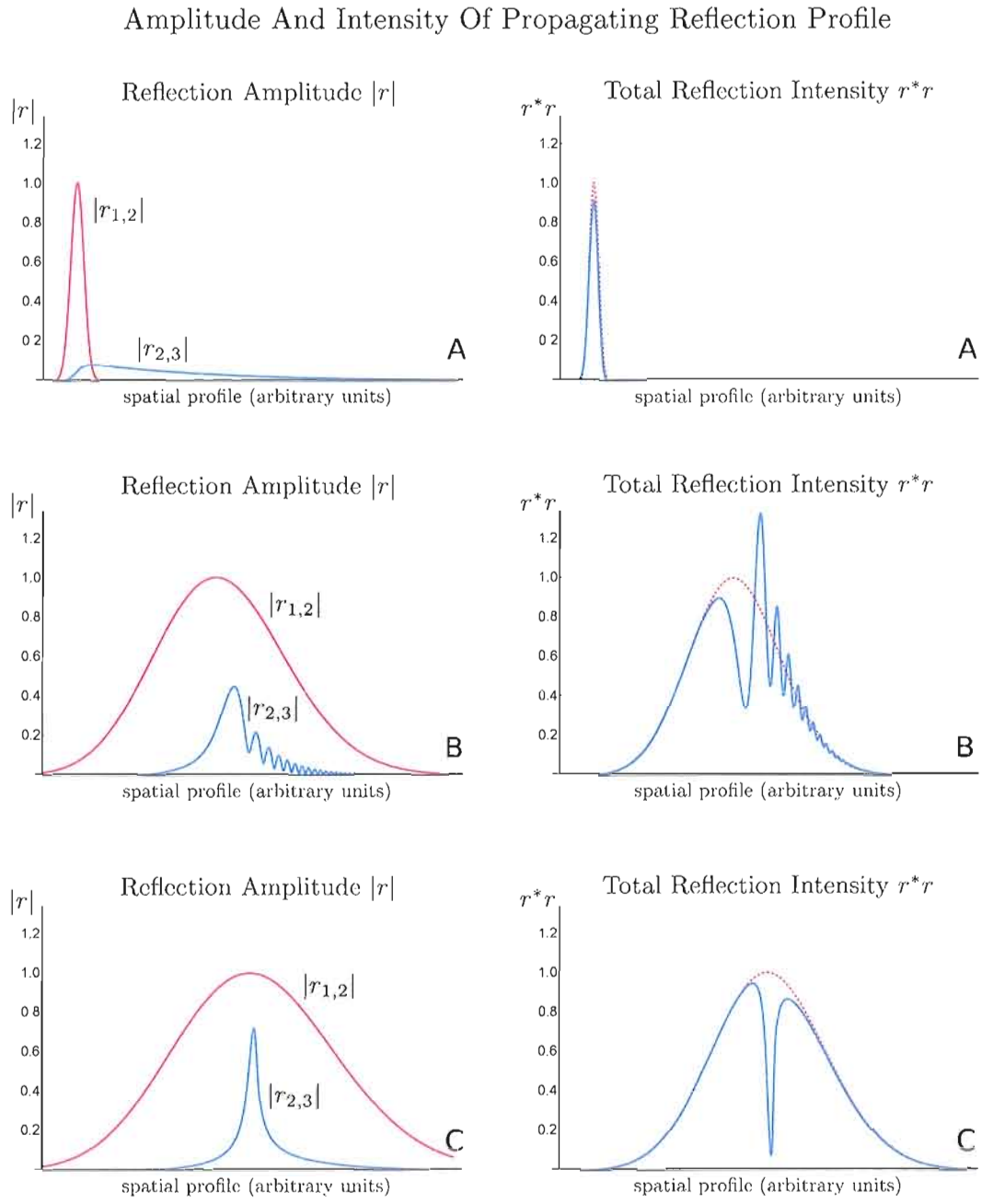

Figure 16: Amplitude and intensity of propagating reflection profile. The images on the left show the amplitude reflection from the first surface and second surface. The images on the right show the corresponding total reflected intensity from the three layer system. The reflection intensity profile of a Gaussian is shown for comparison. Images A correspond to the fields right as they leave the surface ($z = 0$). Images B shows the field profiles as they diffract out to an intermediate region between the near-field and the far-field. Images C shows the final profiles in the far-field. From this point on, the reflected beam continues to expand while maintaining this profile.

Depiction Of Common Terms Used In This Thesis

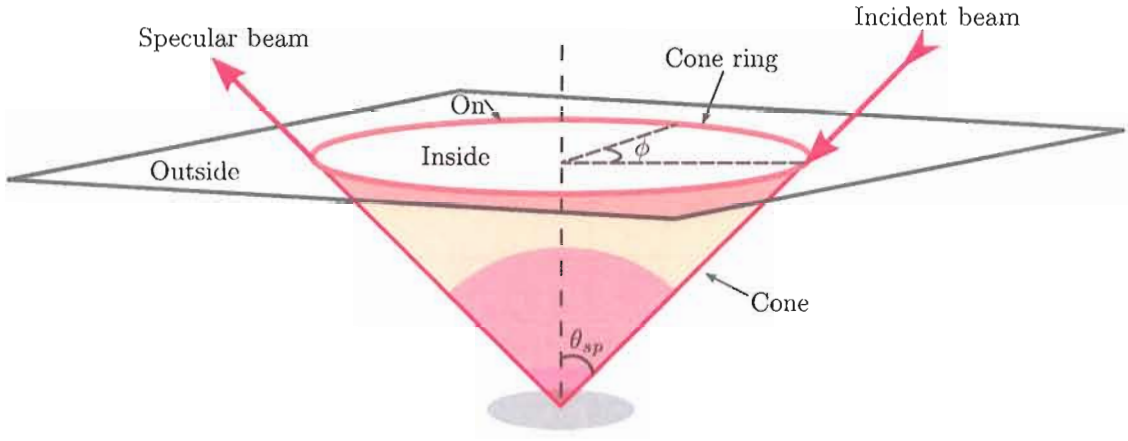

Figure 17: Depiction of common terms used in this thesis. These terms are for referring to features of the incident, reflected and re-radiated cone of light.

IV.3. Description of Terms

For clarity, a few terms are defined regarding the features of SPP resonance and the radiated cone of light. Figure 17 shows the incident beam used for exciting SPP as well as the resultant specularly reflected beam. An SPP undergoing random scattering along the silver-vacuum interface may eventually decay into a photon and exit through the hemisphere along the SP resonant angle θ_{sp} as required by the condition set by the dispersion relation. This produces a hollow cone of radiated light consisting of speckle. The projection of the radiated cone onto a screen produces the cone ring. Any location on the ring is described by the azimuthal angle ϕ as measured from the location of the incident beam in the counter clockwise direction.

IV.4. Scanning Plasmon Optical Microscopy

Scanning Plasmon Optical Microscopy (SPOM), like other near-field optical microscopy techniques, is capable of surpassing the Abbe diffraction limit that prevents conventional optical microscopes from resolving sub-wavelength features. Pohl [38]

compared this phenomenon to a similar situation involving the familiar stethoscope used by medical practitioners. Pohl describes how the position of a patient's heart can be localized to within a few centimeters simply by moving the stethoscope over the patient's chest and listening for the heart beat. He points out that a heart rate of between 30 and 100Hz corresponds to a wavelength of nearly 100m, and therefore, the stethoscope has a resolving power of nearly $\frac{\lambda}{1000}$. The high resolving power of the stethoscope is not limited by the wavelength of the heart beat, but rather, by the diameter of the stethoscope head and its distance from the heart.

Similar behavior is seen for optical [35, 40] and SPP fields for aperture and apertureless probes [39, 41]. Aperture probes, which include metal coated sharpened optical fibers and metal coated cut quartz rods, sample the evanescent field, converting it to a propagating field through its core, and directing it to a detector. While the aperture of this type of probe can be smaller than the wavelength of the light being sampled, they are not as sharp as apertureless probes such as the etched all metal tips used in scanning microscopy. Since apertureless probes can be made sharper, a few tens of nm at their point, they tend to provide better spatial resolution. The apertureless probe is often modeled as a scatterer in which the evanescent field creates an induced dipole at the tip. SPP near-field microscopy occurs quite naturally in our experimental arrangement and we point out several issues regarding the resulting optical signal.

Apertureless near field optical microscopes are typically operated in conjunction with other surface scans such as STM and Atomic Force Microscopy (AFM). The STM and AFM provides the necessary tip to surface feedback for tracking along the surface. Previous investigators have created SPOM images by recording the total intensity of the specular beam [39] and alternately, the total combined intensity in the SPP cone [42, 43]. Optical images produced from the intensity fluctuations in

the cone tend to have more clarity due to the larger signal to noise ratio as opposed to images generated from the specular beam. Recording intensity fluctuations in the specular beam requires measuring small intensity variations within the very bright reflected beam. Attempts have been made by others to obtain scanning plasmon optical images without the aid of a feedback loop (force free interaction), however, this method tends to produce rather poor SPOM images [43]. For this reason, SPOM images are best used for providing complimentary information in conjunction with auxiliary scanning methods.

The interaction of a tungsten STM tip with the evanescent field of the SPPs on a metal surface is fairly difficult to model [44]. Most attempts require the use of Finite Difference Time Domain (FTDT) numerical calculations. However, certain properties of the interaction can be easily measured. Figure 18 shows the response of the average cone ring intensity to the separation distance of the probe tip as it withdraws from tunneling contact with the surface. A separation distance of zero indicates tunneling distance. It can be seen that from tunnel contact to a distance of about 15 nm, the average cone ring intensity actually increases. As the tip withdraws further, the ring intensity begins to fall. As a result of this behavior, it is possible for the SPOM image to record a depression where a peak on the surface resides (see figures 19 and 20.) This is not, however, the only way in which an inversion of the intensity within the SPOM image can occur. Figure 21 for instance shows a SPOM image generated at different locations along the cone ring revealing inversions due to interference from SPP single scattering off of the probe tip.

IV.5. Single Scattering and Primary Stripes

The SPOM image is just one manifestation of what we refer to as the photometry map. That is, the optical image map created by observing a single location in the

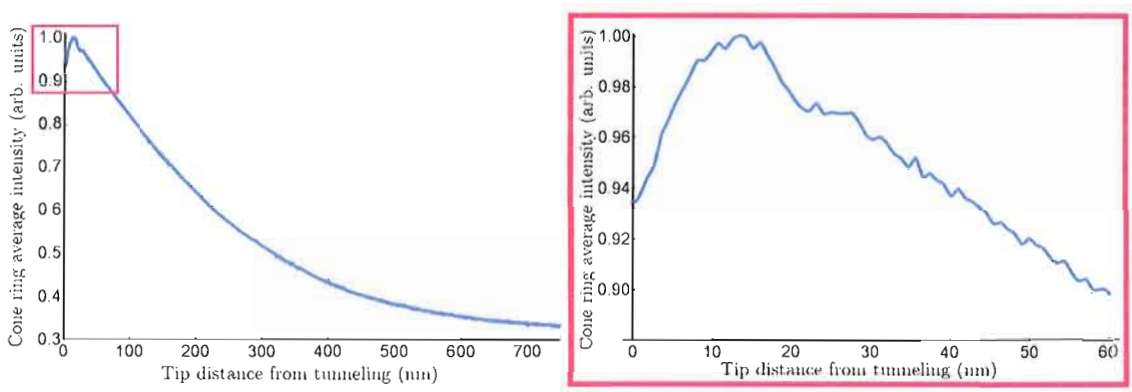

Figure 18: Average cone ring intensity vs. probe tip distance from the surface. As the tungsten STM tip is pulled away from a 40 nm thick silver film surface, the intensity is seen to rise until a separation distance of about 15nm is reached, in which case, the intensity begins to fall. The image on the right shows a close up view of the upper region enclosed on the left.

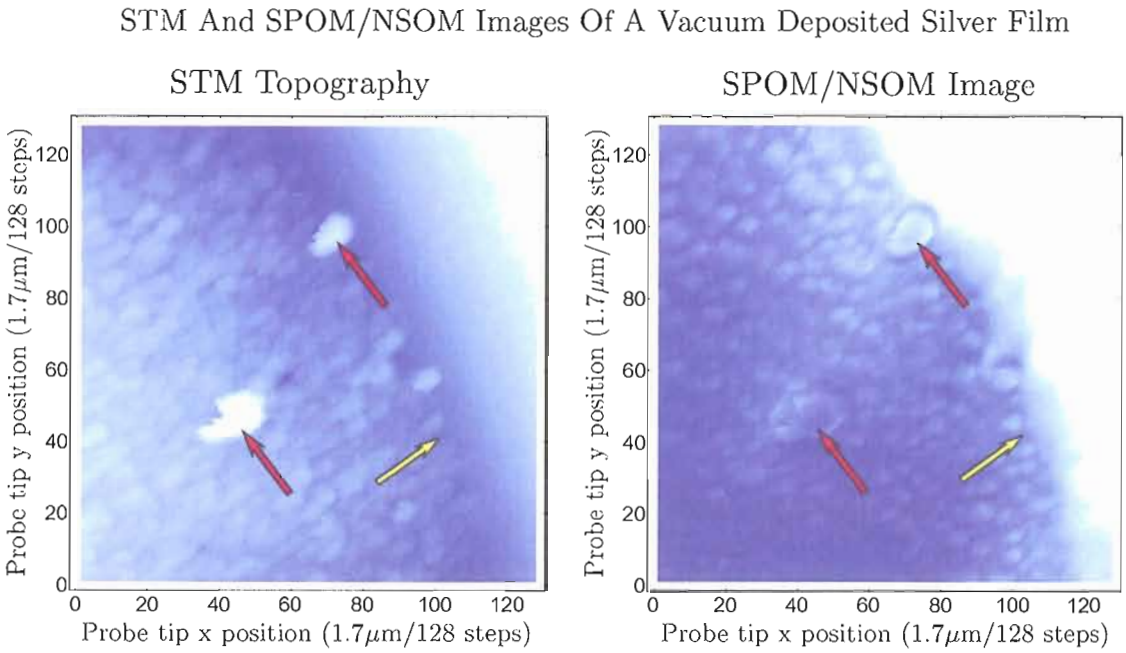

Figure 19: STM and SPOM/NSOM images of a vacuum deposited silver film. Crystal grains as revealed in an STM topography (left) and the corresponding SPOM image (right) obtained by averaging the intensity fluctuations at 10 chosen locations on the cone ring. Notice how the two prominent peaks (red arrows) in the STM topography image appear with central depressions in the SPOM image. The yellow arrow shows where the STM probe tip looses tunneling contact with the silver surface in both the topography and the SPOM image.

Isolation Of Large Topography Feature

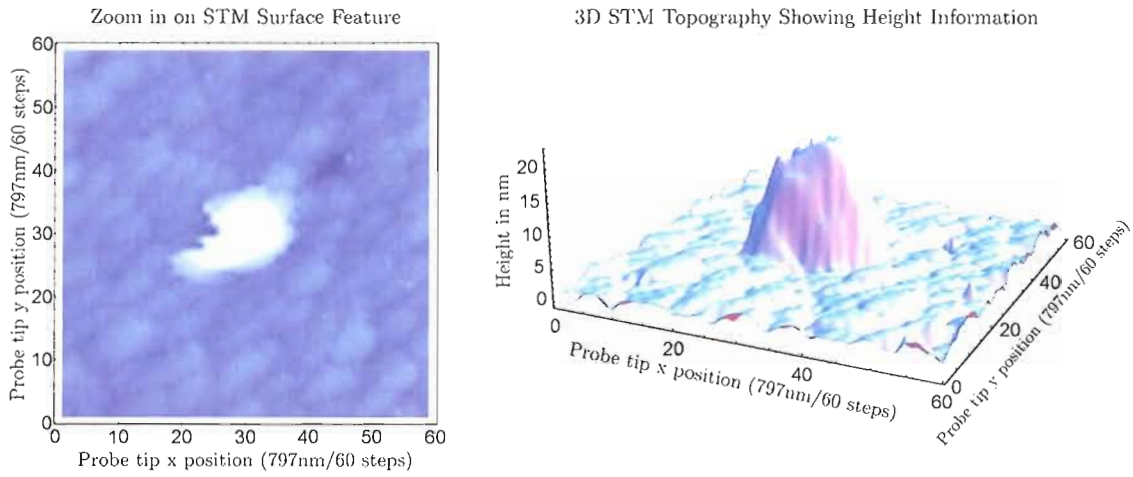

Figure 20: Isolation of large topography feature. The feature shown in Figure 19 is isolated and shown in a three dimensional representation to better gauge its height. The height is greater than 20nm making it a good candidate for the SPOM/NSOM image intensity inversion.

radiated field and recording the intensity at that location for each position of the probe tip either in or out of tunneling distance with the surface. In the previous section, we pointed out the existence of stripes that appear in the SPOM images. We will refer to these stripes as the primary stripe for reasons that will soon become apparent. These primary stripes also appear in the optical images from raster scans where the tip is pulled back beyond tunneling distance. As expected, the intensity of the primary stripes in the photometry images decrease according to the exponential fall off length of the evanescent SPP field in the direction away from the surface. What follows is a model for understanding the primary stripes.

Simply put, the primary stripes are the result of the SPPs undergoing single scattering off of the tip. Figure 22 shows the geometrical construction used to derive the origin of the primary stripes. Notice, that there are two contributions to the phase responsible for the periodic structure of the primary stripes. The first is the phase of the excited SPP field that is locally sampled by the tip i.e. $\varphi_{tip} = k_{sp} x_{tip}$.

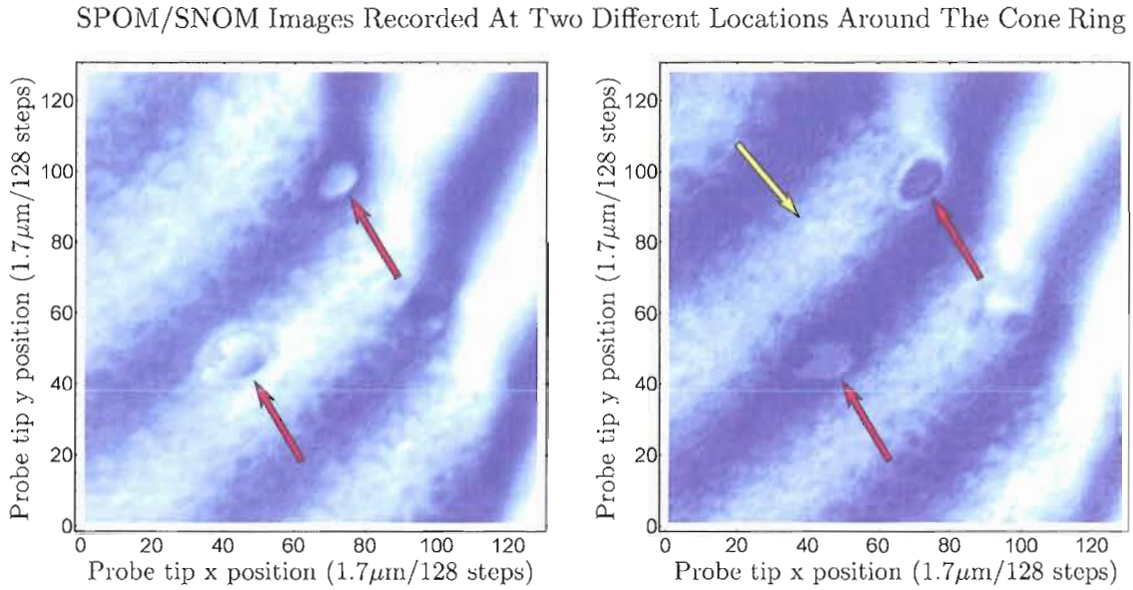

Figure 21: SPOM/NSOM images recorded at two different locations around the cone ring. One of the most noticeable features of this image are the stripes (as pointed out by the yellow arrow) across the image. These stripes are referred to as primary stripes and they are a feature of the optical signal at individual locations on the cone ring. Depending on the phase of the primary stripes, an inversion of the intensity of the SPOM image can occur (see red arrow). The effects of the primary stripes on the SPOM image can be reduced, but not entirely eliminated, by summing over all of the locations on the cone ring.

The second contribution comes from the phase accrued by the radiated field due to the path distance from the tip to a specific location on the cone ring i.e. $\varphi_{L_{tip}} = k_0 L_{tip}$ where k_0 is the wave number of the light in the fused silica hemisphere. The distance from the surface location of the tip to any point in the cone is given by $L_{tip} = \sqrt{[\rho \sin(\theta_{sp}) \cos(\phi) + x_{tip}]^2 + [\rho \sin(\theta_{sp}) \sin(\phi) + y_{tip}]^2 + [\rho \cos(\theta_{sp})]^2}$. Where ρ is the radial distance from the origin out to a location in the cone ring, θ_{sp} is the resonant angle for optically exciting SPPs, (x_{tip}, y_{tip}) is the location of the tip on the surface, and ϕ is the azimuthal angle measured from the $-x$ axes indicating the location in the cone ring. Since the phase of a photon cycles through many orders of 2π on its journey from the tip to a location on the cone, it is useful to subtract off a characteristic length and work instead with the change in photon path distance as opposed to the path distance itself. A useful distance to use is the distance from the origin on the surface to the location of interest in the cone i.e. $L_{origin} = \rho$. The resultant change in the path distance is given by $\triangle L = (L_{tip} - L_{origin})$ with the change in phase given by $\triangle\varphi = k_0 \triangle L$. To further simplify the expression, we can take advantage of the fact that we are looking at a position on the cone in the far-field ($\rho >> \lambda$), this allows us to simplify the change in the difference of the propagation length to $\triangle L = \lim_{\rho \to \infty} (L_{tip} - L_{origin}) = [x_{tip} \cos(\phi) + y_{tip} \sin(\phi)] \sin(\theta_{sp})$. In order for the stripes to appear in the photometry image, the radiated field from surface location at the tip must interfere with some coherent background field. The primary source for this background field are SPP scattering events on the surface that do not include the tip and which ultimately radiate into the cone along the observation direction. The expression for the expected intensity at a specific azimuthal location on the cone ring due to single scattering from the STM tip is given by

$$I\left(\phi; x_{tip}, y_{tip}\right) = \left| a \exp\left[i\Phi\right] + \tilde{b} \exp\left[ik_{sp}x_{tip} + ik_0 \sin\left[\theta_{sp}\right]\left(x_{tip}\cos\left[\phi\right] + y_{tip}\sin\left[\phi\right]\right)\right]\right|^2 \tag{44}$$

which simplifies to

$$I\left(\phi; x_{tip}, y_{tip}\right) \propto 1 + \cos\left[k_{sp}x_{tip} + k_0 \sin\left[\theta_{sp}\right]\left(x_{tip}\cos\left[\phi\right] + y_{tip}\sin\left[\phi\right]\right) + \phi_a\right] \tag{45}$$

Where a is the amplitude of the background field, $\tilde{b}$ is the complex amplitude of the singly scattered beam, Φ is the overall phase of the background field, and ϕ_a is the phase that arises when simplifying equation 44 to equation 45. In practice we treat ϕ_a as an arbitrary constant to be fitted if necessary.

From equation 45 we can determine the expected wavelength for the stripes as a function of the azimuthal angle around the cone ring as given by

$$\lambda_{stripe}\left(\phi\right) = \frac{2\pi}{\sqrt{\left(k_{sp} + k_0 \sin\left[\theta_{sp}\right]\cos\left[\phi\right]\right)^2 + \left(k_0 \sin\left[\theta_{sp}\right]\sin\left[\phi\right]\right)^2}} \tag{46}$$

Testing the validity of equation 46 we compare it with the observed wavelength of the stripes obtained for each azimuthal position on the cone ring. Figure 23 details the method for determining the wavelength of the primary stripes found in the photometry images for a probe scan outside of tunneling distance and figure 25 shows the comparison of equation 46 to the wavelength of the primary stripes obtained from experiment.

The generated stripes provide a way to determine the relative phase of the speckle found in the cone ring by measuring the shift of the stripes for different locations on the cone. We can therefore use them to find locations of optical vortices in the speckle pattern of the cone ring by observing how the primary stripes in the photometry maps shift as we traverse a closed loop about some region (see chapter V). The stripes also provide a way of detecting other strongly propagating SPP fields on the sample

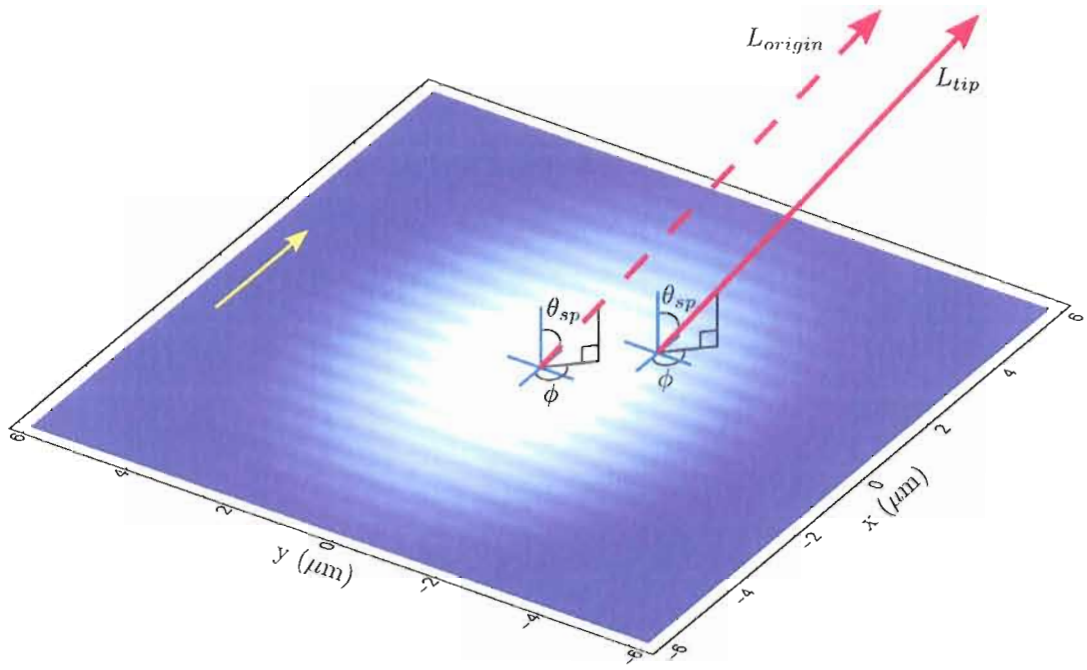

Figure 22: Surface phase and the origin of the primary stripes. The modulation of the illuminated region shows the advancement of phase due to the incident angle of the incoming beam as described in figure 15.The arrow on the far left (yellow) indicates the direction of the launched SPP propagation, and more importantly, the direction of the phase advance of the SPP field. The dashed red arrow (labeled L_{origin}) shows a representative path taken by a radiated photon leaving the surface from the origin. The scattering angle ϕ is measured counter clockwise from the $-x$ axes, and θ_{sp} is the SPP resonant angle. L_{origin} refers to the path length of the photon out to a specific point on the cone ring from the origin. Similarly L_{tip} refers to the path length to the same point on the cone ring originating from the location of the tip on the surface.

surface. In the next section, we discuss our search for coherent back scattered fields on the surface and propose a way of measuring these and other directional fields using the stripes.

IV.6. Coherent Back Scattering and Secondary Waves

After performing many scans, we noticed that other stripes (we will call these secondary stripes) would occasionally accompany the primary stripes in the photom-

Analyzing The Primary Stripes Using The Fourier Transform

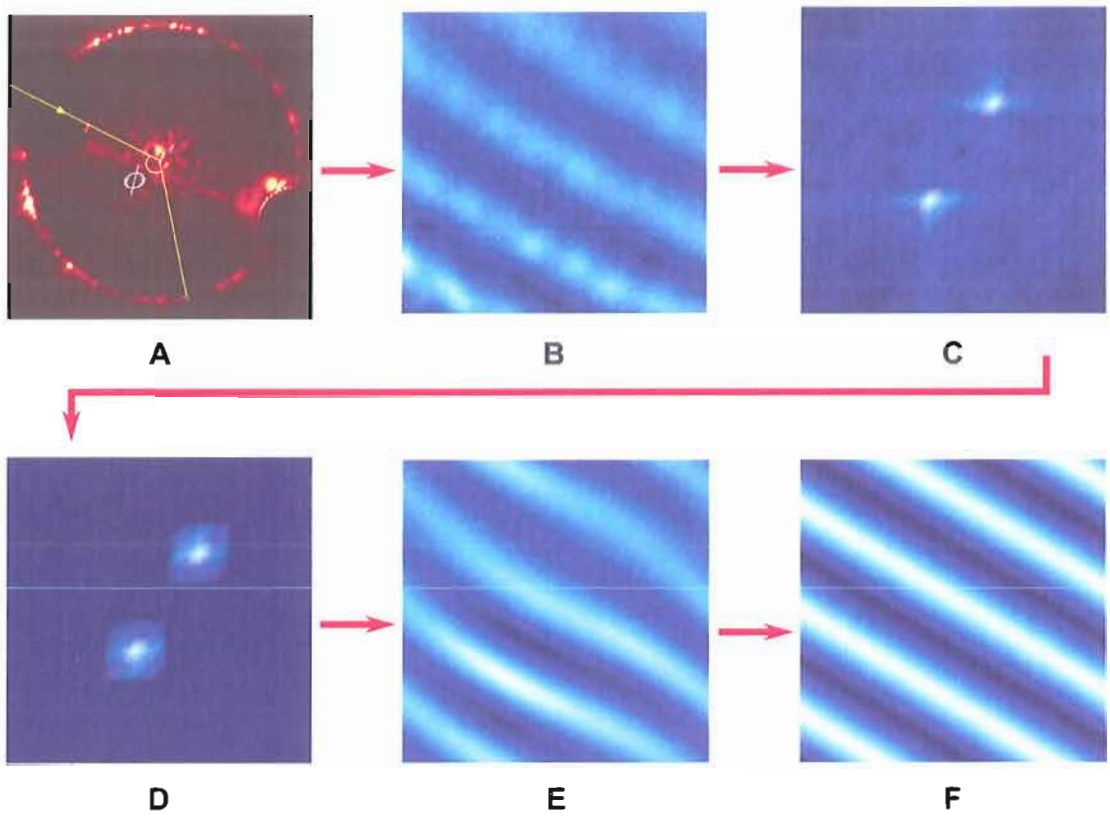

Figure 23: Analyzing the primary stripes using the Fourier transform. Image **A** shows the projection of the cone on a screen producing the cone ring. The location on the cone ring is specified by the azimuthal angle ϕ. By recording the intensity fluctuations at this location on the cone ring for each position of the scanned STM tip, a photometry map is constructed. Image **B** is one such photometry image showing the strong primary stripes that are the result of single scattering events off of the tip. Mathematica code was written to automatically calculate the k_x and k_y components of the stripe images. This calculation was accomplished by first calculating a Fast Fourier Transform (image **C**) of the stripe image (image **B**) which allowed us to pullout trial values for k_x and k_y to seed the fitting algorithm. Image **D** shows the main reciprocal components in Fourier space with the "noise" found in image **C** striped away. Image **E** shows the "noise free" Reverse FFT of transform **D** and image **F** shows the least squares fit of the stripe image found in **E**. The fitted stripes in image **F** can be compared with the original stripes in image **B** to see the close match.

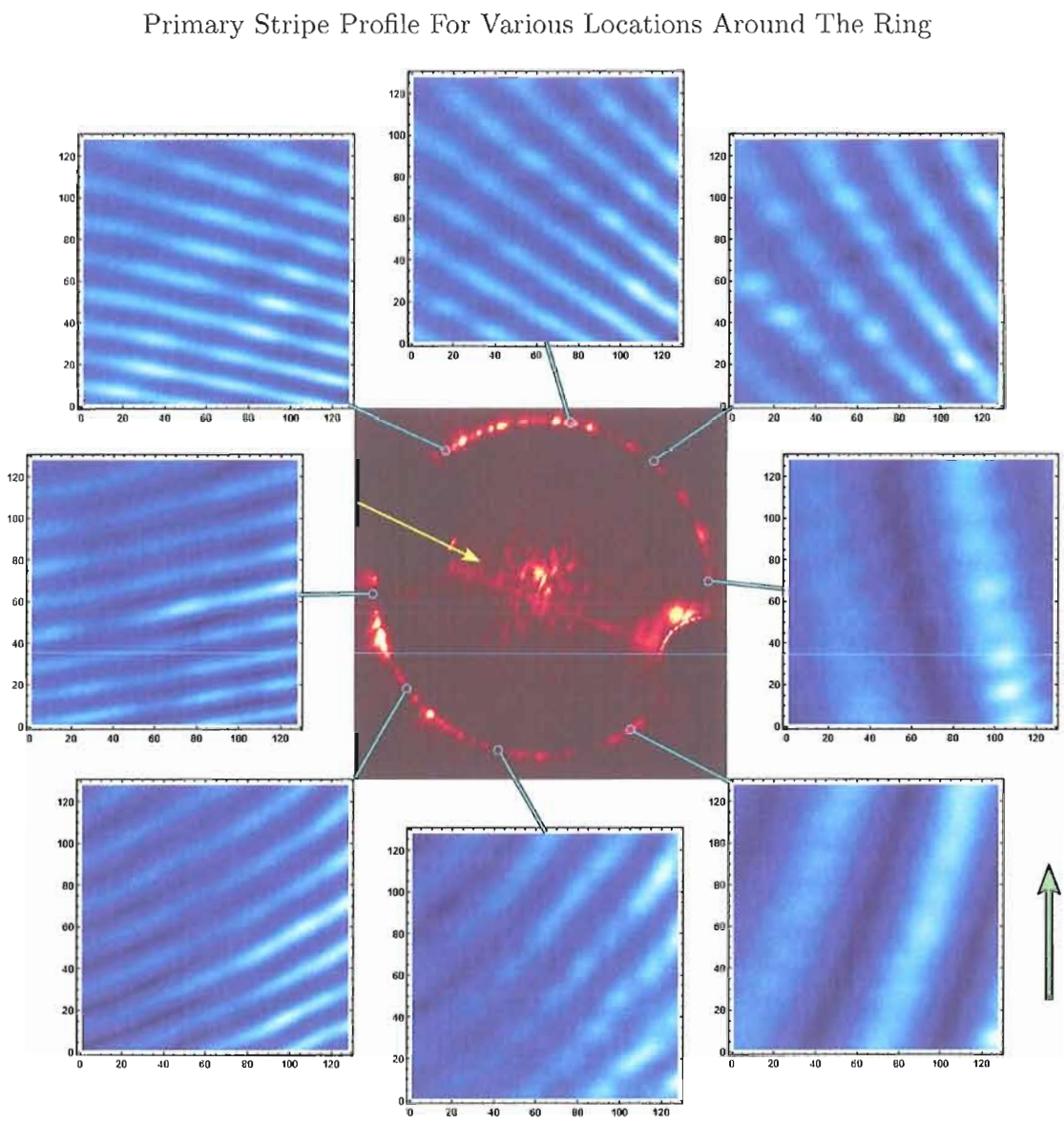

Figure 24: Primary stripe profile for various locations around the ring. These are examples of the primary stripes found in the photometry maps for different azimuthal locations around the cone ring. Notice the orientation and the spread of the primary stripes depending on the observation position. The direction of the incident beam is shown by the arrow (yellow) placed in the central cone ring image. This corresponds to the direction of the incident beam shown by the arrow (green) on the lower right hand side for each of the primary stripe photometry images. The orientation and spread of the stripes are predicted by equation 45.

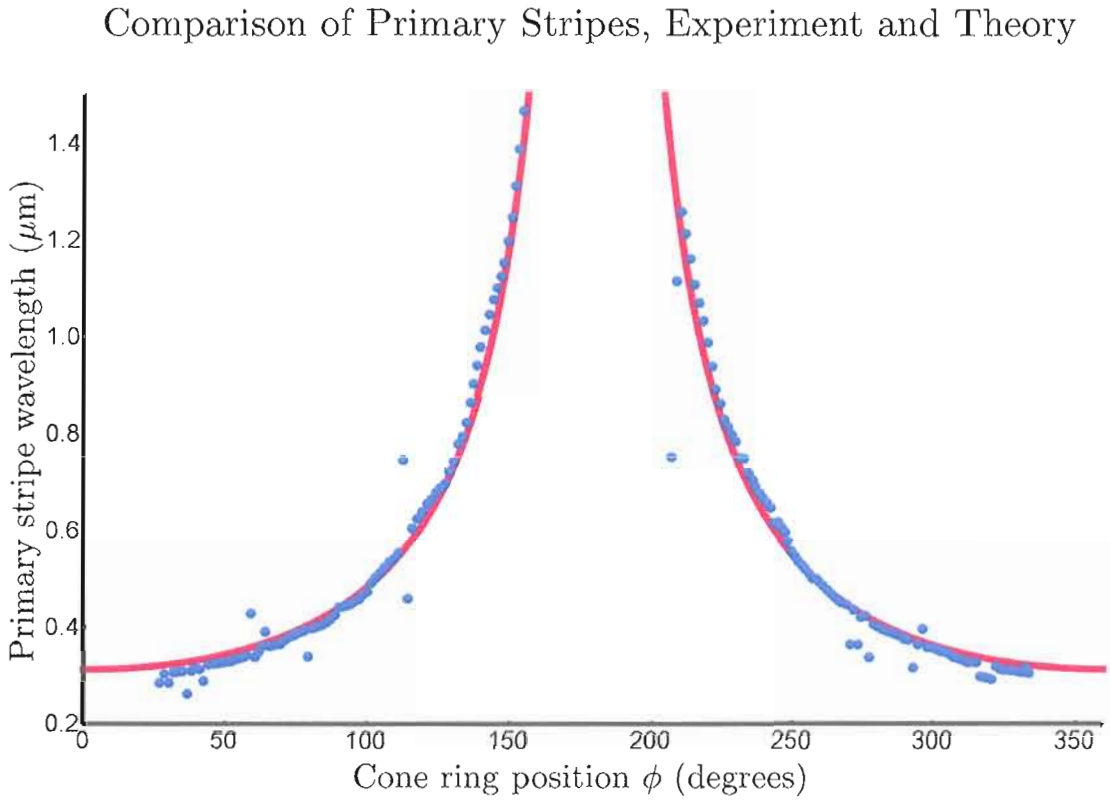

Figure 25: Comparison of primary stripes, experiment and theory. The comparison of the wavelength of the primary stripes obtained from experiment (blue points) with the expected value of the wavelength as determined by equation 46 (solid red line). The outlying points were left in to show the failure rate of the fitting method depicted in figure 23. The values used in equation 46 are $\theta_p = 44°$, $\lambda = 632.8$ nm, n= 1.457, where $k_0 = \frac{2\pi}{\lambda} n$, and $k_{sp} = k_0 \sin(\theta_{sp})$.

etry maps. These secondary stripes were often oriented in such a way as to suggest that they were caused by a SPP field traveling in the opposite direction to that of the excited incident SPPs. One known process that could account for this enhanced counter-propagating field is Coherent Back Scattering (CBS).

CBS is general to any wave propagating in a disordered scattering medium where multiple scattering occurs. The enhancement in the back-scattered direction is due to the constructive interference between a multiply scattered retro-reflecting wave and its "time-reversed" counterpart. Figure 26 shows two complimentary paths where one path traverses the scattering centers in the opposite order as the other path. The phase difference between the two paths depicted in figure 26 is given by $\triangle\phi = \frac{2\pi}{\lambda}(d_1 + d_2)$. Writing the distances d_1 and d_2 as projections of the vector $\overrightarrow{r_n} - \overrightarrow{r_1}$ onto the unit vectors $\hat{k}_i$ and $\hat{k}_f$ gives a phase difference for the two waves of $\triangle\phi = \frac{2\pi}{\lambda}(\overrightarrow{r_n} - \overrightarrow{r_1}) \cdot \left(\hat{k}_f + \hat{k}_i\right)$. As the direction of the reflected field approaches the back scattered direction $\hat{k}_f \rightarrow -\hat{k}_i$, the phase difference vanishes resulting in constructive interference between the two back scattered pairs. The summation over all time reversed pairs results in an enhanced coherent back-scattered field.

Figure 27 image A shows an example of our photometry data containing secondary stripes along with the prominent primary stripes. The intensity for a point on the cone ring given by equation 44 can be modified to include a second propagating SPP field which also undergoes single scattering from the tip. The direction of propagation for this second SPP field is described by the angle θ as measured counterclockwise with respect to the back-scattering direction ($-x$ direction). That is,

$$I(\phi, x_{tip}, y_{tip}) = \left|a_1 e^{i\Phi} + a_2 \exp\left[ik_{sp}x_{tip} + ik_0 \sin[\theta_p](x_{tip}\cos[\phi] + y_{tip}\sin[\phi]) + i\phi_2\right] + \right.$$

$$\left. a_3 \exp\left[-ik_{sp}\cos[\theta]\, x_{tip} + ik_{sp}\sin[\theta]\, y_{tip} + ik_0 \sin[\theta_p](x_{tip}\cos[\phi] + y_{tip}\sin[\phi]) + i\phi_3\right]\right|^2 \quad (47)$$

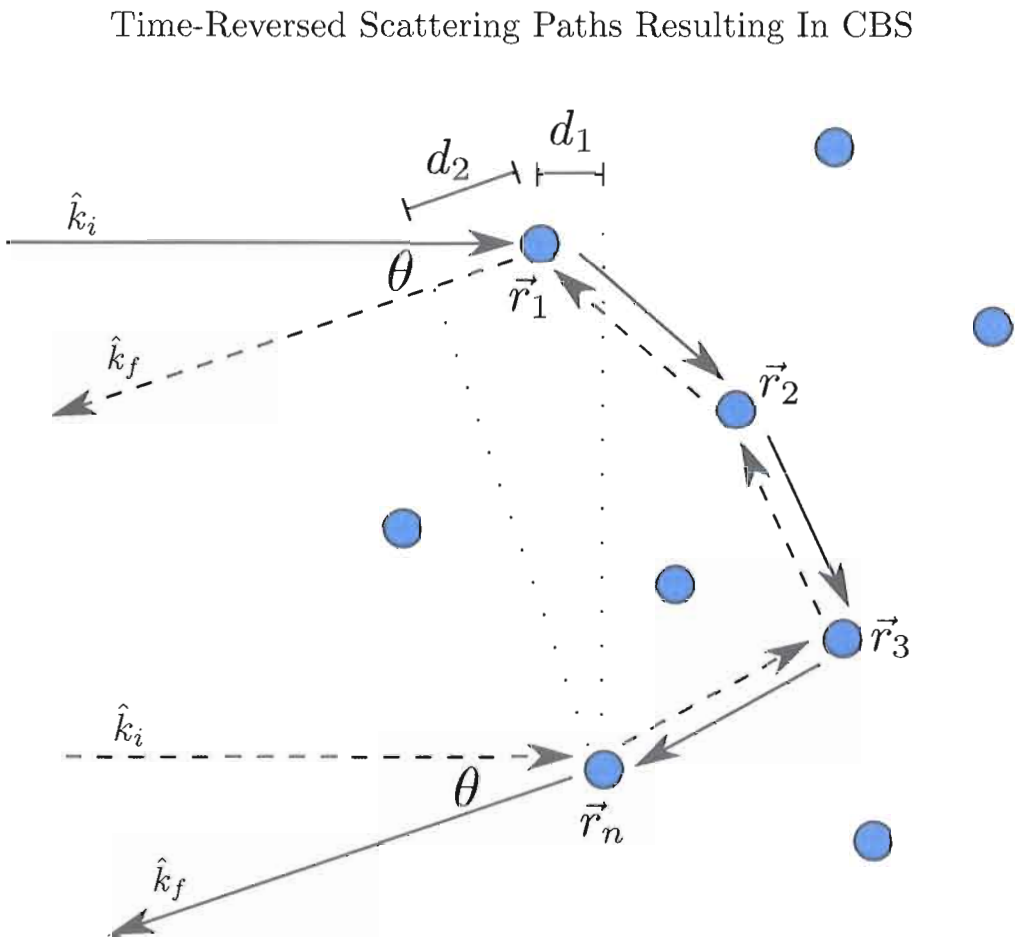

Figure 26: Time reversed scattering paths resulting in CBS. Two paths representing a coherent back-scattering pair for which the phase difference vanishes in the back-scattered direction resulting in constructive interference.

The same analysis for determining the direction of propagation of the SPP field from the orientation of the primary stripes can also be used to determine the propagation direction of a second propagating field based on the secondary stripes. Despite scanning many surfaces and the suggestive orientation of the secondary stripes, analysis performed on the many photometry images containing secondary stripes failed to conclusively reveal a CBS signal. The most likely cause of the observed secondary stripes in our data is single back-scattering from strong scatterers located sufficiently far away from the scan region. The reason why these secondary fields always appear to come from the downstream direction has to do with the fact that the scatterer is interacting directly with the incident SPP field of finite width. If the strong scatterer was not located within the downstream flow of the SPPs, its back-scattered field would most likely be too weak to register as secondary stripes.

While we did not directly observe the presence of a CBS field, our method does provide a possible means in which to do so. It also provides a way to test fabricated SPP mirrors and retro-reflectors and for categorizing their efficiencies. At the very least, this method allows us to detect the presence of strong scatterers that are down stream of the STM tip yet out of its scan region. It is conceivable that when the correct conditions are met, this method will reveal CBS.

In conclusion, we demonstrated that our experimental apparatus is capable of producing SPOM images that rival those obtained by collecting the entire sum of radiated cone light. By post-selecting which locations on the cone ring to contribute to the final SPOM image sum, the quality of the resultant SPOM image may be improved. We have also provided a detailed account for the stripes that often appear in SPOM/Photometry images. While these stripes are often a nuisance and their effects in photometry images are difficult to remove, they are useful for detecting strongly propagating SPP fields along the surface.

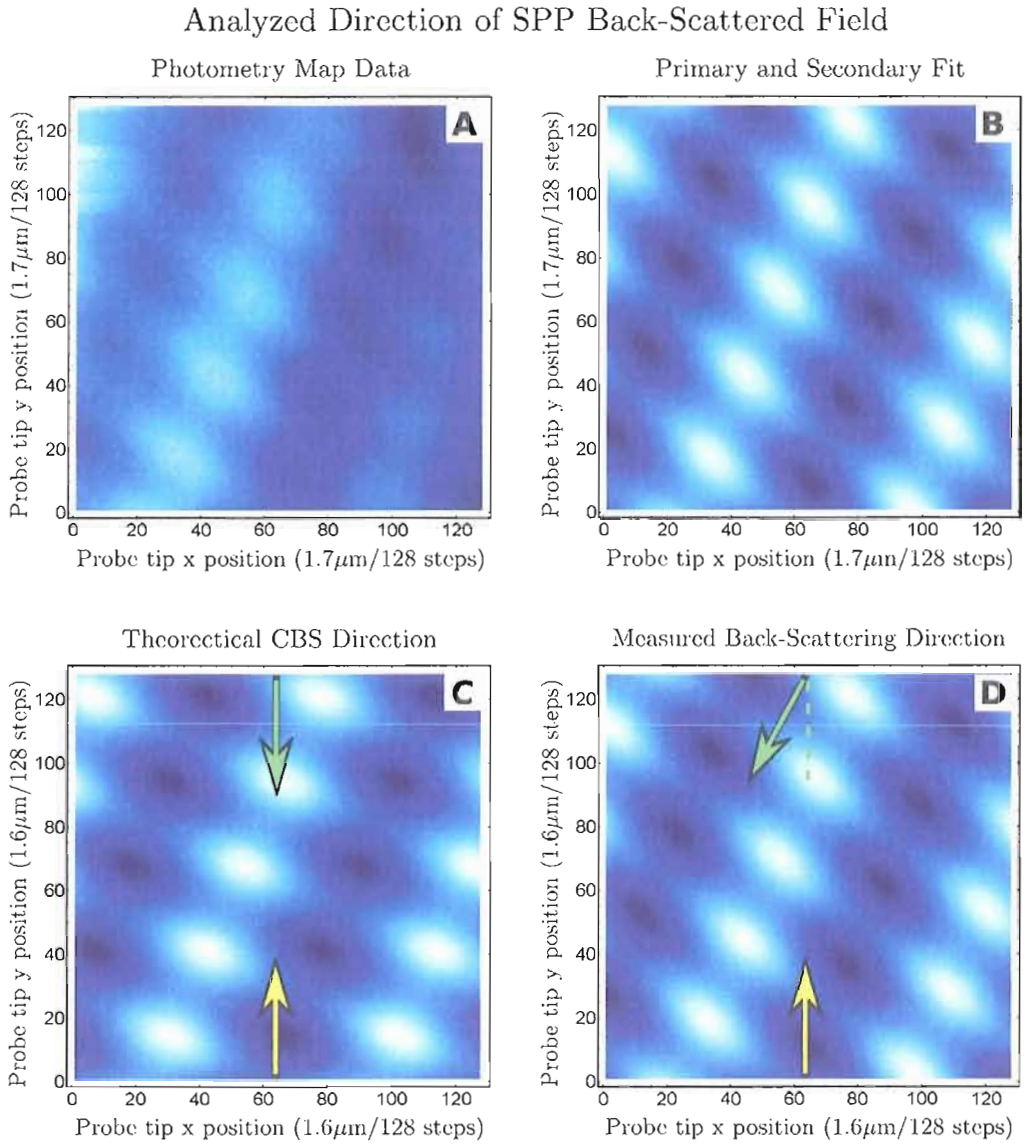

Figure 27: Analyzed direction of SPP back-scattered field. Image **A** shows primary (positive slope) and secondary (negative slope) stripes from a photometry map. Image **B** is the fit of the data represented in image **A** to the equation $a_p \sin[k_{xp}x + k_{yp}y + \phi_p] + a_s \sin[k_{xs}x + k_{ys}y + \phi_s]$ where the first term represents the primary stripes and the second term represents the secondary stripes. ϕ_p and ϕ_s are arbitrary phase shifts for the primary and secondary stripes. The fit was calculated according to the method described in figure 23. Image **C** shows the alignment of the secondary stripes for a field propagating in the back-scattered direction consistent with CBS ($\theta = 0$). Image **D** shows the plot of equation 47 with the angle θ picked to match the secondary stripe alignment found in the fitted data of image **B** in this case $\theta = 28.44°$. Thus, this field while suggestive, is not CBS.

CHAPTER V

CONE SPECKLE, RANDOM SCATTERING, AND OPTICAL VORTICES

V.1. Introduction

In chapter 4 we introduced the topic of optical speckle that makes up most of the conical radiation emitted from scattered SPPs and described the generation of photometry maps by recording the intensity fluctuations at a point within the radiation cone (on the cone ring) for each probe tip position. There is, however, much more to be said regarding the cone speckle and the photometry maps. In this chapter, we will develop these ideas further and delve into the topic of optical phase singularities also known as optical vortices. We will begin this chapter with a discussion on optical speckle as it relates to the field of SPPs. Next, we will discuss the behavior of optical vortices that are found in our experimental data, and finally, we will discuss our attempts to model our photometry images and the multiple scattering of SPPs through computer simulation.

V.2. Cone Speckle and SPP Scattering

Optical speckle is familiar to anyone who has ever turned on a coherent light source, such as a laser, and observed the optical pattern that is created from reflection off of a rough surface. The speckle pattern produced by a random wave field is characterized by the seemingly random spatial arrangement of amplitude and phase. One important class of speckle is the so-called Gaussian speckle, which is a well developed speckle originating from the interference of many highly coherent, highly

polarized wavelets with phases that are uniformly distributed over modulo 2π. As the number of wavelets contributing to the sum becomes very large, the probability density function of the real and imaginary parts of the amplitude asymptotically approach a Gaussian form giving the speckle its name [51]. Other types of non-Gaussian speckle is created when these conditions are not strictly met. For instance, speckle created by diffuse scattering from surfaces in which the rms roughness is much less than the wavelength of the source field will have statistical properties that differ from Gaussian speckle created from very rough surfaces. These differences allow characterization of surface roughness (over a limited range) by studying the speckle's statistical properties [46, 47]. A comprehensive treatment of the statistical properties of speckle can be found in Dainty's book on the subject [51].

There are a number of common processes that randomize the phase of coherent fields necessary for producing speckle, they include the reflection of an incident field from a rough surface, the propagation of a field through a medium containing random refractive indexes and the propagation of a coherent field through a medium containing random scatterers. In the case of the optical speckle generated in our experiment, randomization of the phasors occurs through the intermediary step of SPP random scattering (see figure 28).

The characterization of surface roughness in prism coupled SPP configurations, unlike the case for diffuse scattering, has largely been based on the angular distribution of light around the radiated cone rather than the statistical properties of the speckle itself [52, 53]. Figure 29 shows a sample of the qualitative variety of cone speckle for several of our prism coupled surfaces. Whether the speckle found in our cone rings, particularly cone rings created by tightly focused incident beams, is Gaussian has not been fully explored. It is clear, however, that the strong scattering of the probe tip will contribute a large phasor to the phasor sum and would need to be

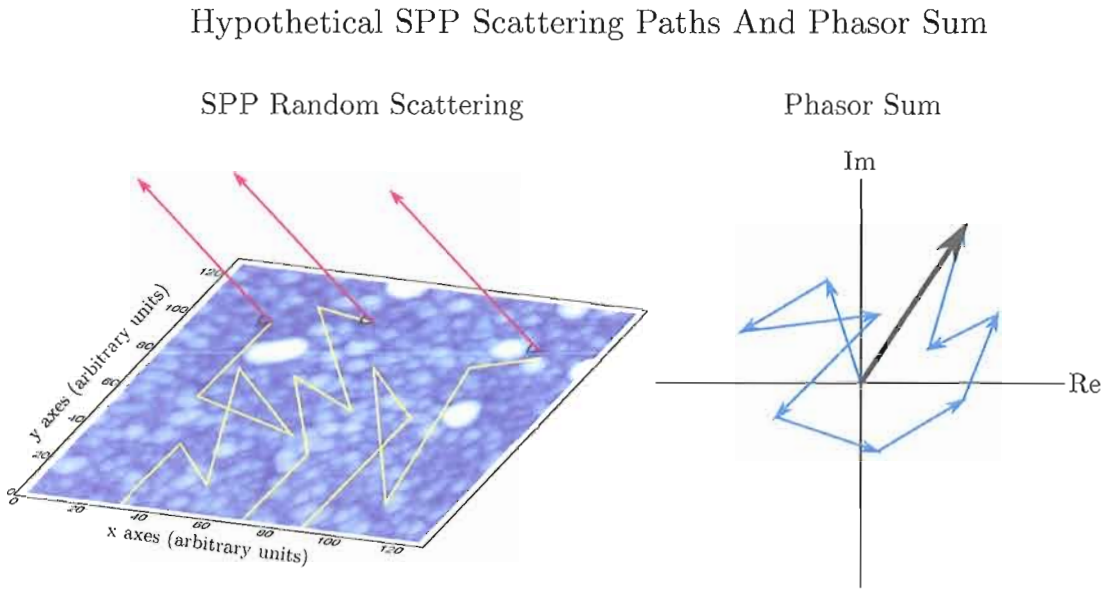

Figure 28: Hypothetical SPP scattering paths and phasor sum. The ballistic scattering paths of SPPs (shown in yellow) accumulate phase until they radiatively decay into the cone (red arrows). The radiated wavelets combine and interfere at locations in the cone ring producing speckle. The phasor diagram on the right shows the summation (black arrow) of the wavelets (blue arrows) with their own amplitude and phase.

accounted for in any statistical calculation.

V.3. Scattering Regimes

The STM surface topography of a typical silver film grown in our lab is pictured in figure 30. Although it is probably legitimate to view small single grains as individual point scattering centers for SPPs, the scattering effect of large grains contributing to surface roughness is less straightforward. For many purposes, however, both large and small grains can be modeled as point scatterers. In general, there are three main scattering regimes that determine the (elastic) scattering characteristics of a system. The first is the weakly scattering regime which is characterized by single scattering events over the lifetime of the particle. As the scatterer density increases, multiple scattering ensues and the so called weak localization regime emerges. Weak localization is characterized by the onset of coherent backscattering as discussed in chapter 4 and by second harmonic generation (SHG) where the incident SPPs interact nonlinearly with the counter-propagating SPPs to produce a signal of frequency 2ω that radiates normal to the surface [48]. Finally, as the scattering increases, strong localization, also known as Anderson localization, emerges. This occurs when the Ioffe-Regel condition is met, i.e. when $\frac{2\pi l}{\lambda} \lesssim 1$, where l is the elastic scattering mean free path and λ is the wavelength of the SPP. The Ioffe-Regel condition implies that the scattering frequency is so great, that the particle scatters before it is able to travel one full wavelength. This effectively inhibits propagation by trapping the SPP in the rough surface creating "hotspots" that are known to have field enhancements of many orders greater than the incident field [49, 50]. The silver surfaces grown in our lab are moderately rough, favorable for weak localization.

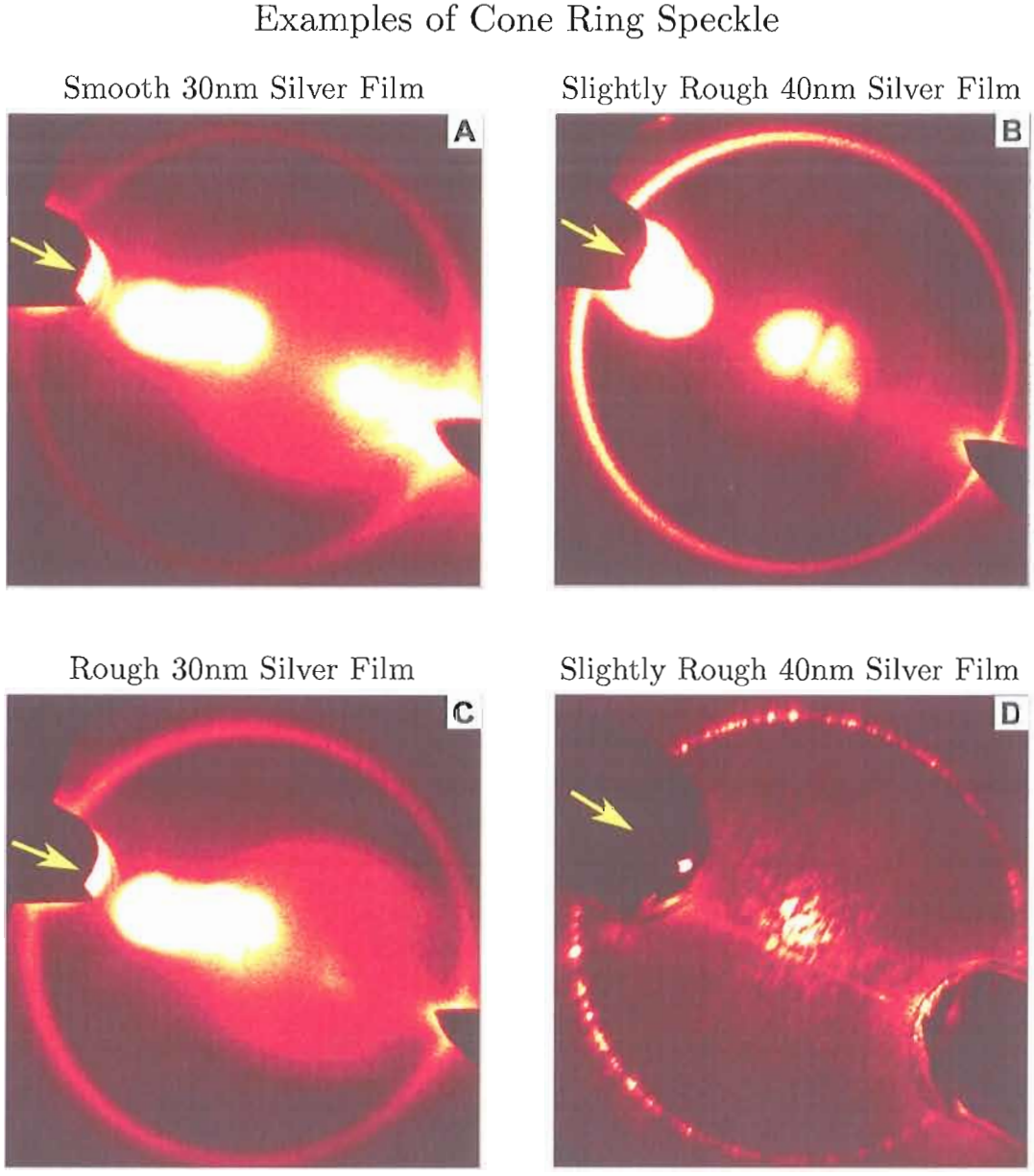

Figure 29: Examples of cone ring speckle. Image **A** shows a smooth 30nm silver film illuminated with a broad beam spot producing small speckle that is mostly forward scattered. Image **B** shows a rougher 40nm silver film illuminated by a broad beam. The sharper ring is a result of the thicker film and the brighter back-scattered field is consistent with a rougher surface. Image **C** shows a rough 30nm film which produces nearly uniform intensity around the entire ring. Image **D** shows the speckle from a 40nm silver film illuminated with a tightly focused beam spot. The size of the speckle is shown to increase as the spot size decreases as one would expect from diffraction theory.

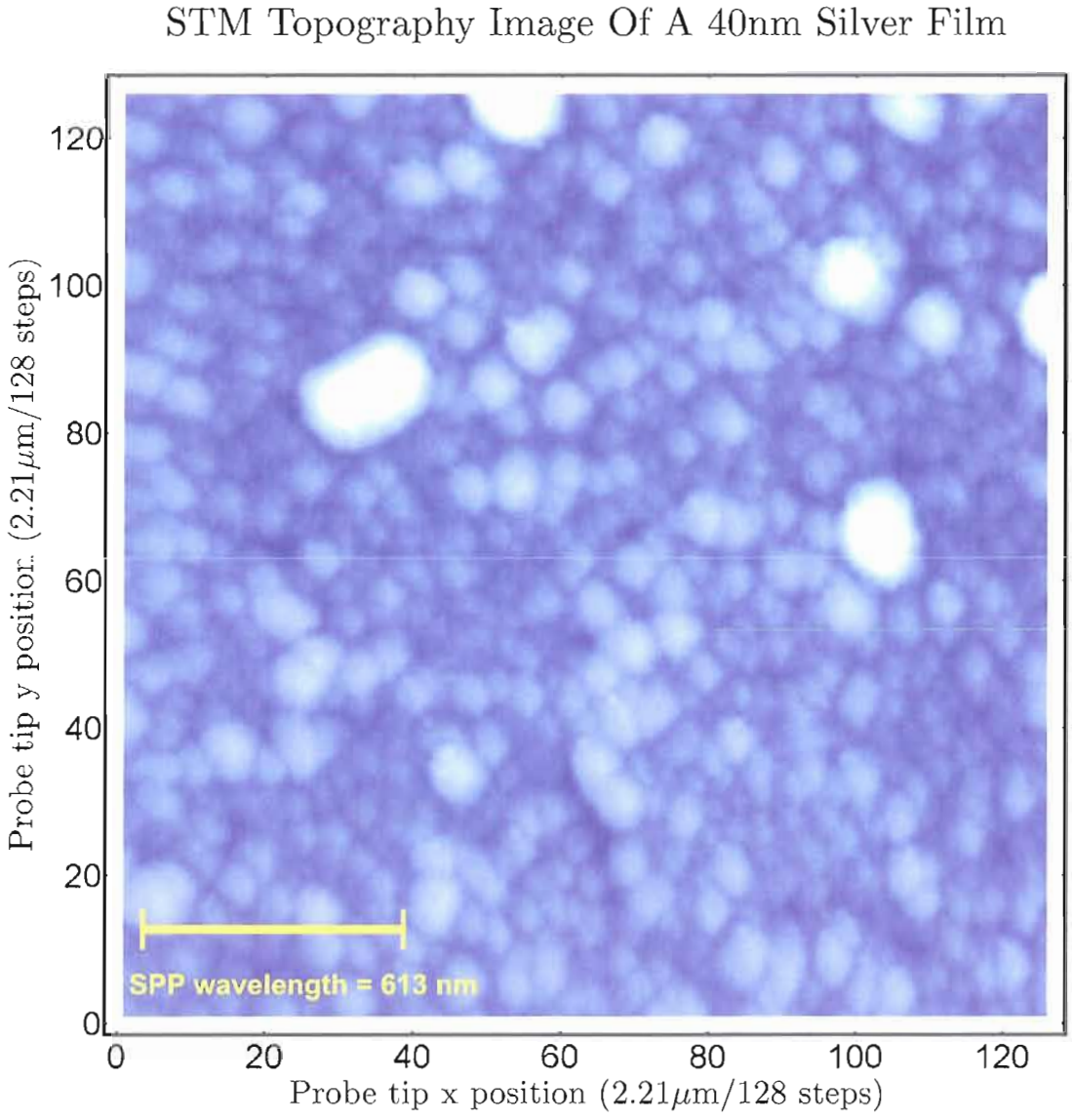

Figure 30: STM Topography image of a 40nm silver film. The film was vacuum-deposited at a rate of 0.4nm per second for a total thickness of 40nm. Shown here, are the crystal grains that serve as potential scattering locations for the SPPs.

V.4. Angular Momentum in Electromagnetic Fields and Optical Vortices

From electromagnetic theory, one finds that electromagnetic fields carry both energy and momentum. The momentum may be comprised of a linear part, with density given by $\epsilon_0 \mathbf{E} \times \mathbf{B}$, and an angular part, with a density of $\epsilon_0 \mathbf{r} \times (\mathbf{E} \times \mathbf{B})$. As one might suspect, the angular momentum may be further broken down into a spin part and an orbital part in analogy with particles in atomic physics. It is now well-understood that the spin angular momentum is associated with the field's polarization whereas the orbital part is due to its spatial distribution of phase.

Maxwell's equations require that the polarization of a freespace optical field lie orthogonal to the direction of propagation. In practice, we are often left with the task of determining where in the plane of polarization the polarization vector should lie. Displacing the phase between two orthogonal polarization vectors of equal length by 90 degrees results in light that is circularly polarized. It has been known since the time of Poynting [63], that circularly polarized light contains angular momentum associated with spin. Experiments performed by Beth [60] verified that the spin angular momentum contained in circularly polarized light is quantized by one $\hbar$ per photon.

Linearly polarized laser beams in the form of Hermite-Gaussian donut modes ($\mathrm{TEM}_{0,1} \pm i\ \mathrm{TEM}_{1,0}$) and Laguerre-Gaussian modes ($\mathrm{LG}_{p,l}$ with radial mode number $p = 0$ and azimuthal mode number $l = 1$) have a component of momentum in the azimuthal direction about the beam axes resulting in orbital angular momentum (see figure 31.) As with spin, the orbital angular momentum for these beams is quantized by one $\hbar$ per photon. In the case of Laguerre-Gaussian beams the orbital angular momentum is determined by the azimuthal mode number, l, giving a total angular momentum of $l\hbar$ per photon and a variation of phase of $l2\pi$ along a closed path around the beam axis. The amplitude of any beam exhibiting this phase structure

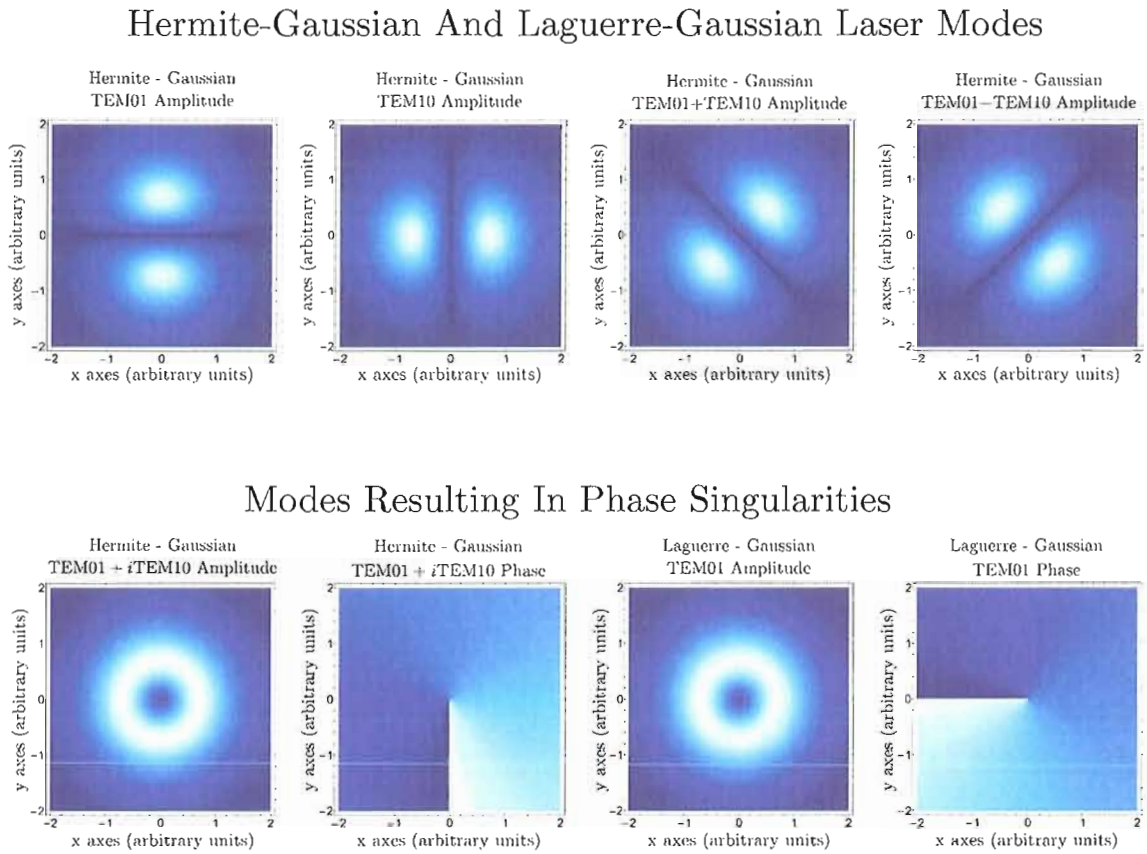

Figure 31: Hermite-Gaussian and Laguerre-Gaussian laser modes. Hermite-Gaussian modes are solutions to the Helmholtz equation in Cartesian coordinates. Laguerre-Gaussian modes satisfy the Helmholtz equation for cylindrical coordinates. The modes in the upper row have wavefronts of constant phase. Modes represented in the lower row contain phase singularities.

must vanish at the center to satisfy the wave equation resulting in a field containing a phase singularity.

The topological charge is the quantity used to describe the amount of 2π phase variation along a counter-clockwise closed path around a phase singularity. The topological charge is always given by an integer; if it is positive, then the phase advances and if it is negative, the phase retreats.

Illustrating an optical phase singularity is accomplished by considering the equation for a propagating field $u = A\exp(ikz - i\omega t)$ which satisfies the wave equation

$\nabla^2 u - \frac{1}{c^2}\frac{\partial^2}{\partial t^2}u = 0$ provided that the transverse Laplace equation $\nabla_T^2 A = 0$ holds. Here, A is the transverse complex amplitude, $\nabla_T^2 = \frac{\partial^2}{\partial x^2} + \frac{\partial^2}{\partial y^2}$ is the transverse Laplacian, and $k = \frac{\omega}{c}$ is the wave number. One particularly simple non-diffracting solution is $A = x \pm iy$ which produces a phase singularity at the point $(0, 0)$. A map of the phase around a phase singularity reveals contours of constant phase that radially spread out giving it a star-like appearance, hence, a singularity is often referred to as a "phase star" or "star dislocation" as shown in figure 32. As a consequence of its phase structure, the phase of a field propagating past a fixed location is seen to rotate at a rate ω. Spatially, the phase forms a rotating helix with its axis lying along the direction of propagation. Because of this behavior, phase singularities are also referred to as optical vortices.

Other solutions to the transverse Laplace equation are $A = x \pm \alpha iy$ and $A = (x \pm iy)^n$ (see figure 33). The real valued parameter, α, adjusts for the skew of the phase "radiating" from the singularities whereas the parameter denoted by the natural number, n, determines the order of the topological charge (the sign of the charge is once again determined by the sign of the imaginary term). Wavefronts with higher order topological charge (> 1) are commonly made using spiral phase masks and through computer-generated holographic diffraction [62].

V.5. Phase Singularities in Random Wave Fields

While the random array of bright spots are the most conspicuous feature of any speckle pattern, arguably its most important features are found within the dark regions, specifically, locations where the zeros of the real and imaginary parts of the electromagnetic field amplitude meet resulting in phase singularities. For well developed Gaussian speckle, there is on average one phase singularity for each bright speckle spot [54, 55, 56]. The number density of the phase singularities is inversely

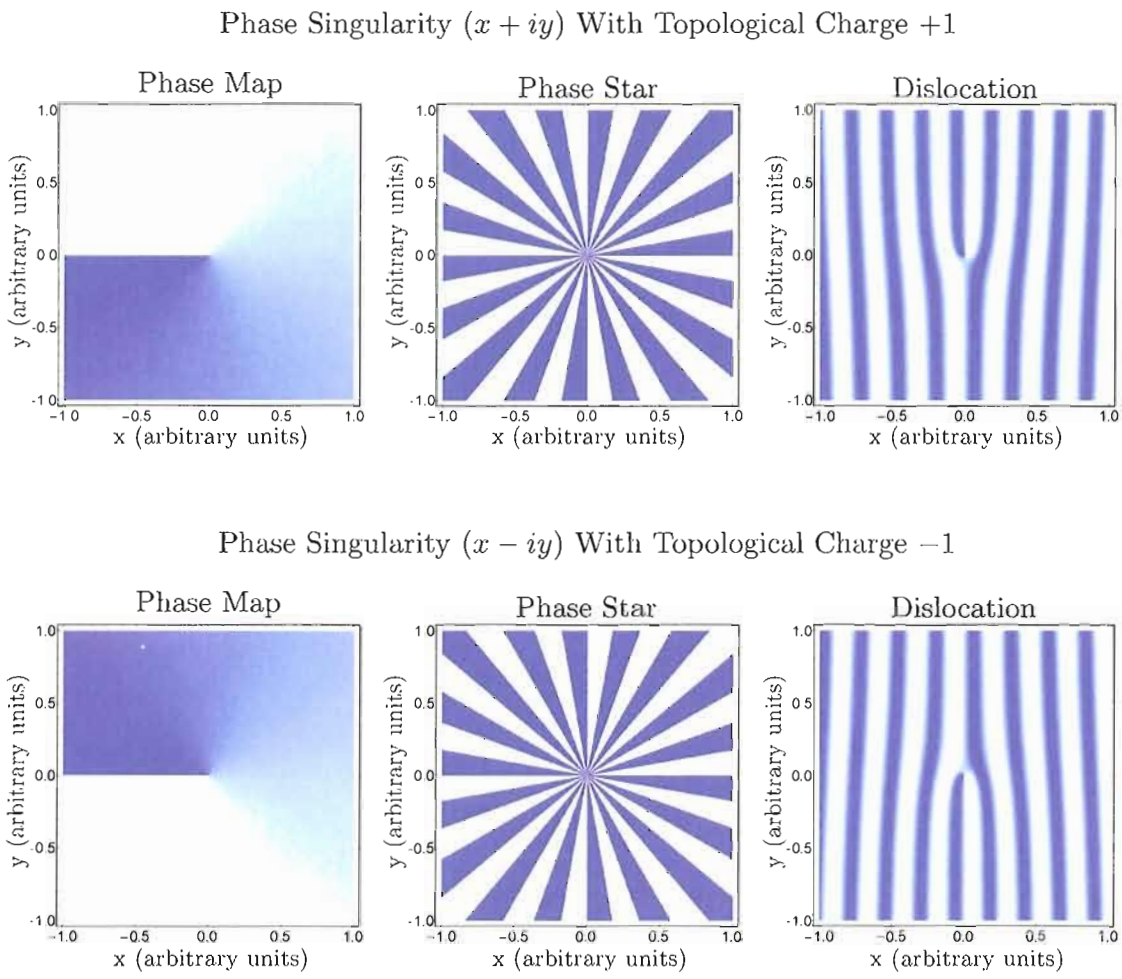

Figure 32: Common representations of optical phase singularities. The first row shows the phase plot for the transverse complex amplitude of a propagating electromagnetic field given by $x + iy$. The second row shows the phase plot for an oppositely charged field given by $x - iy$. The phase map ranges from $-\pi$ to π from light to dark. The phase star image is created by breaking the phase into 20° increments and the dislocation shows the intensity variations that occur when a tilted reference beam incident from the $-x$ direction interferes with the phase of the singularity.

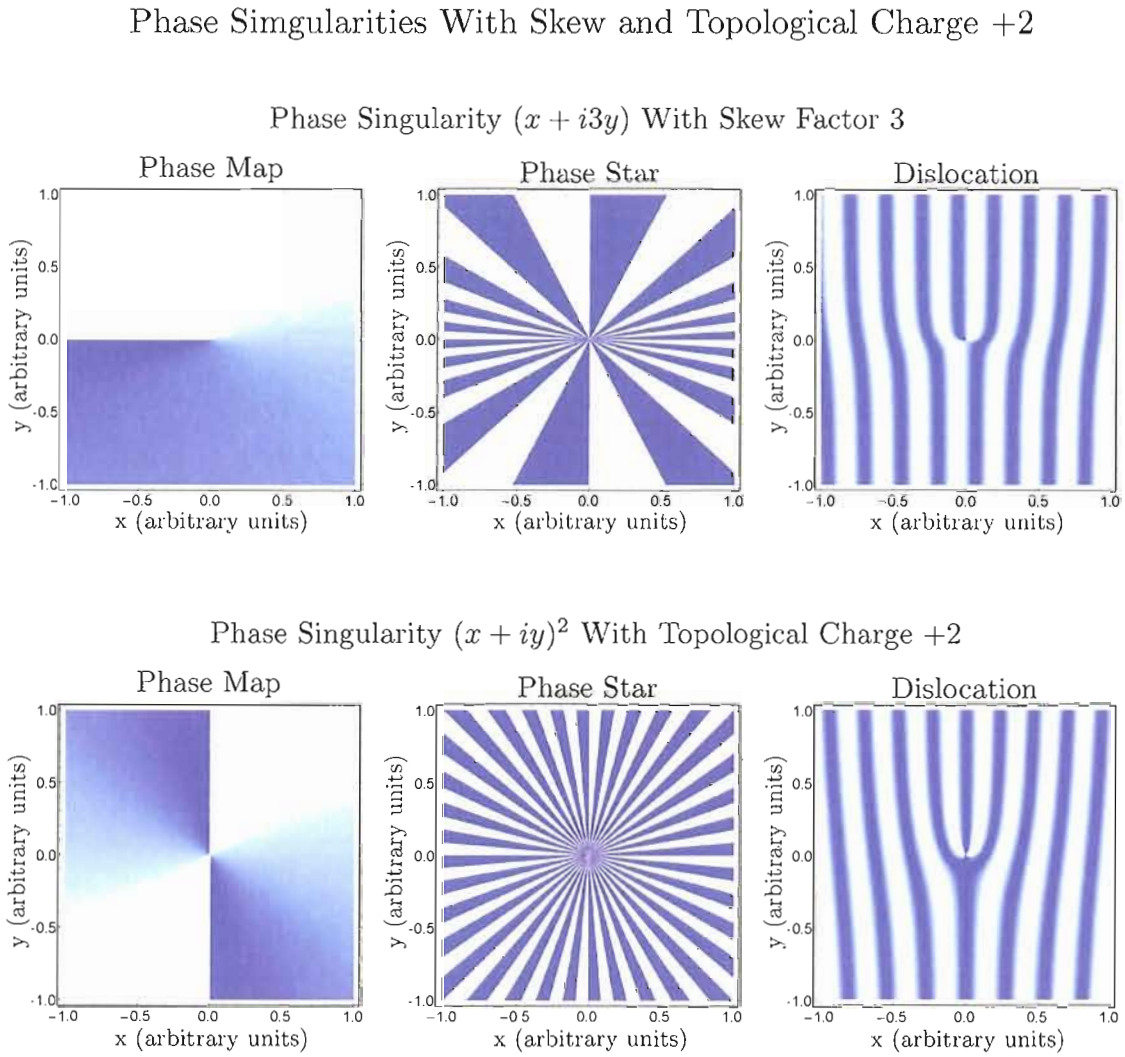

Figure 33: Phase singularities with skew and topological charge +2. The first row shows the phase plot for the transverse complex amplitude of a propagating electromagnetic field given by $x+3iy$. The second row shows the phase plot for an oppositely charged field given by $(x + iy)^2$. The phase map ranges from $-\pi$ to π from light to dark. The phase star image is created by breaking the phase into 20° increments and the dislocation shows the intensity variations that occur when a tilted reference beam incident from the $-x$ direction interferes with the phase of the singularity.

related to twice the coherence area of the speckle [58] where the coherence area is a parameter applied to speckle that provides a measure for the size of regions having constant amplitude and phase. The size of a speckle spot, for example, is roughly equal to the coherence area. Previous studies have shown that phase singularities in Gaussian speckle form loose networks in which the topological charge of one singularity is highly anti-correlated with the topological charge of its nearest neighbor, that is, nearest neighbors tend to have opposite topological charge [57, 58]. It is also unlikely to find random field phase vortices with topological charge other than ± 1 as this would entail the rare occurrence of vortices with like charges overlapping. This anti-correlation of vortice nearest neighbors is just one of the correlations that betrays the seemingly random nature of a speckle field [57].

Analogies can be drawn between topological charge and electric charge. For instance, contours of constant phase originate and terminate on phase singularities just as electric field lines originate and terminate on charges. This is due to the fact that an optical field must be single valued everywhere and therefore, regions of equiphase between two singularities must in some way connect up. As a result, the phase structure of a random wave field is entirely determined by the properties and positions of the phase singularities. It has therefore been argued, that knowing the position and properties of each phase singularity is sufficient for understanding the speckle field as a whole [59].

In general, a phase singularity with topological charge ± 1 satisfying the transverse Laplace equation can be fully described with six parameters of the form

$$A = (a_r + b_r x + c_r y) + i(a_i + b_i x + c_i y) \tag{48}$$

where the factors $a_r, b_r, c_r, a_i, b_i, c_i$ are real valued numbers describing the characteristics of the phase singularity. Unfortunately, there is no easy interpretation ascribed to these factors. Rewriting equation 48 in the alternate form

$$A = (X_n + i\alpha_n Y_n) \tag{49}$$

where

$$X_n = a_n \left[(x - x_n)\cos(\rho_n) + (y - y_n)\sin(\rho_n)\right]$$

$$Y_n = a_n \left[-(x - x_n)\sin(\rho_n + \sigma_n) + (y - y_n)\cos(\rho_n + \sigma_n)\right]$$

We are still required to define six parameters per vortice, but this time, they have well defined interpretations. The phase singularity center is located at (x_n, y_n) with anisotropy, α_n, orientation angle, ρ_n, skew angle, σ_n, and an over all scaling factor of a_n [59]. In this form, it is easy to construct a random wave field of our own design in terms of a product wave function

$$A = \prod_{n=1}^{N} (X_n + i\alpha_n Y_n) \tag{50}$$

While equation 49 satisfies the transverse Laplace equation, equation 50, does not. It has been demonstrated, however, that equation 50 can be closely approximated as a superposition of Hermite-Gaussian beams and is valid over a large volume of space [59].

Introducing a coherent background to a random wave field will cause the position

of the vortices to shift. Increasing the amplitude of the coherent background will cause oppositely charged vortices to seek one another out and annihilate. Equally charged vortices repel in the presence of a coherent background and as a consequence, multiply charged vortices will split into singularly charged vortices and drift away from one another. Figure 34 shows a network of vortices generated by equation 50 interacting with a coherent background.

V.6. Cone Speckle

In the laboratory, it is generally not possible to directly measure the phase information contained in an optical field. The fastest optical detectors are far too slow for resolving the phase of optical fields. One common technique for revealing this information is to interfere the field with a reference and observe the resulting interference fringes. This is the method we used for looking at phase information in the cone speckle.

When an inclined reference beam interferes with the phase structure of an optical vortex, a dislocation will appear in the fringes (dislocations in the fringes are seen in figures 32 and 33). While this is a useful technique for measuring the phase structure surrounding a vortex, it does have its draw backs. For example, the presence of the reference beam alters the phase and amplitude of the field in the region containing the vortex. It is also difficult to localize optical vortices with this method since the field amplitude surrounding the singularity is vanishingly small, resulting in weak to no interference.

We have observed optical vortices in the speckle pattern of the cone ring through the use of interference. This was accomplished in the typical way by splitting off a reference beam from the incident laser beam using a beam splitter. The incident beam was allowed to continue on normally to excite the SPPs. The reference beam was sent

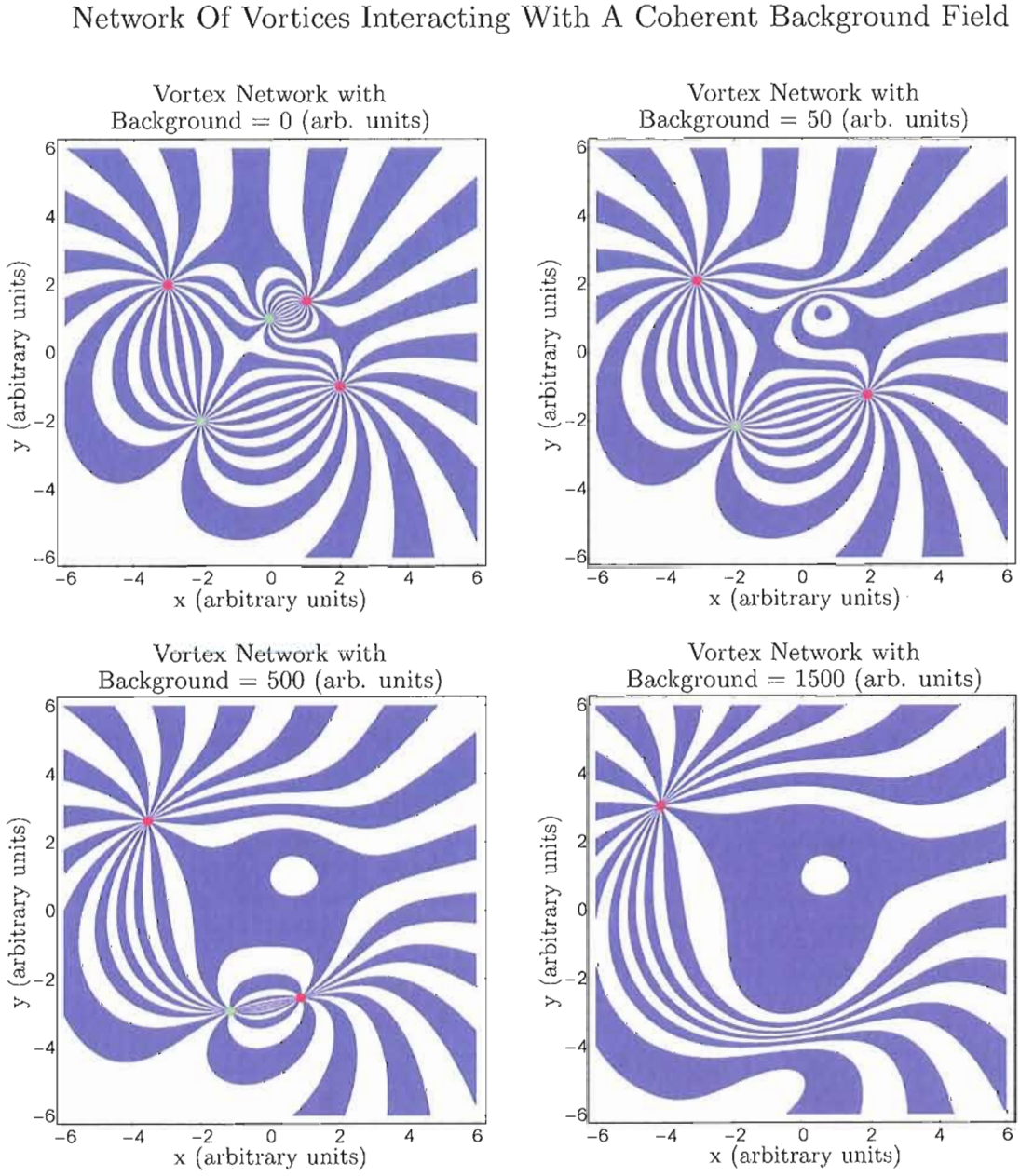

Figure 34: Network of vortices (shown as phase stars) interacting with a coherent background field. The vortice centers (x_n, y_n) are given by $\{(0,1),(2,-1),(-3,2),(-2,-2),(1,1.5)\}$ with anisotropies $\alpha_n = \{-1,1,1,-1,1\}$, orientation angles $\rho_n = \{0,0,0,0,0\}$, skew angles $\sigma_n = \{0,0,0,0,0\}$, and scaling factors $a_n = \{1,1,1,1,1\}$. The background field is created by adding on a real valued constant. As the coherent background increases, oppositely charged optical vortices seek one another out and annihilate.

through an attenuation wheel and steered to a beam combiner for interference with the expanding radiated cone. Before combining the two light fields, the reference beam passed through a bi-concave lens to produce wavefronts that roughly match the expanding radiated cone. Finally, a linear polarizer was placed in front of the CCD camera and the resulting interference pattern was captured. Figure 35 shows an example of the speckle with and without the reference beam revealing locations of optical vortices.

Scanning the tip out of tunneling distance near the surface will cause the vortices to wander amongst the shifting speckle. Occasionally, oppositely charged vortices will approach one another and annihilate only to spontaneously reappear (as oppositely charged pairs) and drift away. The addition of a coherent field will also cause oppositely charged pairs to merge and annihilate. Single scattering off the tip produces a large portion of this coherent field. As the tip moves the coherent phase changes in a predicable way. The tip's movement amongst the other scatterers will invariably change the over all scattering scenario and this too affects the speckle, but to a lesser extent. Figure 36 shows two oppositely charged vortices in the cone speckle annihilate with one another due to the movement of the probe tip.

V.7. Photometry Maps in the Absence of Background Fields

As we have discussed earlier, our photometry images are largely dominated by the presence of the primary stripes. For the primary stripes to emerge in the photometry, a background field must be present to provide the necessary interference. The speckle derived form scattering paths that do not include the tip provides a suitable background. Even the seemingly dark regions in the speckle usually contain enough background for producing stripes. There are, however, locations in the speckle that are dark enough (presumably near optical vortices). Here, the generated photometry

Locations Of Optical Vortices In The Cone Speckle

Cone Speckle With A Coherent Reference Field

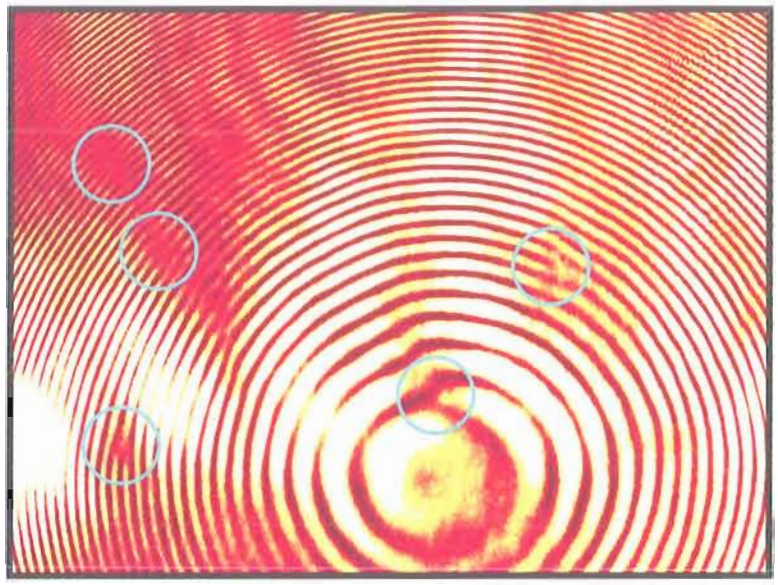

Cone Speckle Without A Coherent Reference Field

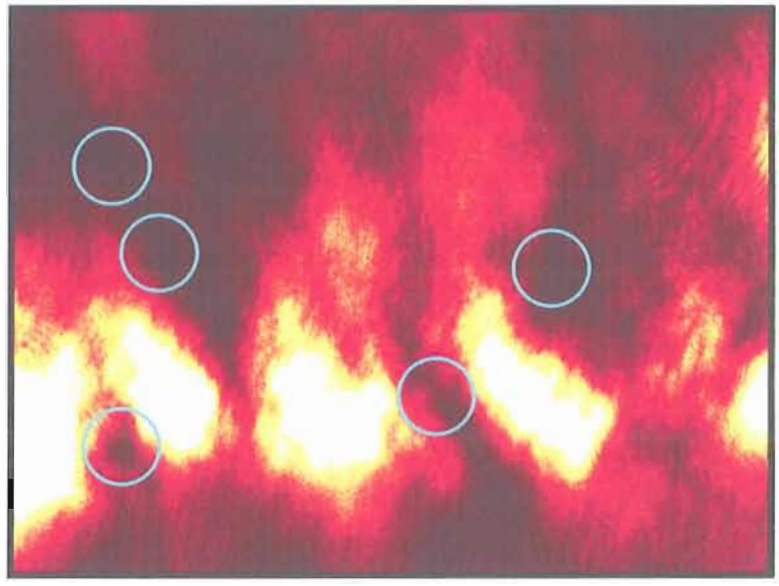

Figure 35: Locations of optical vortices in the cone speckle. The upper image shows the interference between the speckle and the reference beam revealing the optical vortices as dislocations in the fringes. The lower image shows the speckle with the same optical vortices encircled.

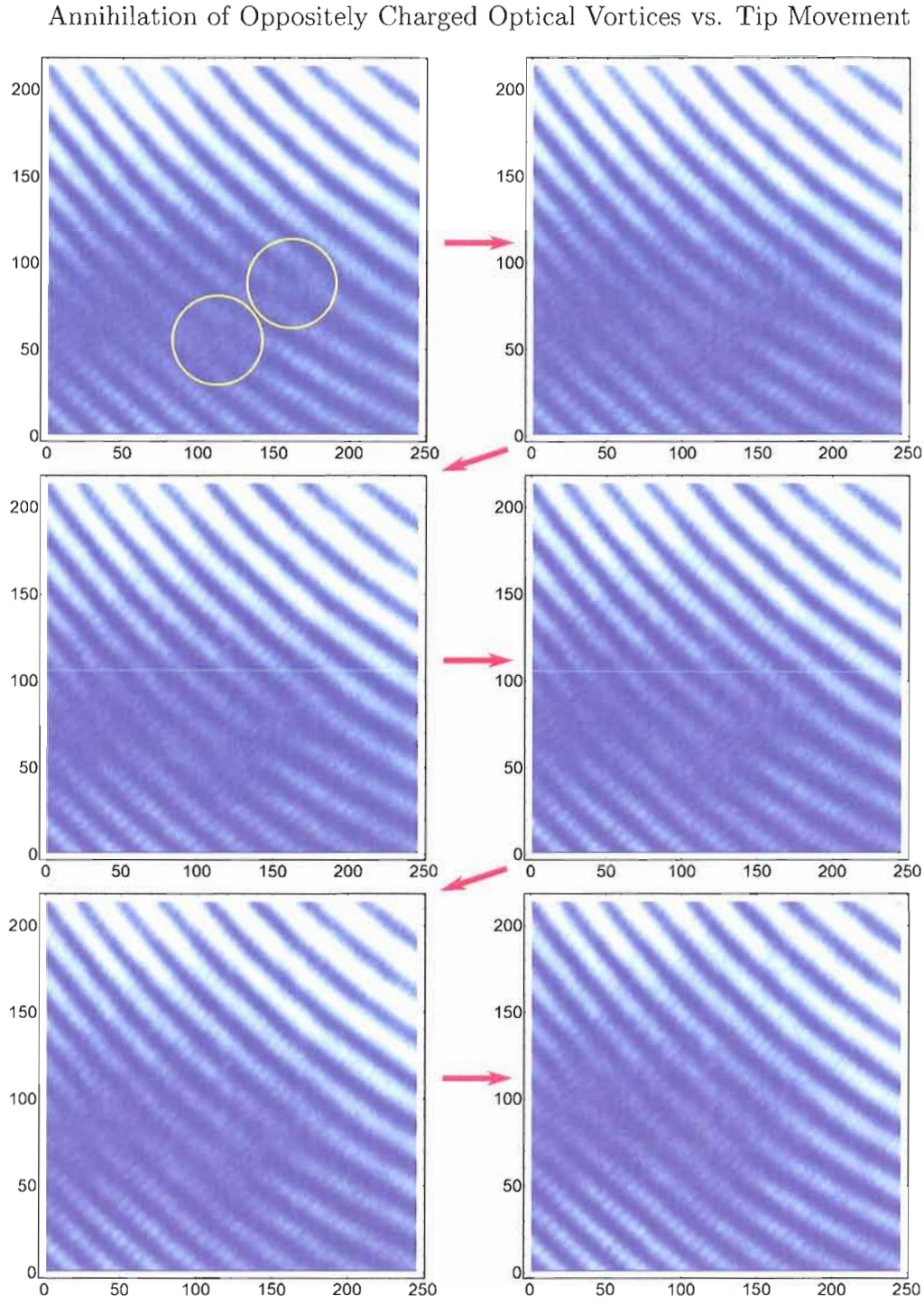

Figure 36: Annihilation of oppositely charged optical vortices vs. tip movement. The movement of the STM tip can cause oppositely charged optical vortices to merge and annihilate as well as spontaneously appear. From upper left to lower right, the tip was moved a total distance of $0.48\mu m$ in the $+x$ direction.

images are no longer dominated by the primary stripes and an underlying optical structure is revealed. This additional photometry information is the result of all scattering involving the tip minus all scattering paths not including the tip (effectively). Figure 37 shows a number of photometry images generated at these sufficiently dark locations.

Our experimental setup has a number of advantages for investigating this elusive underlying structure. For example, The CCD camera allows for many locations of the ring speckle to be recorded simultaneously for a given scan. This provides for a number of likely locations suitable for resolving the underlying structure. Another advantage is the short amount of time it takes to obtain large amounts of data. A typical scan takes less than two hours to complete with an additional hour for processing the data. There are, however, some drawbacks to the physical experiment. For instance, the inability to accurately record the phase of the speckle, and the inability to consider only certain types of scattering paths in the speckle sum. As a compliment to the experimental data, we also performed scattering scenarios using computer software performing Monte Carlo simulations.

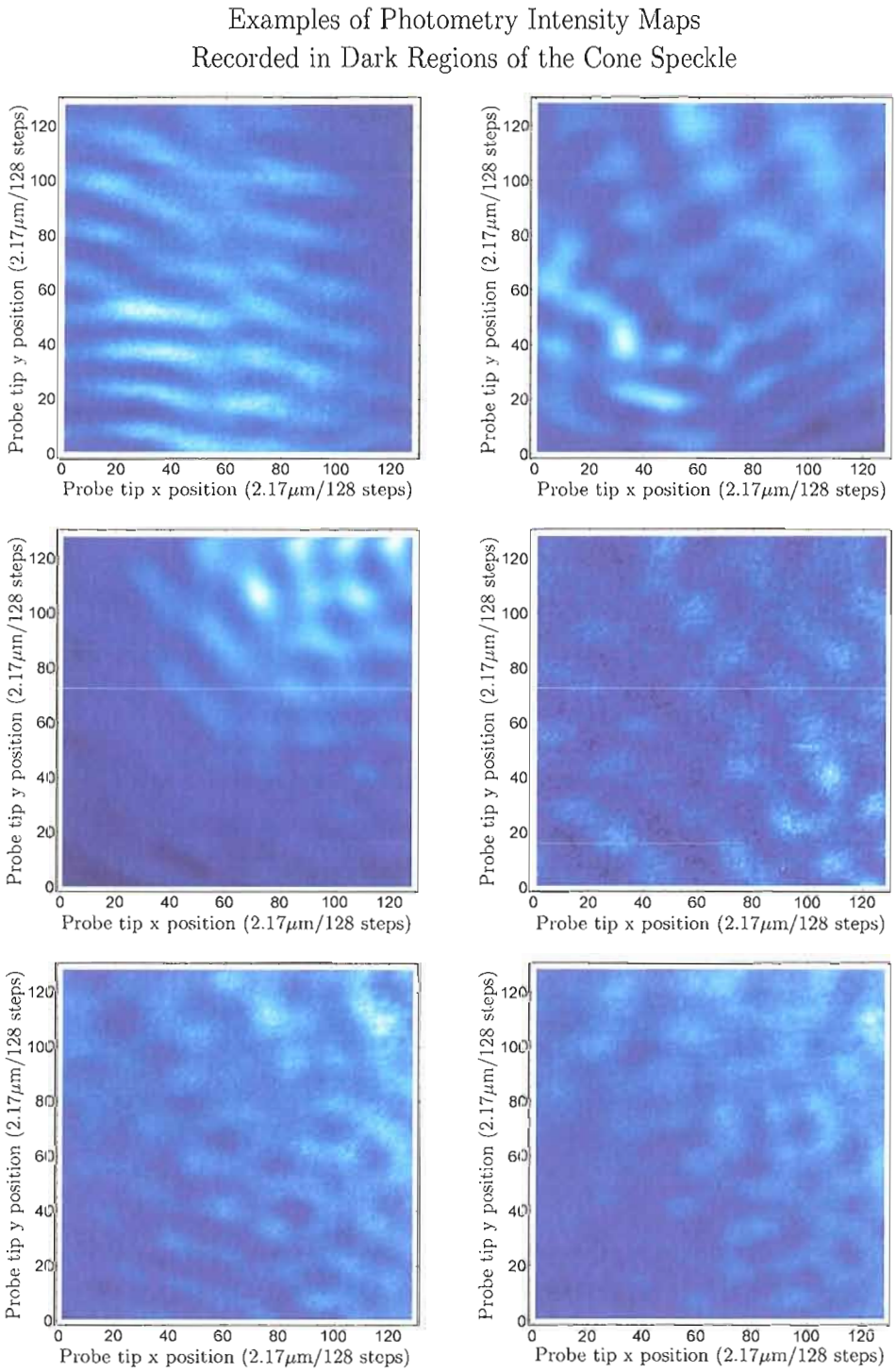

Figure 37: Examples of photometry intensity maps recorded in dark regions of the cone speckle. These photometry images reveal underlying optical structure from scattering events that involve the tip.

V.8. Monte Carlo SPP Scattering Simulation

The simulation software was written in the c programing language and implemented through Mathematica using the MathLink protocol (see appendix A). The software calculates the amplitude and phase of a single photometry frame from multiple SPP random scattering involving point scatterers and a moving tip (also modeled as a point scatterer). For each tip location, the program calculates N random scattering paths with a distributed coherence length L amidst the random array of point scatterers. The parameters N, L, the random array of point scatterers, as well as parameters defining the illuminated spotsize, ring observation angle, SPP wavelength and incident angle are defined by us before hand and passed along for use in the program. What are returned are arrays of complex amplitudes sorted into 7 distinct categories depending on the scattering paths encountered. The scattering categories include, all paths that do not include the tip as one of the scatterers, all paths involving single scattering off of the tip, all paths where the tip is the first scatterer, all paths where the tip is the last scatterer, all closed paths with the tip as the first and last scatterer, all closed paths with the tip as one of the scatterers, and all remaining paths involving the tip as one of the scatterers. Each category is mutually exclusive and is sorted accordingly from the most specific conditions to the most general.

The program provides insight into a number of features that we see in the physical experiment. It also may be used to design experiments that emphasize certain scattering effects. Here we present the results of a typical calculation using our scattering algorithm. We present a random array of 35 point scatterers (including the moving tip) shown in figure 38. Executing the scattering program "Cone" with 2.6 million scattering paths per tip location on a 128×128 grid ($2.27 \times 2.27 \mu m$) at a cone viewing angle of 0.6π measured counter clockwise from the $-x$ axis produces the photometry image shown in figure 39.

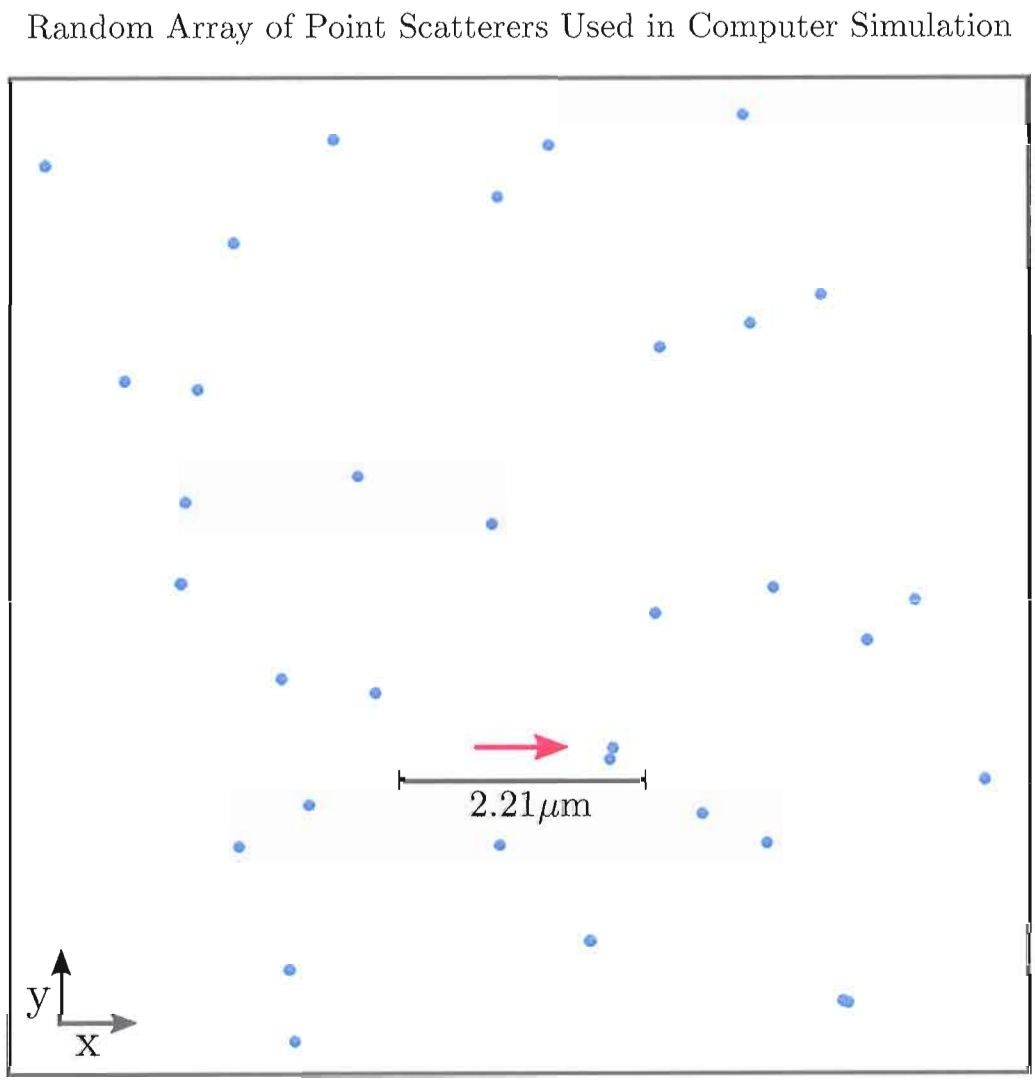

Figure 38: Random array of point scatterers used in computer simulation. The point scatterers are represented by blue dots. The gray oval (semi-minor axes $2.17\mu m$, semi-major axes $3.19\mu m$) shows the illuminated region where SPPs are excited. The reddish square shows the scan region for the tip scatterer ($2.21 \times 2.21\mu m$) and the SPP launch direction is indicated by the red arrow.

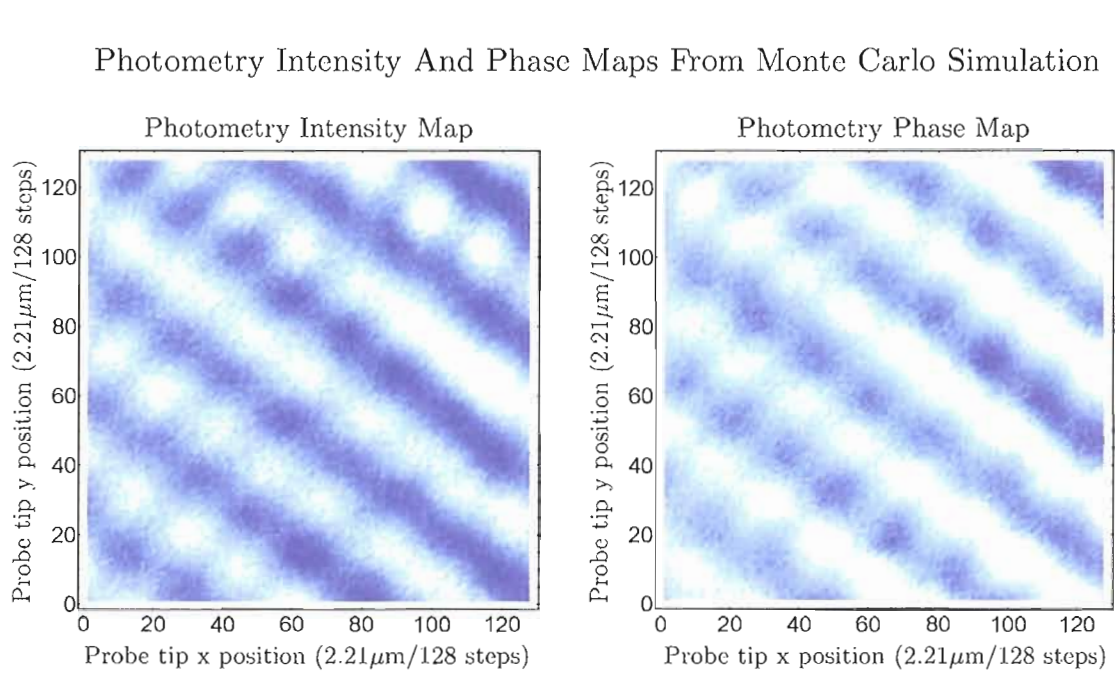

Figure 39: Photometry intensity and phase maps from Monte Carlo simulation. The primary stripes caused by single scattering of the incident SPP field off of the tip remains the dominant feature in both the intensity and phase.

As we see, both the intensity and phase of the full photometry is dominated by the primary stripes created by single scattering from the tip just as in our physical experiment. The primary stripes (figure 40) that appear in the photometry intensity can be eliminated in one of two ways. First, by removing all paths involving single scattering from the tip, or second, by removing the constant background field. The constant background field arises from the summation of all scattering paths that do not involve the tip. Since these paths are tip independent, it is expected that the complex amplitude of this field be normally distributed about an average value producing a constant background (figure 41). Removing this background field is similar to what is achieved in the physical experiment by recording the optical signal at locations on the ring near optical vortices. On thing worth noting is the dominance of single scattering from the tip in the structure of the phase map. The implications of this will become apparent soon.

Less dominant, but equally noteworthy are the set of secondary stripes that appear in the generated photometry which retains the background field, but excludes single scattering off of the tip. These secondary stripes are due to scattering paths involving the tip as the last scatterer effectively sampling a backscattered field emanating from scatterers located down stream from the tip and interfering with the background field.

One surprising result is the photometry maps generated in the absence of a background field have the potential for harboring optical vortices of its own kind. Figure 42 shows one such dislocation brought about by interfering the computed photometry map with a computer generated tilted reference field given by $ref = a\exp(iby)$. Where a is the mean amplitude of the photometry map, $b = \frac{60\pi}{180}$, and y is a scan direction coordinate.

As discussed previously, large fields have the ability to cause optical vortices to merge and annihilate. In practice, The field created by single scattering from the tip is often strong enough to dominate the phase structure of the photometry maps and wipe out all possible vortices. Reducing the effect of single scattering from the tip to one third of it's original value allows numerous vortices with both positive and negative charges to appear. In the physical experiment, one possible way of reducing the contribution of single scattering from the tip is to increase the effect of scattering from all of the other paths by roughening the metal film with an under layer of CaF2.

Finding optical vortices in the photometry maps leads to the ability of sweeping through an arbitrary range of integer 2π phase at an observation point in the cone speckle by guiding the tip through a closed trajectory. Figure 43 shows an example of this with the phase extracted from the computer generated photometry. While we only show two simple closed path examples, much more complicated trajectories can be imagined encircling any number of vortices of any charge. We are also looking at just a single location on the cone ring for which the background field is zero (albeit

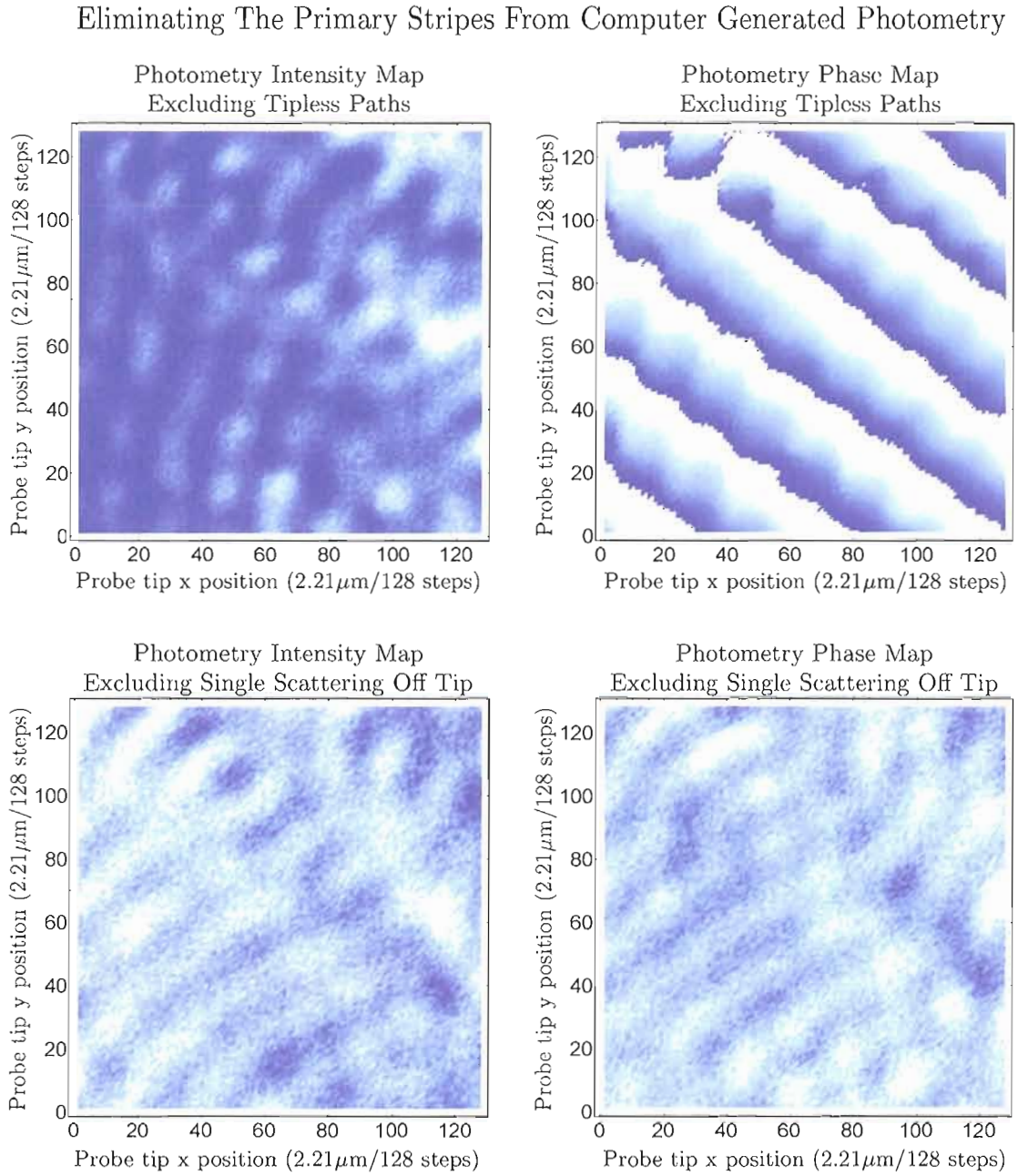

Figure 40: Eliminating the primary stripes from computer generated photometry. This is accomplished by suppressing single scattering off the tip (top row), or by suppressing the constant background field (bottom row) i.e. the field produced by the summation of all scattering paths that do not include the tip.

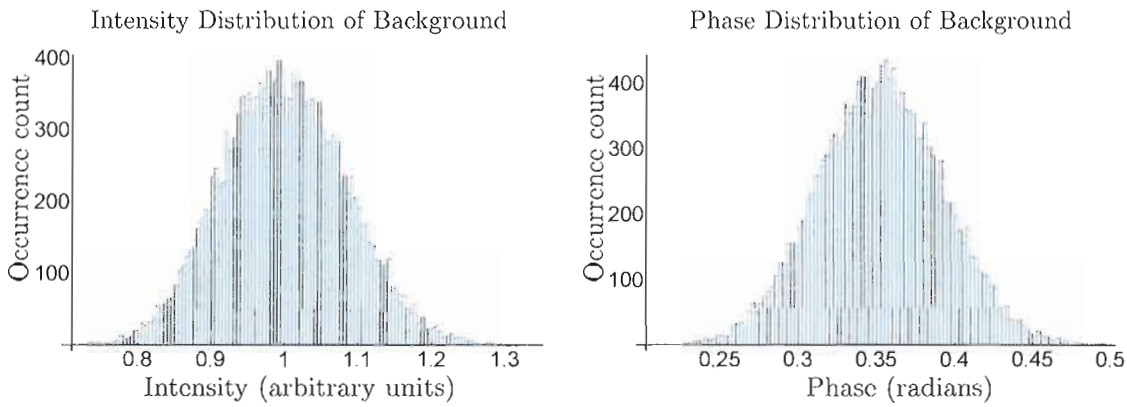

Figure 41: Distribution of intensity and phase of background field. Histogram showing distribution of intensity (in arbitrary units) and phase (in radians) of the background field found at a location in the speckle.

through our own suppression), however, there are many locations on the physical cone ring where the background field nearly vanishes. This raises further questions concerning how vortices are arranged in photometry maps at other locations on the ring and what the correlation may be, if any, between different photometry maps.

Based on our computer simulations, it is likely that the photometry maps produced by our physical experiment also harbor optical vortices at locations that are void of a background field so long as single scattering from the tip is not overwhelmingly large. This raises the question, what is the origin of the vorticity found in the photometry maps? Perhaps the summation of all the scattering paths involving the tip produces a field that causes an optical vortex from the background field to sweep through the observation point resulting in an optical vortex to appear in the photometry. While this can happen, our Monte Carlo simulation shows that we observe vortices in the photometry when the background field is entirely removed. However, the idea that optical vortices are still present in the real space speckle and are sweeping through the observation position is very likely. Their origin must then be due to the summation of scattering paths that involved the tip. Verifying this likely cause has not yet

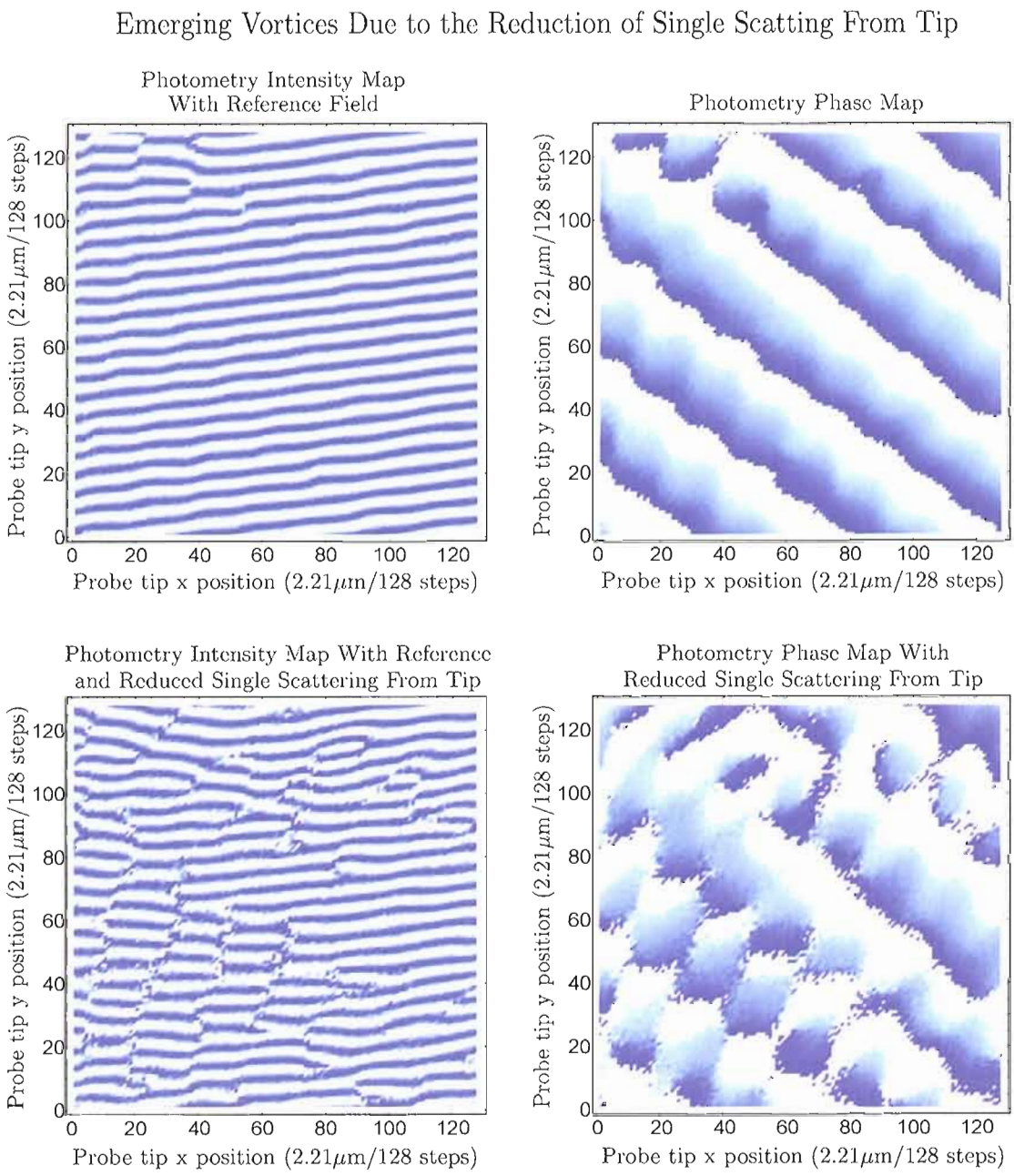

Figure 42: Emerging vortices due to the reduction of single scattering from tip. The optical dislocations are revealed by interfering the computer generated photometry map (excluding the background field) with a tilted reference. The intensity of the photometry was normalized to improve the interference revealing the dislocations.

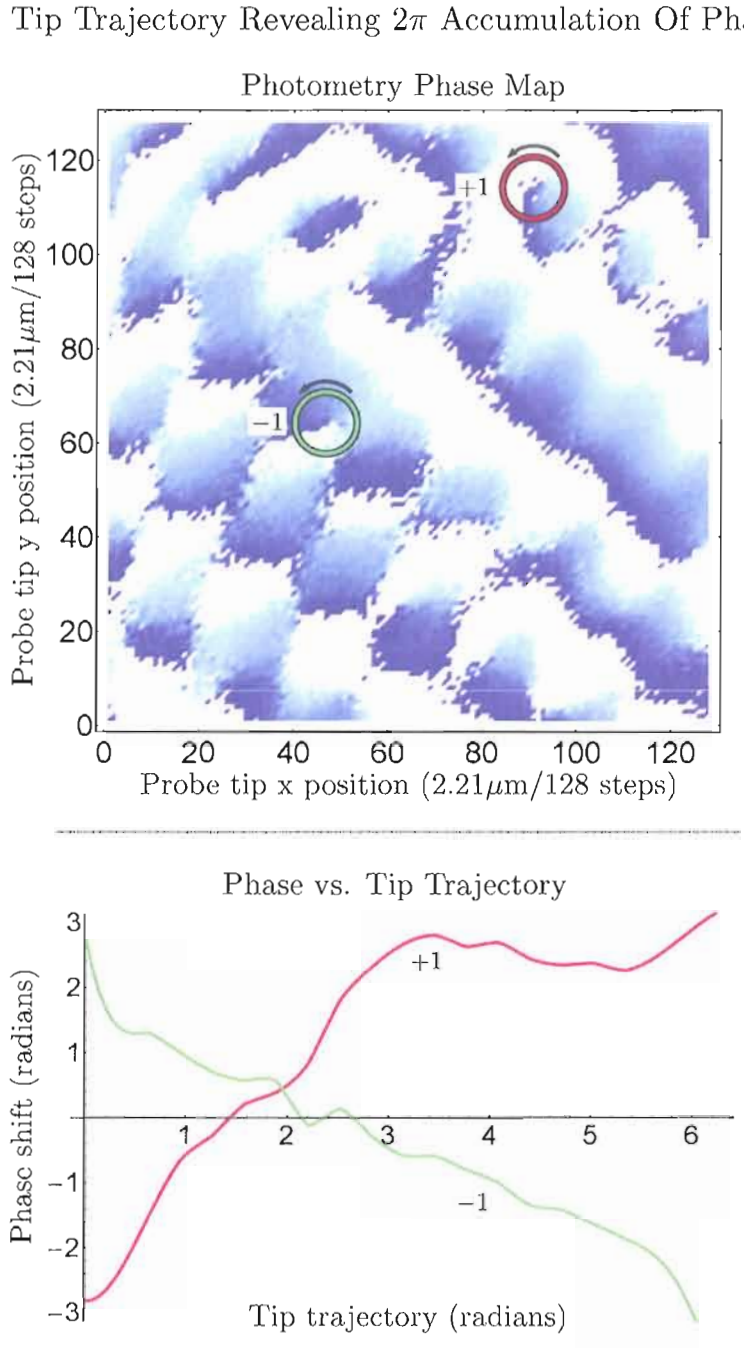

Figure 43: Tip trajectory revealing 2π accumulation of phase. Two counter clockwise tip trajectories are shown in the photometry phase map around a positively charged $(+1)$ and negatively charged (-1) optical vortice. The corresponding phase shift seen at the observation position on the ring is shown in the phase vs. tip trajectory graph.

been done due to computation limitations. However, if this does turn out to be the explanation, it implies that we have far more control over the positioning of optical vortices in the far-field than what we have currently been able to show in the physical experiment.

V.9. Future Projects

In these experiments, the scatterer positions are randomly distributed according to the roughness of the metal film. However, there is no reason why one could not place scatterers at any desired location on a sufficiently smooth film. Creating scattering arrays lithographically on the surface may enable one to have further control over the vortex structure within the photometry maps and far-field speckle.

Figure 44 shows an example of the photometry generated using four evenly positioned point scatterers. Strangely enough, the photometry intensity map reveals what appears to be the locations of the four point scatterers within the scan. It is generally not clear from the photometry images the location of the scatterers on the film. A reverse transformation from photometry maps to scatterer locations remains illusive. While the multiple scattering systems are complex, there is an abundance of information encoded in the phase and intensity of the speckle as well as the phase and intensity of our photometry maps.

We have shown in the physical experiment that optical vortices in the far-field speckle pattern can be manipulated, created, and destroyed by moving the probe tip within the near field region of the SPPs. Through computer simulation, we have found that vortices, while static in the photometry space, may have a dynamic counterpart in real space for which we have a great deal more control. These regions are accessible to us in the physical experiment through the dark regions of the speckle. One additional avenue worth pursuing is SPP vortices on the metal film surface.

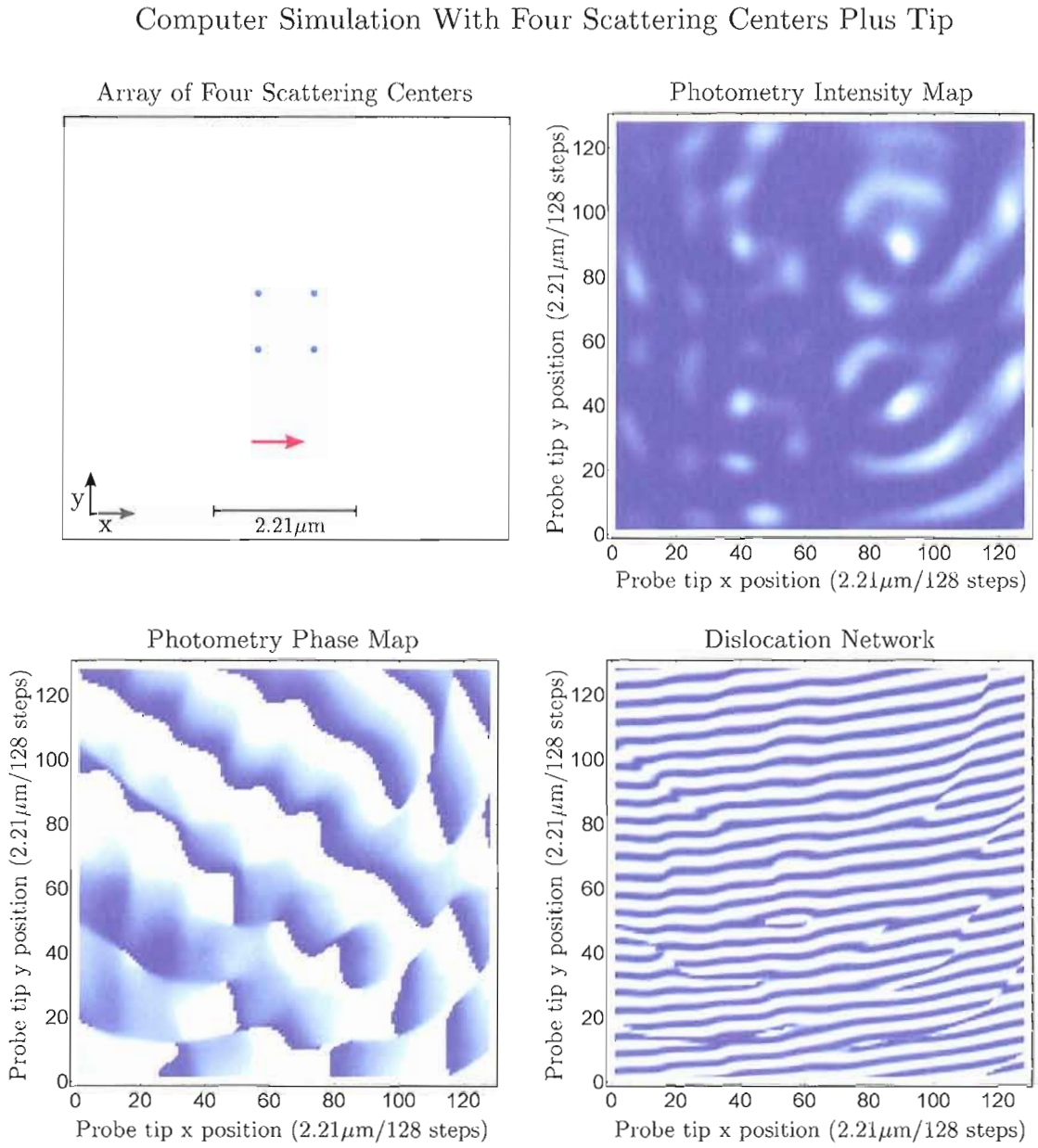

Figure 44: Computer simulation with four scattering centers plus tip. Generated photometry maps for four regularly positioned point scatterers showing intensity and phase map photometry.

A rough, multiple scattering, random surface would be very conducive for finding SPP vortices provided that the surface field isn't dominated by the strong incident beam used to excite the SPPs. The strong incident field would invariably bring about the annihilation of any vortices that might otherwise exist on the surface.

The creation of phase singularities requires a minimum of three interacting, tri-directional waves (Figure 45). Optically exciting SPPs on a smooth metal film with an appropriate combination of equally intense beams from multiple directions can lead to SPP vortices on the surface. The strong in-plane scattering characteristics of the probe tip could then be used to manipulate the SPP vortices on the surface. Figure 46 shows a possible scenario for creating SPP vortices using only two orthogonally propagating excitation beams. The necessary third field would result from strong scattering from the probe tip. In this scenario, the probe tip samples the local field created by the summation of the orthogonally propagating SPPs and would radially scatter the field within the plane. This ensures that the probe tip is a dominant participant in the creation of the SPP vortices and therefore, exerts control over their behavior.

Optical vortices have been demonstrated to trap (optical tweezers) and impart angular momentum to particles [64, 65]. Optical vortices have also been suggested as a way to drive micro-machines [66]. In the same way, SPP vortices on a metal surface may be a useful way to perform these tasks with the added benefit of using a movable scatterer as a transmission and clutch for positioning SPP vortices to locations where they are needed.

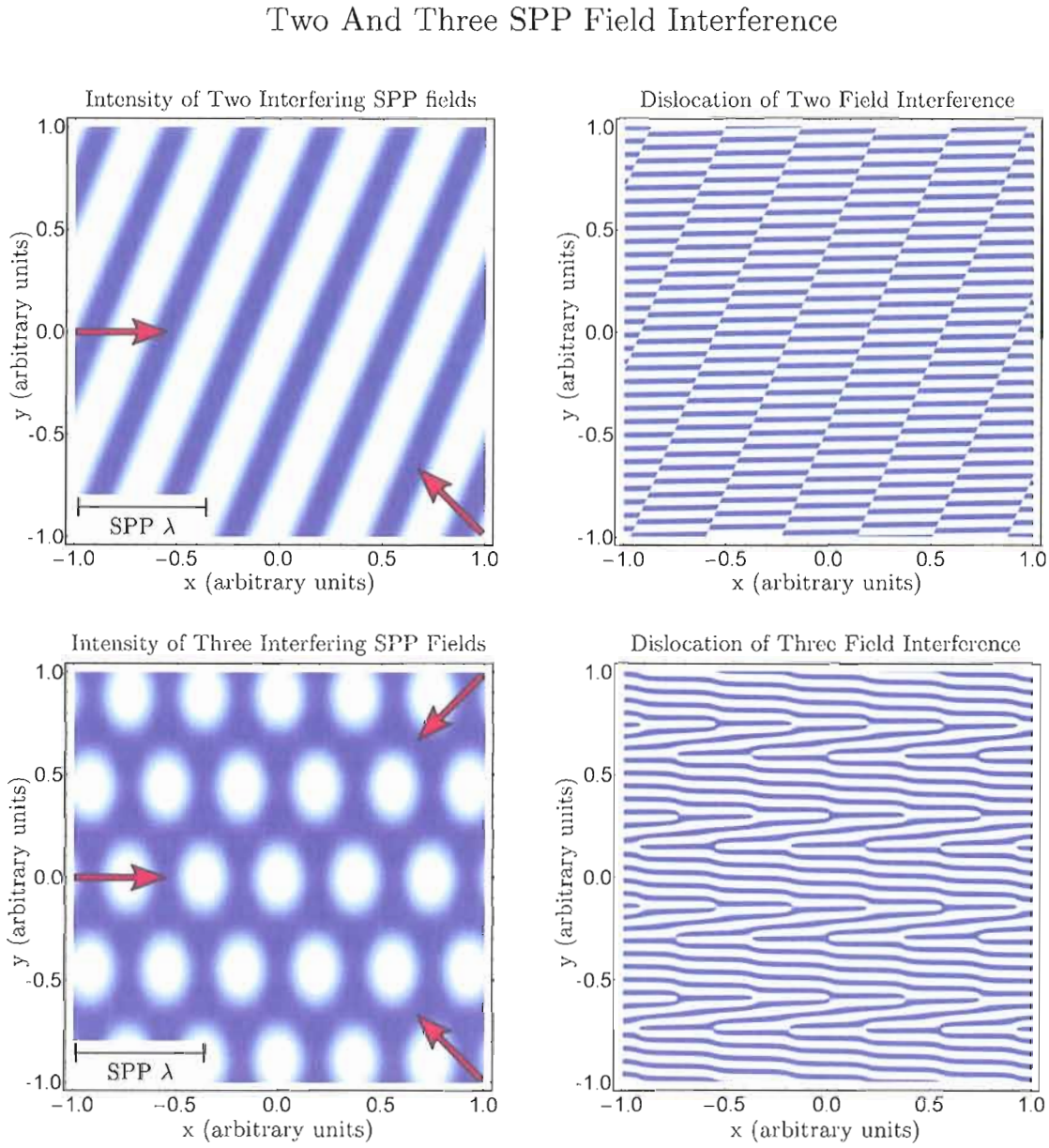

Figure 45: Two and three SPP field interference. Intensity and phase information from the interference between two and three incident SPP fields. The direction of the incident fields are indicated by the arrows in the intensities. The images on the left show the response of the fringe when a reference beam interacts with the underlying phase. When two fields interfere, the phase skews, but no phase singularities appear. When three fields interfere, a regular array of positively and negatively charged phase singularities appear.

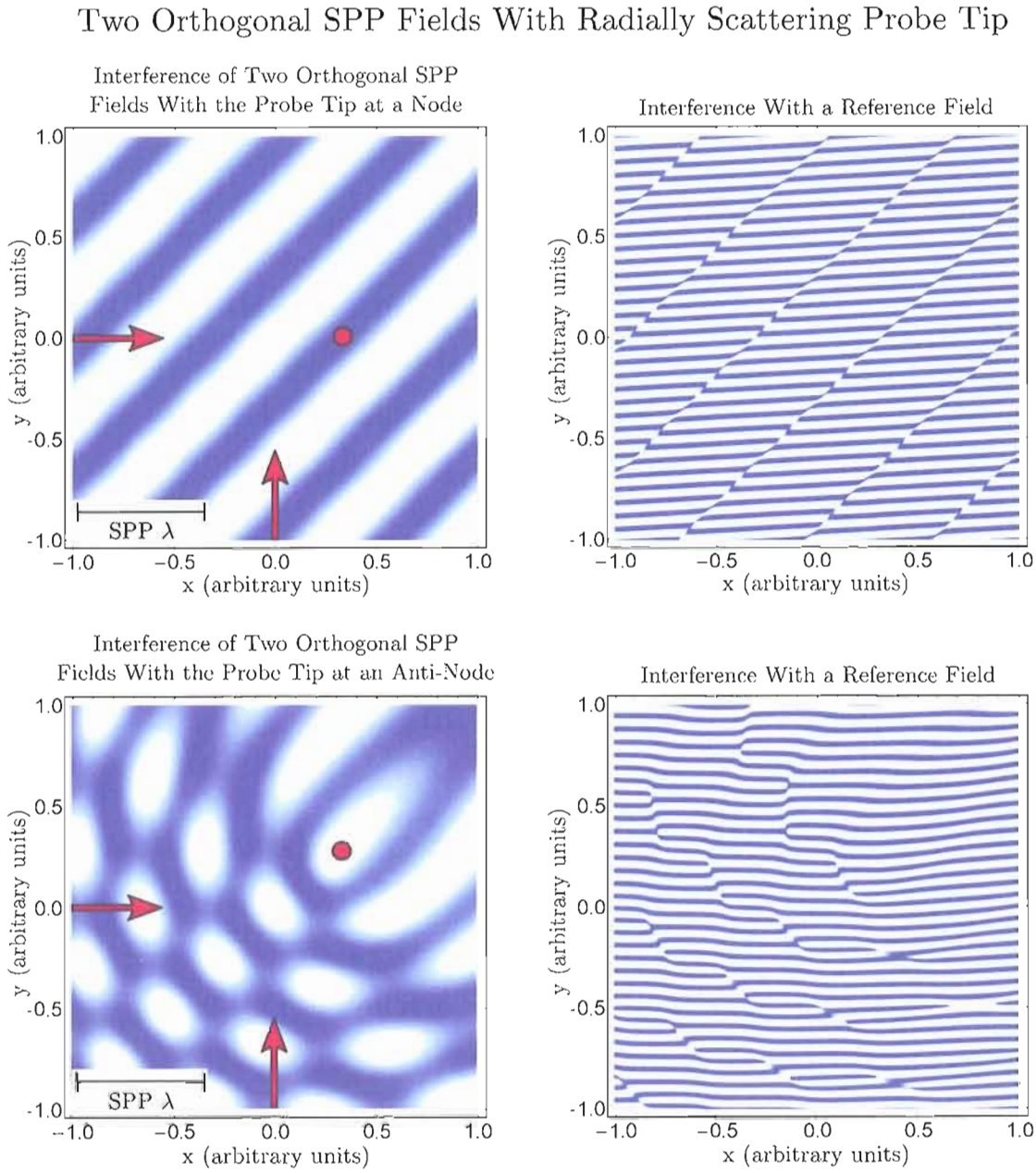

Figure 46: Two orthogonal SPP fields with radially scattering probe tip. The probe tip (shown as a dot) provides the third field necessary for the creation of SPP vortices by radially reflecting the local field created by the two incident beams. The direction of the incoming SPP fields are indicated by the arrows.

CHAPTER VI

CONCLUSION

VI.1. Conclusion and Future Work

Our study of the optical characteristics of the radiated conical field emitted by the decay of scattered SPP interacting with the scanning probe tip of an STM has rarely been a straight forward process. This is not to say that there was ever a lack of things to study. Often times, our investigations headed off into previously unintended directions where topics were shelved to make room for pursuing other questions only to be revisited later. This way of approaching questions allowed us to cover a fair amount of ground. For a conclusion, I will summarize our major findings and provide topics for future research.

We were interested in what could be understood by measuring the radiated conical field in the far-field as a scatterer was moved amongst the SPPs in the near-field. We knew that the conical field contained speckle and that this speckle was largely ignored by fellow researchers. In the case of SPOM/NSOM measurements, the typical approach was to measure intensity variations by collecting and averaging over the entire conical field. While this approach resulted in fairly good images, it overlooked a number of interesting details including ways to improve the image quality. Quite often this averaging process was prone to produced non-topographical artifacts in the scan images in the form of splotches (see for instance key 41). We found that the appearance of the splotches are consistent with averaging over the ensemble of primary stripes distributed around the cone ring. Once the splotches are embedded in

the image, they are difficult to remove through post-processing. We have found that a better method for improving SPOM/NSOM images involves attenuating the primary stripes at the discrete locations around the cone and then performing an average over these frames. Due to the periodicity of the primary stripes, Fourier filtering works very well.

We have also developed a working theory for the origin of the primary stripes as resulting from single scattering of the incident SPP field off of the probe tip interfering with the background field buried within the speckle. The buried background field, is the result of the phasor sum of radiated SPP which have scattering paths that did not involve the tip. Armed with this knowledge we can can use the presence of these stripes to our advantage. The orientation and spread of the stripes generated at a particular point on the cone ring allows us to determine the direction of propagation of a SPP field on the surface. The primary stripes are associated with the propagation of the launched SPPs where as the presence of secondary stripes in our data, which conform to the same analysis as the primaries, can be associated with a strong SPP reflection from features on the metal surface. We propose that the presence of these stripes can be further used for testing the efficiency of SPP mirrors and wave guides and is worth further pursuing.

We note in passing that the primary stripes can also be used for detecting locations of phase singularities within the speckle of the conical radiation without the use of an external reference field. Where as an external reference field will reveal optical vortices in the form of optical dislocations. The primary stripes will reveal them by shifting a full wavelength in position associated by a full 2π shift in phase as a path is traversed around a region containing a phase singularity.

While much of our attention is centered on the properties of the cone ring, we have also studied the region where the cone ring intersects the specularly reflected

beam from the sample. This lead us to investigate the finer points of SPP excitation and aspects of the specular reflected beam particularly the interference fringes that appear on the down stream side of the reflected profile. To our knowledge, we were the first to observe these interference fringes for short-range SPP. However, they were simultaneously observed for long-range SPP in four layer systems and long-range waveguide fields [80]. We have looked into using this extra information contained in the fringes for the possibility of improving on ATR based analyte detection, specifically, gas detection. We have done this by leaking freon-116 gas into the sample chamber (STM chamber) and observe the shift in the fringes. However, the shift in the ATR position was the same for all of the fringes so we were unable to develop a way to use this extra information for improving upon current ATR detection schemes.

We have also experimented with using the probe tip to weaken the contribution of the leaky wave of the SPPs in the specular beam by scattering the SPPs away from the downstream direction and thus, modifying the notch depth of the reflected beam. The field from the SPP is in antiphase with the specularly reflected beam from the front surface (glass/metal) resulting in a notch in the reflected beam profile corresponding to the SPP excitation angle. For a film thickness equal to the critical thickness, the notch depth is at a minimum resulting in the total attenuation of the specular beam (at the notch location). While varying the film thickness will change the contribution of the SPP leaky wave, the film thickness is a fixed property of the sample and can not be changed once the film has been deposited. The positioning the probe tip allows for in-situ control over the destructive interference in the specular beam.

One possible avenue of future work regarding this ability involves the analogy that can be drawn between this system and a Mach-Zehnder interferometer. Here, the first surface interface (glass/metal) splits the incoming beam into a reflected beam and a

propagating SPP field analogous with the splitting of an optical field by the first beam splitter of a Mach-Zehnder interferometer. The fields in the two paths are once again combined where one output arm results in total destructive interference (specular beam notch) and the other output arm results in total constructive interference (the conversion of SPP into heat). It is known that the probe tip can form a van der Waals trap for molecules [81] enabling one to position a molecule within one arm of the "interferometer", namely the SPP arm while simultaneously creating total destructive interference in the notch.

Much of our studies involved understanding the properties of photometry space and how it relates to the radiated conical field and the behavior of the SPPs and probe tip at the metal surface. Besides the SPOM/NSOM images that appear in the photometry as the probe tip traverses the surface in tunneling contact, far more interesting properties occur when the probe tip is scanned above the surface out beyond tunneling distance (150 to 200nm or so), but still within the interaction range of the evanescent SPP field. We have discovered additional structure in the photometry images generated at certain fixed locations (dark regions near optical vortices) on the cone ring. Through computer simulation, we are able to relate this structure to single and multiple SPP scattering events involving the probe tip. This structure is distinctly different from the underlying topography of the surface as well as the SPP field distribution on the surface. One of the exciting results to come from this is the appearance, under certain conditions, of phase singularities in the photometry maps. Detecting phase singularities in the photometry space suggests that we are able to manipulate the phase at a point in the far-field on the cone ring by interacting with the SPPs with the probe tip in the near field. This includes advancing (or retreating) through an arbitrary amount of phase out at a given location on the cone ring. We have found that photometry maps generated at different locations on

the cone ring will have different arrangements of phase singularities. In other words, depending on the trajectory of the tip, it is possible to create arbitrary phase shifts at select positions on the cone ring. We have not yet determined what this may ultimately be good for, but it is topologically interesting. We also note that this phase variation is a robust feature of the field.

Apart from the optical vortices that appear in our (simulated) photometry maps, we have also studied the real-space optical vortices that appear within the cone ring speckle. We have demonstrated the ability to shift the position of these vortices (with limited control) by moving the probe tip. The shift in position of the vortices occur from the interference with the field originating from the probe tip sampling the local field on the metal surface. This field is largely predictable since it is dominated by the phase of the launched SPPs. This technique also allows us to create and annihilate oppositely charged pairs of vortices within the cone speckle.

One important aspect that deserves further study involves SPP vortices located at the metal surface. The prospect of harnessing the angular momentum of the SPP vortices for useful work at the micro-scale is very intriguing. Our preliminary simulations show that the probe tip is capable of positioning vortices on the surface by manipulating one of the three beams for interference. Driving micro-machines in this fashion could allow for the eventual fusion of electronics, photonics, plasmonics, and kinematics.

APPENDIX

MONTE CARLO SPP SCATTERING SIMULATION PROGRAM

```
/*****************************************************************/
/* c Routine for use with Mathematica front end and MathLink     */
/*                                                               */
/* This program performs a Monte Carlo simmulation of SPP        */
/* scattering from a raster scanned probe tip and point          */
/* scatterers chosen by the user. For each tip position, the     */
/* complex phase resulting from the summation of random scattering */
/* paths is calculated for a single position in the far-field    */
/* (out in the cone ring.)                                       */
/* This program returns a 14X128X129 array consisting of the real */
/* and imaginary part of the amplitude for 7 distinct types of   */
/* scattering paths on a 128X128 Photometry map with the 129th   */
/* array element reserved for path status.                       */
/*                                                               */
/* Software writen by Robert Schumann and Stephen Gregory        */
/*****************************************************************/

:Begin:
:Function:       cone
:Pattern:        Cone[phasepref_Real, xscatt_List, yscatt_List, expo_List,
                 thetacone_Real, thetaplasmon_Real, spotsize_Integer]
:Arguments:      {phasepref, xscatt, yscatt, expo,
                 thetacone, thetaplasmon, spotsize}
:ArgumentTypes: {Real, RealList, RealList, RealList, Real,
                 Real, Integer}
:ReturnType:     Manual
:End:

/* phase prefactor, x coords for scatterers, y coords for        */
/* scatterers, and angle thetacone counter clock wise from -x axis */
```

```
int main(int argc, char* argv[]) {
return MLMain(argc, argv);
}
#include <stdlib.h>
#include <stdio.h>
#include <time.h>
#include <math.h>

/*************** CONDITIONAL COMPILATION FLAGS ********************/

/******************************************************************/

#define NUMSCANPOINTS 128 /* sets size of probe tip scan          */

/* Period parameters for Mersenne Twister                          */

#define N 624
#define M 397
#define MATRIX_A 0x9908b0dfUL   /* constant vector a               */
#define UPPER_MASK 0x80000000UL /* most significant w-r bits       */
#define LOWER_MASK 0x7fffffffUL /* least significant r bits        */

/******************** GLOBAL VARIABLES ****************************/

double lifeleft;
double a_ellipse, b_ellipse;
double *xscatt, *yscatt;
long numscatt;
int *path_track;

/* for use by Mersenne Twister                                     */
unsigned long mt[N]; /* the array for the state vector           */
int mti=N+1; /* mti==N+1 means mt[N] is not initialized           */

double sumsc[14][NUMSCANPOINTS][NUMSCANPOINTS+1];

/* [0] cosinesum multiple scattering,                              */
/* [1] sinesum multiple scattering,                                */
/* [2] cosinesum single scattering off of the tip,                 */
/* [3] sinesum single scattering off of the tip                    */

int scanxindex,scanyindex;
```

```
/* Scan matrix x-y indices - must be positive -                    */
/* they are NOT tip position coordinates                           */

/************* FUNCTION PROTOTYPES *********************************/

double mt_rand(void);
void init_genrand(unsigned long);
int possible_initials(int *);
int choose_initialscatt(int *, int, int);
int choose_nextscatt(int, double);
void reject_time_reverse_paths(int);
void write_path_track_file(int);
void weight_path(int, int);
void eliminate_single_scattering_off_tip(int);
void exclude_tipless_paths(int);
void add_reference_beam(double, double, int, int, int, int);
/* acts as constant reference or vortex hunter                     */
void exclude_double_scatt_with_tip(int);

/********************** CALLED FUNCTION ****************************/

void cone
(
double phasepref,     /* multiplier for pathlength to convert      */
/*                       to phase                                  */

double *xscatt_tmp,   /* pointer to array of x coords of scatterers */

long  numscatt_tmp ,  /* this is the size of the xscatt array      */
/*                       which is also the number of scatterers    */

double *yscatt_tmp,   /* pointer to array of y coords of scatterers */
long ysize,           /* just here as a dummy                      */
double *expo,
long numpaths,        /* let the length of expo determine number   */
/*                       of paths                                  */

double thetacone,     /* thetacone is scattering angle measured    */
/*                       counter-clockwise from -x axis            */

double thetaplasmon, /* thetaplasmon is plasmon launch angle       */
```

```
/*                          measured from the normal                    */

int spotsize
)
/******* LOCAL VARIABLES ****************************************/
{
int i, initialscatt, nextscatt, previous_scatt, path_index, j;
int scatt_total, n, tip, single_scatt_off_tip;
int closed_path_tip_first_last;
int first_scatterer_is_tip, last_scatterer_is_tip, path_no_tip;
int closed_path_tip_involved, path_include_tip;
double xprevious, yprevious, xnext, ynext, plasmonbirth, count;
long dims[] = {14, NUMSCANPOINTS, NUMSCANPOINTS+1};
int poss_initials[1000];
int  numinitials; /* number of possible initialscatts */
double pathlength, phase_tmp;
int xtip, ytip; /* tip position */

/*************************************************************************/

/* The following assigns the values passed in from mathematica      */
/* to variables that we have declared to be global.                 */
xscatt = xscatt_tmp; yscatt = yscatt_tmp;
numscatt = numscatt_tmp;
single_scatt_off_tip = 0;
closed_path_tip_first_last = 2;
first_scatterer_is_tip = 4;
last_scatterer_is_tip = 6;
closed_path_tip_involved = 8;
path_include_tip = 10;
path_no_tip = 12;
count = (double)1.0/(NUMSCANPOINTS*NUMSCANPOINTS);

/* memory is allocated for path_track. path_track is a numpath      */
/* by 100 array the first 95 slots of each 100 slot block is used   */
/* to store the index of the scatterers visited, the last 5 slots   */
/* of each 100 slot block is used to store additional information   */
/* about the path such as the number of scatterers visited.         */

path_track = (int *)malloc((int)numpaths * 100 * (int) sizeof(int));
if(path_track == 0){
printf ("error allocating memory for path_track\n");}
```

```
/* formating of path_track is as follows...                    */
/* 0-94 storage of scatterer indices for current path          */
/* 95 plasmon birth for current path                           */
/* 96 lifeleft for current path                                */
/* 97 weighting factor for current path                        */
/* 98 sum inclusion flag for current path                      */
/* 99 number of scatterers visited in current path             */
/* note: path_track contains only integer values.              */

/*************************************************************/

/* seed random number generator                                */
init_genrand((unsigned long)time(NULL));

b_ellipse = (double)(spotsize/2);
a_ellipse = (double)spotsize/(2*sin(thetaplasmon));
/* This ensures that the tip will be considered               */
/* as one of the first scatterers.                            */
xscatt[0] = 0; yscatt[0] = 0;
numinitials = possible_initials(poss_initials);

/*************************************************************/

/* this code initializes stats about the paths that           */
/* will be returned to the mathematica program.               */

for(j = 0; j <= 13; j++){
for(i = 0; i <= 94; i++)
{sumsc[j][i][NUMSCANPOINTS] = 0.0;}
}
/************ x-y tip position loops ***************************/

for(scanxindex = 0; scanxindex < NUMSCANPOINTS; scanxindex++)
{
for(scanyindex = 0; scanyindex < NUMSCANPOINTS; scanyindex++)
{
/* initialize cosinesum and sinesum                           */
sumsc[single_scatt_off_tip][scanyindex][scanxindex] = 0.0;
sumsc[single_scatt_off_tip + 1][scanyindex][scanxindex] = 0.0;

sumsc[closed_path_tip_first_last][scanyindex][scanxindex] = 0.0;
```

```
sumsc[closed_path_tip_first_last + 1][scanyindex][scanxindex] = 0.0;

sumsc[first_scatterer_is_tip][scanyindex][scanxindex] = 0.0;
sumsc[first_scatterer_is_tip + 1][scanyindex][scanxindex] = 0.0;

sumsc[last_scatterer_is_tip][scanyindex][scanxindex] = 0.0;
sumsc[last_scatterer_is_tip + 1][scanyindex][scanxindex] = 0.0;

sumsc[closed_path_tip_involved][scanyindex][scanxindex] = 0.0;
sumsc[closed_path_tip_involved + 1][scanyindex][scanxindex] = 0.0;

sumsc[path_include_tip][scanyindex][scanxindex] = 0.0;
sumsc[path_include_tip + 1][scanyindex][scanxindex] = 0.0;

sumsc[path_no_tip][scanyindex][scanxindex] = 0.0;
sumsc[path_no_tip + 1][scanyindex][scanxindex] = 0.0;

/* set xscatt[0] and yscatt[0]to tip position, which is          */
/* relative to the origin on surface.                            */
xscatt[0] = (double)(scanxindex - NUMSCANPOINTS/2);
yscatt[0] = (double)(scanyindex - NUMSCANPOINTS/2);

/* Execute scattering path - repeat (numpaths) times             */
for(i=0; i < (int)numpaths; i++){
/* set path index to zero for use in path_track                  */
path_index = 0;
/* initialises inclusion flag for current path (1 = include)     */
path_track[i*100 + 98] = 1;

/* select a lifeleft (lifelength left - starts out as full       */
/* length) from the expo list                                    */
lifeleft = expo[i];
/* choose initialscatt.                                          */
initialscatt = choose_initialscatt(poss_initials, numinitials, i);
pathlength = xscatt[initialscatt]; /* 1st segment of pathlength  */
xprevious = xscatt[initialscatt];
yprevious = yscatt[initialscatt];
nextscatt = initialscatt;
path_track[i*100 + path_index] = initialscatt;
/* record the first scatterer                                    */
path_index++;
```

```
/*****************************************************************/

do{
/* generate a random path between the first and last             */
/* scatterer and keep a running total of the pathlength.         */

previous_scatt = nextscatt;
nextscatt = choose_nextscatt(previous_scatt, 0);

if(previous_scatt != nextscatt){
/* this if statement keeps track of i'th path                    */

path_track[i*100 + path_index] = nextscatt;
path_index++;
if(path_index > 94){path_index = 94;}
/* test to see if path_index over runs                           */
/* the memory allocated to path_track                            */
}
xnext = xscatt[nextscatt];
ynext = yscatt[nextscatt];

pathlength += sqrt((xnext - xprevious) * (xnext - xprevious)
              + (ynext - yprevious) * (ynext - yprevious));

xprevious = xnext; /* set for next iteration */
yprevious = ynext; /* set for next iteration */
}
while(nextscatt != previous_scatt);
/* if next scatt = previous scatt then let                       */
/* plasmon decay from previous scatterer.                        */

path_track[i*100 + 96] = (int)lifeleft;
/* The 99'th slot of each 100 slot block is reserved for         */
/* the storage of the number of scatterers visited.              */
path_track[i*100 + 99] = path_index;

if(path_index == 94){path_track[i*100 + 98] = 0;}
/* flags path to be disqualified from sum if too many            */
/* scatterers are included. This will probably never happen      */

/*****************************************************************/
```

```
/******** filters for inclusion / exclusion are listed here ********/

/* These filters are obsolete so they are commented out              */
/*
if(options[0]){ /* exclude time reverse paths                       */
reject_time_reverse_paths(i);}
if(options[1] != 10){
/* weight current path. note: the weight is contained in options[1] */
weight_path(i, options[1]);}
if(options[2]){  /* eliminates single scattering off tip           */
eliminate_single_scattering_off_tip(i);}
if(options[3]){
exclude_tipless_paths(i);}
*/
/******************** end filters ********************************/

if(path_track[i*100 + 98]){
/* if true then include path in sum                                 */

phase_tmp = phasepref * (pathlength + xnext * cos(thetacone)
                + ynext * sin(thetacone));
scatt_total = path_track[i*100 + 99];
/* 1. Check to see if the first scatterer is the tip                */
if(path_track[i*100] == 0)
{/* 1.Yes. */
/* 2. Now is it the only scatterer?                                 */
if(scatt_total == 1){
/* 2. Yes.                                                          */
sumsc[single_scatt_off_tip][scanyindex][scanxindex]
                += cos(phase_tmp);
sumsc[single_scatt_off_tip + 1][scanyindex][scanxindex]
                += sin(phase_tmp);
sumsc[single_scatt_off_tip + 1][scatt_total -1][NUMSCANPOINTS]
                += count;
} /* end of 2. Yes */
else{ /* 2. No. */
/* 3. Is the last scatterer also the tip?                           */
if(path_track[i*100 + (scatt_total -1)] == 0){
/* 3. Yes.                                                          */
sumsc[closed_path_tip_first_last][scanyindex][scanxindex]
                += cos(phase_tmp);
sumsc[closed_path_tip_first_last + 1][scanyindex][scanxindex]
```

```
                += sin(phase_tmp);
sumsc[closed_path_tip_first_last + 1][scatt_total -1][NUMSCANPOINTS]
                += count;
} /* end of 3. Yes */
else{
/* 3. No. Then this path has the tip as the first scatterer.        */
sumsc[first_scatterer_is_tip][scanyindex][scanxindex]
                += cos(phase_tmp);
sumsc[first_scatterer_is_tip + 1][scanyindex][scanxindex]
                += sin(phase_tmp);
sumsc[first_scatterer_is_tip + 1][scatt_total -1][NUMSCANPOINTS]
                += count;
} /* end of 3. No */
} /* end of 2. No */
} /* end of 1. Yes */
else{
/* 1. No, the first scatterer was not the tip.                      */
/* 4. Is the last scatterer the tip?                                */
if(path_track[i*100 + (scatt_total -1)] == 0){
/* 4. Yes                                                           */
sumsc[last_scatterer_is_tip][scanyindex][scanxindex]
                += cos(phase_tmp);
sumsc[last_scatterer_is_tip + 1][scanyindex][scanxindex]
                += sin(phase_tmp);
sumsc[last_scatterer_is_tip + 1][scatt_total -1][NUMSCANPOINTS]
                += count;
} /* end of 4. Yes */
else
{ /* 4. No */
/* Determine if this path contains the tip                          */
tip = 0;
if(scatt_total >= 3){
/* the first and second scatterer is not the tip                    */
n = 1;
do{
if(path_track[i*100 + n] == 0){
tip = 1;
}
n++;
}
while(!((tip == 1 ) || (n == (scatt_total -1))));
}
```

```
/*****************************************************************/

/* 5. Are any of the other scatterers the tip?                    */
if(tip){
/* 5. Yes this path contains the tip.                             */
/* 6. Is this path closed?                                        */
if(path_track[i*100] == path_track[i*100 + (scatt_total -1)]){
/* 6. Yes, this path is closed                                    */
sumsc[closed_path_tip_involved][scanyindex][scanxindex]
                += cos(phase_tmp);
sumsc[closed_path_tip_involved + 1][scanyindex][scanxindex]
                += sin(phase_tmp);
sumsc[closed_path_tip_involved + 1][scatt_total -1][NUMSCANPOINTS]
                += count;
} /* end of 6. Yes                                                */
else{
/* 6. No, this is just a path that includes the tip               */
sumsc[path_include_tip][scanyindex][scanxindex]
                += cos(phase_tmp);
sumsc[path_include_tip + 1][scanyindex][scanxindex]
                += sin(phase_tmp);
sumsc[path_include_tip + 1][scatt_total -1][NUMSCANPOINTS]
                += count;
} /* end of 6. No.                                                */
} /* end of 5. Yes */
else{
/* 5. No this path does not contain the tip at all.               */
sumsc[path_no_tip][scanyindex][scanxindex]
                += cos(phase_tmp);
sumsc[path_no_tip + 1][scanyindex][scanxindex]
                += sin(phase_tmp);
sumsc[path_no_tip + 1][scatt_total -1][NUMSCANPOINTS]
                += count;
} /* end of 5. No. */
} /* end of 4. No */
} /* end of 1. No. */
} /* end of if path_track */
} /* end of numpaths loop */
/***** optional addition of a reference or vortex hunter "beam" *****/
/* this is more obsolete code that is commented out               */
/*
if(options[4]){/* if non-zero (amplitude) then add beam          */
```

```
add_reference_beam(xtip, ytip, options[4], options[5],
        options[6], options[7]);}
*/
/*****************************************************************/

} /* end scanyindex loop                                          */
} /* end scanxindex loop                                          */

MLPutRealArray(stdlink, &sumsc[0][0][0], dims, NULL, 3);
} /* end of cone */

/*****************************************************************/

/* These functions seed and generate Mersenne Twister             */
/* random numbers                                                 */
/* [0,1). This is the preferred random number generator for       */
/* Monte Carlo Simulations.                                       */
/* initializes mt[N] with a seed                                  */
void init_genrand(unsigned long s)
{
mt[0]= s & 0xffffffffUL;
for (mti=1; mti<N; mti++) {
mt[mti] =
(1812433253UL * (mt[mti-1] ^ (mt[mti-1] >> 30)) + mti);
mt[mti] &= 0xffffffffUL;
}
}
/* generates Mersenne Twister random double [0,1)                 */
double mt_rand(void)
{
unsigned long y;
static unsigned long mag01[2]={0x0UL, MATRIX_A};
/* mag01[x] = x * MATRIX_A  for x=0,1                             */
if (mti >= N) { /* generate N words at one time */
int kk;
if (mti == N+1)   /* if init_genrand() has not been called, */
init_genrand(5489UL); /* a default initial seed is used */
for (kk=0;kk<N-M;kk++) {
y = (mt[kk]&UPPER_MASK)|(mt[kk+1]&LOWER_MASK);
mt[kk] = mt[kk+M] ^ (y >> 1) ^ mag01[y & 0x1UL];
}
for (;kk<N-1;kk++) {
```

```
y = (mt[kk]&UPPER_MASK)|(mt[kk+1]&LOWER_MASK);
mt[kk] = mt[kk+(M-N)] ^ (y >> 1) ^ mag01[y & 0x1UL];
}
y = (mt[N-1]&UPPER_MASK)|(mt[0]&LOWER_MASK);
mt[N-1] = mt[M-1] ^ (y >> 1) ^ mag01[y & 0x1UL];
mti = 0;
}
y = mt[mti++];
y ^= (y >> 11);
y ^= (y << 7) & 0x9d2c5680UL;
y ^= (y << 15) & 0xefc60000UL;
y ^= (y >> 18);
return (((double)y) / 4294967296.0);
}
/*****************************************************************/

int possible_initials( int *poss_initials)
/* Determines which scatterers fall within the launch ellipse     */
/* or anywhere to the +x side of it (i.e. downstream)             */
/* returns: numinitials (number of possible initial scatterers)   */
{
int i, j=0;
for(i=0; i < numscatt; i++){
if(fabs(yscatt[i]) < b_ellipse){
if(xscatt[i] > -(a_ellipse/b_ellipse) *
                sqrt(b_ellipse * b_ellipse - yscatt[i] * yscatt[i]))
{
*(poss_initials + j) = i; /*this one is possible*/
j++;
}/* end if(fabs (xscatt[i])  */
}/* end if(fabs(yscatt[i]) < b_ellipse) */
}/* end for */
return j; /* number of initial scatterers */
}/* end of possible_initials */

/*****************************************************************/

int choose_initialscatt(int *poss_initials,
                int numinitials, int current_path)
/* Chooses the initial scatterer for a particular path.           */
/* pointer returns:  amount of lifelength left                    */
/* call return: index of scatterer                                */
```

```
{
int initialscatt;
double plasmonbirth;
do{
/* randomly select one of the poss_initials                          */
initialscatt = poss_initials[(int)(((double)numinitials) *
               mt_rand())];
/* randomly select plasmon launch position inside ellipse            */
/* ( at y coord of the scatterer )                                   */

plasmonbirth = ( 2.0 * mt_rand()  - 1.0) *
               (a_ellipse/b_ellipse) * sqrt(b_ellipse *
               b_ellipse - yscatt[initialscatt] * yscatt[initialscatt]);
}
while(((xscatt[initialscatt] - plasmonbirth) < 0.0) ||
               ((xscatt[initialscatt] - plasmonbirth) > lifeleft));
/* launch must be upstream and within lifeleft                       */

lifeleft -= ( xscatt[initialscatt] - plasmonbirth );
/* remaining lifelength for rest of path                             */

path_track[current_path*100 + 95] = (int)plasmonbirth;
/* keep track of plasmon births                                      */
return initialscatt;
}

/*****************************************************************/

int choose_nextscatt(int current_scatt, double include_region){
int *possible_scatterers;
int j, k = 0;
double length, include_region_tmp;
possible_scatterers = (int *)malloc((int)numscatt *
               (int) sizeof(int));
if(possible_scatterers == 0){
printf ("error allocating memory in choose_nextscatt\n");
}/* end error check */
if((include_region) && (include_region < lifeleft)){
        include_region_tmp = include_region;}
else{
include_region_tmp = lifeleft;}
for(j=0; j < numscatt; j++){
```

```
length = sqrt( (xscatt[current_scatt] - xscatt[j]) *
               (xscatt[current_scatt] - xscatt[j]) +
               (yscatt[current_scatt] - yscatt[j]) *
               (yscatt[current_scatt] - yscatt[j]) );

if(include_region_tmp > length){
possible_scatterers[k] = j;
k+=1;
}/* end if lifeleft */
}/* end for j */
j = (int)(((double)k) * mt_rand());
/* j used to store the index for next scatterer                    */
/* from list of possible next scatterers                           */
k = possible_scatterers[j];
/* actual index of next scatterer is extracted                     */
free(possible_scatterers);

/* make adjustments to lifeleft                                    */
lifeleft -= sqrt( (xscatt[current_scatt] -
               xscatt[k]) * (xscatt[current_scatt] -
               xscatt[k]) + (yscatt[current_scatt] -
               yscatt[k]) * (yscatt[current_scatt] - yscatt[k]) );
return k;
}
/*****************************************************************/

void reject_time_reverse_paths(int current_path){
/* This code takes the current path and checks it against          */
/* all previous paths. If time reversal is discovered,             */
/* then the current path is disqualified.                          */

int j, k, compare = 0, scatt_number;
scatt_number = path_track[current_path*100 + 99];

if((scatt_number > 1) &&
               (path_track[current_path*100+scatt_number-1] == 0)){
/* Check to see if the current path contains more than one         */
/* scatterer, and also, that the last scatterer is the tip.        */
/* Then continue checking for time reverse paths                   */

for(j=0; j < current_path; j++){
if((path_track[j*100 + 99] == scatt_number) &&
```

```
                (path_track[j*100+scatt_number-1] == 0)){
for(k=0; k < scatt_number-1; k++){
/* The k loop checks two different paths of the same size          */
/* in reverse order by calculating their difference and            */
/* storing that value in compare                                   */
compare += (int)fabs(path_track[j * 100 +
                scatt_number - 2 - k] -
                path_track[current_path * 100 + k]);
/* find the difference in paths                                    */
} /* end of k loop. */
if(compare == 0){
/* if true, then this is a time reverse path, so disqualify it     */
path_track[current_path * 100 + 98] = 0;
/* This flags the current path to be disqualified from the sum     */
}/*  end if compare  */
}/*  end if path_track  */
}/*  end of j loop  */
}/*  end if scatt_number  */
}/*  end of program  */

/*********************************************************************/

void write_path_track_file(int numpaths){
int i;
FILE *path_dat_file;
path_dat_file = fopen("pathdata.dat","w");
for(i=0; i < (numpaths * 100); i++){
fprintf(path_dat_file,"%d\n",path_track[i]);
}
fclose(path_dat_file);
}

/*********************************************************************/

void weight_path(int current_path, int weight_factor){

/* this function checks to see how many times the tip is visited in */
/* a single path and weights the coefficient to sinesum and
/* cosinesum.                                                      */
/* path_track[... + 97] is reserved for the coefficient            */

int i, scatt_number, tip_count = 0;
```

```
scatt_number = path_track[current_path * 100 + 99];
/* set number of scatterers in the current path                    */
for(i=0; i < scatt_number; i++){
if(path_track[current_path*100 + i] == 0){
tip_count++;}/* end if */
}/* end for loop */
if(tip_count != 0){
path_track[current_path * 100 + 97] = tip_count * weight_factor;
}
/* if the tip is involved then adjust the                          */
/* sinesum and cosinesum appropriately                             */
} /* end of weight_path function                                   */

/*****************************************************************/

void eliminate_single_scattering_off_tip(int current_path){

if((path_track[current_path * 100] == 0)
              && (path_track[current_path * 100 + 99] == 1)){
/* if only scatterer is the tip                                    */
path_track[current_path * 100 + 98] = 0;}
/* set flag to elliminate this path from sum                       */
}/* end of this measly function */

/*****************************************************************/

void exclude_tipless_paths(int current_path){
int i;
path_track[current_path*100 + 98] = 0; /* initially exclude path   */
for(i=0; i<path_track[current_path * 100 + 99]; i++){
if(path_track[current_path * 100 + i] == 0){
path_track[current_path * 100 + 98] = 1;}
/* include path in sum if tip is present                           */
}/* end for loop */
}
/*****************************************************************/

void add_reference_beam(double xtip, double ytip,
       int amplitude, int phase_offset , int spatial_freq, int angle){
double phase_at_tip;
phase_at_tip =((ytip * sin ((M_PI/180.0) * (double)angle) +
                xtip * cos ((M_PI/180.0) * (double)angle)) *
```

```
                spatial_freq + (M_PI/180.0) * (double)phase_offset);
sumsc[0][scanyindex][scanxindex] +=
                (double)amplitude * cos(phase_at_tip);
sumsc[1][scanyindex][scanxindex] +=
                (double)amplitude * sin(phase_at_tip);
}
/*****************************************************************/

void exclude_double_scatt_with_tip(int current_path){
/* this code checks two things, first,                           */
/* if path contains only two scatterers                          */
/* and if either the first or second scatterer is the tip        */
if((path_track[current_path * 100 + 99] == 2) &&
                ((path_track[current_path * 100] == 0) ||
                (path_track[current_path * 100 + 1] == 0))){
path_track[current_path * 100 + 98] = 0;}
/* exclude this path from sum                                    */
}
/*****************************************************************/
```

BIBLIOGRAPHY

[1] R. H. Ritchie, "Plasma Losses by Fast Electrons in Thin Films," Phys. Rev. **106**, 874-881 (1957).

[2] R. W. Wood, "On a Remarkable Case of Uneven Distribution of Light in a Diffraction Grating Spectrum," Proc. Phys. Soc. London **18**, 269-275 (1902).

[3] U. Fano, "The Theory of Anomalous Diffraction Gratings and of Quasi-Stationary Waves on Metallic Surfaces (Sommerfeld's Waves)," J. Opt. Soc. Am. **31**, 213-222 (1941).

[4] R. H. Ritchie, E. T. Arakawa, J. J. Cowan and R. N. Hamm, "Surface-Plasmon Resonance Effect in Grating Diffraction," Phys. Rev. Lett. **21**, 1530-1533 (1968).

[5] G. Mie, "Beiträge zur Optik trüber Medien, speziell kolloidaler Metallösungen," Ann. Phys. **25**, 377-452 (1908).

[6] U. Kreibig and P. Zacharias, "Surface plasma resonances in small spherical silver and gold particles," Z. Physik **231**, 128-143 (1970).

[7] A. Otto, "Excitation of Nonradiative Surface Plasma Waves in Silver by the Method of Frustrated Total Reflection," Z. Physik **216**, 398-410 (1968).

[8] E. Kretschmann and H. Raether, "Radiative decay of nonradiative surface plasmon excited by light," Z. Nature **23A**, 2135-2136 (1968).

[9] M. Fleischmann, P. J. Hendra and A. J. McQuillan, "Raman spectra of pyridine adsorbed at a silver electrode," Chem. Phys. Lett. **26**, 163-166 (1974).

[10] D. L. Jeanmaire and R. P. van Duyne, "Surface Raman Electrochemistry Part 1. Heterocyclic, Aromatic and Aliphatic Amines Adsorbed on the Anodized Silver Electrode," J. Elec. Chem. **84**, 1-20 (1977).

[11] D. W. Pohl, W. Denk and M. Lanz, "Optical stethoscopy: Image recording with resolution $\lambda/20$," Appl. Phys. Lett. **44**, 651-653 (1984).

[12] A. Lewis, M. Isaacson, A. Harootunian and A. Murray, "Development of a 500 Å spatial resolution light microscope. 1. Light is efficiently transmitted through $\lambda/16$ diameter apertures," Ultramicroscopy **13**, 227-232 (1984).

[13] E. H. Synge, "A suggested method for extending the microscopic resolution into the ultramicroscopic region," Phil. Mag. **6**, 356-362 (1928).

[14] M. Specht, J. D. Pedarnig, W. M. Heckl, and T. W. Hänsch, "Scanning Plasmon Near-Field Microscope," Phys. Rev. Lett. **68**, 476-479 (1992).

[15] T. W. Ebbesen, H. J. Lezec, H. F. Ghaemi, T. Thio and P. A. Wolff, "Extraordinary optical transmission through sub-wavelength hold arrays," Nature **391**, 667-669 (1998).

[16] K. Kneipp, Y. Wang, H. Kneipp, L. T. Perelman, I. Itzkan, R. R. Dasari and M. S. Feld, "Single Molecule Detection Using Surface-Enhanced Raman Scattering (SERS)," Phys. Rev. Lett. **78**, 1667-1670 (1997).

[17] C. J. Powell and J. B. Swan, "Effect of Oxidation on the Characteristic Loss Spectra of Aluminum and Magnesium," Phys. Rev. **118**, 640-643 (1960).

[18] N. Garcia and M. Bai, "Theory of Transmission of Light by Sub-Wavelength Cylindrical Holes in Metallic Films," Opt. Exp. **14**, 10028-10042 (2006).

[19] F. Abeles, "Surface Plasmon (SEW) Phenomena," in *Electromagnetic Surface Excitations*, R. F. Wallis and G. I. Stegeman, eds. (Springer-Verlag, New York, 1986), pp. 8-29.

[20] L. Novotny and B. Hecht, *Principles of Nano-Optics* (Cambridge University Press, United Kingdom, 2006).

[21] F. Baida, D. V. Labeke and J. M. Vigoureux, "Theoretical study of near-field surface plasmon excitation, propagation and diffraction," Opt. Comm. **171**, 317-331 (1999).

[22] S. Kawata, *Near-Field Optics and Surface Plasmon Polaritons* (Springer Verlag, Berlin, Heidelberg, 2001).

[23] J. D. Jackson, *Classical Electrodynamics third edition* (John Wiley & Sons, New York, 1999).

[24] Y. Kuk, "STM on Metals," *Scanning Tunneling Microscopy I*, H. J. Guntherodt and R. Wiesendanger, eds. (Springer Verlag, Heidelberg, 1992), pp. 17-35.

[25] A. Bryant, D. P. E. Smith, and C. F. Quate, "Imaging in real time with the tunneling microscope," Appl. Phys. Lett. **48**, 832-834 (1986).

[26] David W. Abraham, C. C. Williams, and H. K. Wickramasinghe, "Noise reduction technique for scanning tunneling microscopy," Appl. Phys. Lett. **53**, 1503-1505 (1988).

[27] C. J. Chen, *Introduction to Scanning Tunneling Microscopy Second Edition* (Oxford University Press, 2008).

[28] R. Hobara, S. Yoshimoto and S. Hasegawa, "Dynamic electrochemical-etching technique for tungsten tips suitable for multi-tip scanning tunneling microscopes," e-J. Surf. Sci. Nanotech **5,** 94-98 (2007).

[29] P. E. Wolf and G. Maret, "Weak Localization and Coherent Backscattering of Photons in Disordered Media," Phys. Rev. Lett. **55**, 2696-2699 (1985).

[30] G. Bergmann, "Physical interpretation of weak localization: A time-of-flight experiment with conduction electrons," Phys. Rev. B **28**, 2914-2920 (1983).

[31] E. Abrahams, P. W. Anderson, D.C. Licciardello and T. V. Ramakrishnan, "Scaling Theory of Localization: Absence of Quantum Diffusion in Two Dimensions," Phys. Rev. Lett. **42**, 673-675 (1979).

[32] Y. Wang and H. J. Simon, "Coherent backscattering of optical second-harmonic generation in silver films," Phys. Rev. B **47**, 13695-13699 (1993).

[33] W. Wang, M. J. Feldstein, N. F. Scherer, "Observation of coherent multiple scattering of surface plasmon polaritons on Ag and Au surfaces," Chem. Phys. Lett. **262**, 573-582 (1996).

[34] E. Akkermans, P. E. Wolf and R. Maynard, "Coherent Backscattering of Light by Disordered Media: Analysis of the Peak Line Shape," Phys. Rev. Lett. **56**, 1471-1474 (1986).

[35] V. Sivel, R. Coratger, F. Ajustron, and J. Beauvillain, "Photon emission stimulated by scanning tunneling microscopy in air," Phys. Rev. B **45**, 8634-8637 (1992).

[36] H. Raether, *Surface Plasmons on Smooth and Rough Surfaces and on Gratings*, Springer Tracts in Modern Physics Vol.III (Springer, Berlin, Heidelberg 1988).

[37] B. Saleh and M. Teich, *Fundamentals of Photonics* (John Wiley & Sons, New York, 1991).

[38] D. W. Pohl, W. Denk, and M. Lanz, "Optical stethoscopy: Image recording with resolution $\lambda/20$," Appl. Phys. Lett. **44**, 651-653 (1984).

[39] M. Specht, J. D. Pedarnig, W. M. Heckl, and T. W. Hansch, "Scanning Plasmon Near-Field Microscope," Phys. Rev. Lett. **68**, 476-479 (1992).

[40] B. Hecht, H. Bielefeldt, Y. Inouye, and D. W. Pohl, "Facts and artifacts in near-field optical microscopy," Jour. Appl. Phys. **81**, 2492-2498 (1997).

[41] H. F. Hamann, A. Gallagher, and D. J. Nesbitt, "Enhanced sensitivity near-field scanning optical microscopy at high spatial resolutions," App. Phys. Lett. **73**, 1469-1471 (1998).

[42] Y-K. Kim, P. R. Auvil, and J. B. Ketterson, "Conical electromagnetic radiation in the Kretschmann attenuated total reflections configuration," Appl. Opt. **36**, 841-846 (1997).

[43] Y-K. Kim, P. M. Lundquist, J. A. Helfrich, J. M. Mikrut, G. K. Wong, P. R. Auvil, and J. B. Ketterson, "Scanning plasmon optical microscope," Appl. Phys. Lett. **66**, 3407-3409 (1995).

[44] R. W. Rendell, D. J. Scalapino, and B. Muhlschlegel, "Role of Local Plasmon Modes in Light Emission from Small-Particle Tunnel Junctions," Phys. Rev. Lett. **41**, 1746-1750 (1978).

[45] E. Kretschmann and H. Raether, "Radiative decay of non-radiative surface plasmons excited by light," Z. Naturforsch **23**, 2135-2136 (1963).

[46] B. Dhanasekar, N. Krishna Mohan, B. Bhaduri and B. Ramamoorthy, "Evaluation of surface roughness based on momochromatic speckle correlation using image processing," Prec. Eng. **32**, 196-206 (2008).

[47] C. T. Stansberg, "Surface Roughness Dependence of the First-order Statistics of Polychromatic Speckle Patterns," Jour. Mod. Opt. **28**, 471-488 (1981).

[48] A. R. McGurn, T. A. Leskova and V. M. Agranovich, "Weak-localization effects in the generation of second harmonics of light at a randomly rough vacuum-metal grating," Phys. Rev. B **44**, 11441-11456 (1991).

[49] S. I. Bozhevolnyi, V. S. Volkov and K. Leosson, "Localization and Waveguiding of Surface Plasmon Plolaritons in Random Nanostructures," Phys. Rev. Lett. **89**, 186801-186804 (2002).

[50] S. I. Bozhevolnyi, "Localization phenomena in elastic surface-polariton scattering caused by surface roughness," Phys. Rev. B **54**, 8177-8185 (1996).

[51] J. C. Dainty, *Laser speckle and related phenomena* (Berlin, New York, Springer-Verlag, 1975).

[52] A. J. Braundmeier Jr. and H. E. Tomaschke, "Observation of the simultaneous emission of roughness-coupled and optical-coupled surface plasmon radiation from silver," Opt. Comm. **14**, 99-103 (1975).

[53] H. J. Simon and J. K. Guha, "Directional surface plasmon scattering from silver films," Opt. Comm. **18**, 391-394 (1976).

[54] F. T. Arecchi, G. Giacomelli, P. L. Ramazza, and S. Residori, "Vortices and defect statistics in two-dimensional optical chaos," Phys. Rev. Lett. **19**, 475-480 (1992).

[55] M. V. Berry, "Disruption of wavefronts: statistics of dislocations in incoherent Gaussian random waves," J. Phys. A **11**, 27-37 (1978).

[56] N. B. Baranova, A. V. Mamaev, N. F. Pilipetsky, V. V. Shkunov, and B. Y. Zel'dovich, "Wave-front dislocations: topological limitations for adaptive systems with phase conjugation," J. Opt. Soc. Am. **73**, 525-528 (1983).

[57] I. Freund, "'1001' correlations in random wave fields," Waves in Random Media **8**, 119-158 (1998).

[58] N. Shvartsman, I. Freund, "Vortices in Random Wave Fields: Nearest Neighbor Anticorrelations," Phys. Rev. Lett. **72**, 1008-1011 (1994).

[59] I. Freund, N. Shvartsman and V. Freilikher, "Optical dislocation networks in highly random media," Opt. Comm. **101**, 247-264 (1993).

[60] R. A. Beth, "Mechanical Detection and Measurement of the Angular Momentum of Light," Phys. Rev. **50**, 115-125 (1936).

[61] M. Mansuripur, "Angular momentum of circularly polarized light in dielectric media," Opt. Exp. **13**, 5315-5324 (2005).

[62] A. Mair, A. Vaziri, G. Weihs and A. Zeilinger, "Entanglement of the orbital angular momentum states of photons," Nature **412**, 313-316 (2001).

[63] J. H. Poynting, "The Wave Motion of a Revolving Shaft, and a Suggestion as to the Angular Momentum in a Beam of Circularly Polarised Light," Proc. R. Soc. London **82**, 560-567 (1909).

[64] M. E. J. Friese, J. Enger, H. Rubinsztein-Dunlop, and N. R. Heckenberg, "Optical angular-momentum transfer to trapped absorbing particles," Phys. Rev. A **54**, 1593-1596 (1996).

[65] N. B. Simpson, K. Dholakia, L. Allen, and M. J. Padgett, "Mechanical equivalence of Spin and orbital angular momentum of light: an optical spanner," Opt. Lett. **22**, 52-54 (1997).

[66] P. Galajda, and P. Ormos, "Complex micromachines produced and driven by light," Appl. Phys. Lett. **78**, 249-251 (2001).

[67] P. B. Johnson and R. W. Christy, "Optical Constants of the Noble Metals," Phys. Rev. B **6**, 4370-4379 (1972).

[68] M. A. Ordal, L. L. Long, R. J. Bell, S. E. Bell, R. R. Bell, R. W. Alexander, Jr., and C. A. Ward, "Optical properties of the metals Al, Co, Cu, Au, Fe, Pb, Ni, Pd, Pt, Ag, Ti, and W in the infrared and far infrared," Appl. Opt. **22**, 1099-1120 (1983).

[69] C. Nylander, B. Liedberg and T. Lind, "Gas detection by means of surface plasmon resonance," Sensors and Actuators **3**, 79-88 (1982).

[70] B. Liedberg, C. Nylander and I. Lundström, "Surface plasmon resonance for gas detection and biosensing," Sensors and Actuators, **4**, 299-304 (1983).

[71] K. Matsubara, S. Kawata and S. Minami, "Optical chemical sensor based on surface plasmon measurement," Appl. Opt. **27**, 1160-1163 (1988).

[72] B. Liedberg, I. Lundström and E. Stenberg, "Principles of biosensing with an extended coupling matrix and surface plasmon resonance," Sensors and Actuators B **11**, 63-72 (1993).

[73] J. Homola, S. S. Yee and G. Gauglitz, "Surface plasmon resonance sensors: review," Sensors and Actuators B **54**, 3-15 (1999).

[74] S. A. Maier, *Plasmonics: fundamentals and applications* (Springer, 2007).

[75] R. Schumann and S. Gregory, Department of Physics, University of Oregon, 1274 University of Oregon, Eugene, OR 97403-1274, USA, are preparing a manuscript to be called "Near-Field Modification of Interference Components in Surface Plasmon Resonance."

[76] C. Im, *Studies of optically-induced transient charge motion in tunneling microscope junctions* (PhD dissertation, University of Oregon, 1997).

[77] S. C. Kaiser, *Scanning tunneling microscopy studies, evaporated gold films and the interpretation of images* (M.A. thesis, University of Oregon, 1995).

[78] B. C. Yao, *Rectification mapping using the scanning tunneling microscope* (PhD dissertation, University of Oregon, 1997).

[79] K. M. Engenhardt, *Ultrafast dynamics and nonlinear behavior of surface-plasmon polaritons in optical microcavities* (PhD dissertation, University of Oregon, 2005).

[80] H. J. Simon, R. V. Andaloro, and R. T. Deck, "Observation of interference in reflection profile resulting from excitation of optical normal modes with focused beams," Opt. Lett. **32**, 1590-1592 (2007).

[81] D. M. Eigler, and E. K. Schweizer, "Positioning single atoms with a scanning tunnelling microscope," Nature **344**, 524-526 (1990).